CRANFIELD UNIVERSITY

Charalambos Andrew Georgiou

# Thermal Performance of a Multi-Axis Smoothing Cell

School of Applied Sciences
Precision Engineering

Masters by Research
Academic Year: 2010 - 2011

Supervisors: Paul Comley, Paul Shore
May 2011

CRANFIELD UNIVERSITY

School of Applied Science
Precision Engineering

MSc by Research

Academic Year 2010 - 2011

Charalambos Andrew Georgiou

# Thermal Performance of a Multi-Axis Smoothing Cell

Supervisor: Paul Comley, Paul Shore

May 2011

# ABSTRACT

Multi Axis Robots have traditionally been used in industry for pick and place, de-burring, and welding operations. Increasing technological advances have broadened their application and today robots are increasingly being used for higher precision applications in the medical and nuclear sectors. In order to use robots in such roles it is important to understand their performance. Thermal effects in machine tools are acknowledged to account for up to 70% of all errors (Bryan J. , 1990) and therefore need to be considered.

This research investigates thermal influences on the accuracy and repeatability of a six degree of freedom robotic arm, which forms an integral part of a smoothing cell. The cell forms part of a process chain currently being developed for the processing of high accuracy freeform surfaces, intended for use on the next generation of ground based telescopes. The robot studied was a FANUC 710i/50 with a lapping spindle the end effector.

The robot geometric motions were characterised and the structure was thermally mapped at the latter velocity. The thermal mapping identified the key areas of the robot structure requiring more detailed analysis. Further investigation looked into thermal variations in conjunction with geometric measurements in order to characterise the robot thermal performance. Results showed thermal variations of up to 13ºC over a period of six hours, these produced errors of up to 100µm over the 1300mm working stroke slow. Thermal modelling carried out predicted geometric variation of 70µm to 122µm for thermal variations up to 13ºC over a period of six hours. The modelling was 50% to 75% efficient in predicting thermal error magnitudes in the X axis. With the geometric and modelling data a recommendation for offline compensation would enable significant improvement in the robots positioning capability to be achieved.

Keywords: Robot, Thermal Performance, Thermal Model, Geometric Performance, Optics

# ACKNOWLEDGEMENTS

I would like to thank God and all those who have kept me in their prayers, my family and friends who have assisted me in writing my thesis and made many sacrifices for me. No trophy or victory in this world comes without sacrifice. I wish to thank all those during this time who offered support; specifically my parents Andreas and Rita Georgiou, who have unconditionally shown love for me. My sisters and cousin Maria Georgiou and Petros Sofocleous who gave me the opportunity to have the English and grammar checked during their working hours by their account manager Christina Georgiou. She also deserves thanks for her dedication throughout weekends which has been relentless. Natalie Georgiou for the reminders to keep me from distractions, my cousin Paul Pangalos who made many suggestions to me, sacrificing much time in making comments and suggestions for writing up my thesis and also for ideas for my VIVA presentation and offering his experience in working with other students. Theodore Veniamin who also offered advice in writing up together with his experience from a non-technical point of view who was always willing to lend a hand if I needed it. Wynand Swart from South Africa, after I sent a request for help over e-mail not having met him before who helped me with the DH Parameters for Fanuc Robot 710iC/50 for the kinematic model of my robot, and his secretary Han Li. Gratitude also goes to my supervisors Paul Comley who also spend many hours going over my work and making comments, I could not ask for a better supervisor, and Paul Shore for overseeing my work. All the technicians and staff who I would join for tea breaks and who enjoyed my ‘unique’ humour, biscuits and cakes. Andy, Xavier, John, Kevin, Adam, Alan, Roger, Yan, Ian, Renaud, and others. PhD and MSc by Research students Marco Castelli, Graham McMeecking, Tom Morris, Yinka Abedayo, Eva, Dominica, the Italian summer students, Andreas Bacci, Marco Targa, Andrea, Andrea and Simone and Yakubo, Saadia Hakim.

This whole experience has taught me what research is, it is not a perfect world where everything is set out for you, there are obstacles which are hard to overcome but not impossible, for everything I am grateful.

# TABLE OF CONTENTS

# LIST OF FIGURES

# LIST OF TABLES

# LIST OF EQUATIONS



# List of symbols/acronyms

## List of acronyms

(ISO): International Standards Organisation

(IKC): Integrated Knowledge Centre

(EPSRC): Engineering Physical Science Research Council

(RAP): Reactive Atom Plasma

(E-ELT): European Extra Large Telescope

(Box© machine): Big Optix machine. Trade name for machine

(CMM): Co-ordinate Measuring Machine

(ESA): European Space Association

(FEA): Finite Element Analysis

(rpm): Revolutions per Minute

(ANSI): American National Standards Institute

(ASME): American Society of Mechanical Engineers

(LVDT): Linear Variable/Voltage Differential Transformer

(SCARA): Selective Compliant Assembly Robot Arm / Selective Compliant Articulated Robot Arm

(TCP): Tool Centre Point

(PKM): Parallel Kinematic Manipulators

(SOPHIE): Surgeon's Operating Force-feedback Interface Eindhoven

(CCD): Charged Couple Device

(ADI): Absolute Distance Interferometer

(HPKM): Hybrid Parallel Kinematic Manipulators

(MRA): Multiple Regression Analysis

(MFN): Multiple Feedforward Network

(DH): Denavit Hartenberg parameters/table Jaques Denavit and Richard S. Hartenberg developed a method for representing multiple links and the frame at the end of the links.

## List of Symbols

$\Delta x$: Extension of material due to increase in temperature (µm)

L: Length of material in metres (m)

$\Delta T$: Temperature change of material (°C in this thesis)

CTE: Co-Efficient of Linear expansion (µm $m^{-1}$ $°C^{-1}$)

KW: Kilowatt

$\theta_i$: Angle of robot joint i = 1…6

di: Distance (d) between the Joint axis normals ($x_i$ and $x_{i-1}$) in frame for joint and link co-ordinate system. Offset (d) of end effector i=1…6

$a_i$ = Perpendicular distance between the $z_i$ and $z_{i-1}$ axis (The Length of the Link)

$\alpha_i$ = Angle of rotation about the positive (counter clockwise) $x_i$ axis, measured to the positive $z_i$ axis.

$T_6^0$: Transformation matrix from initial co-ordinate reference frame 0 to End effector frame i

$A_1^0$: Transformation matrix from initial co-ordinate reference frame 0 to frame i

$\overrightarrow{\boldsymbol{q_i}}$**:** Quaternion for frame i

$\begin{bmatrix} a_i\hat{\boldsymbol{i}} \\ b_i\hat{\boldsymbol{j}} \\ c_i\hat{\boldsymbol{k}} \end{bmatrix}$: Vector for quaternion in X, Y, and Z for $i^{th}$ frame with magnitude unit vectors i, j and k and a, b and c representing x, y and z respectively.

$A_{i\ Hot}^0$: Transformation matrix from initial co-ordinate reference frame 0 to frame I added to transformation matrix with thermal effect applied to frame.

$A_{iTi}^0$: Transformation matrix from initial co-ordinate reference frame 0 to frame i with thermal effect applied to frame.

$T_{6\ ThermalEffect}^0$: Difference between transformation matrix from initial co-ordinate reference frame 0 to end effector frame i with thermal load applied to transformation matrices and old transformation matrix.

$T_{6Hot}^0$: Transformation matrix from initial co-ordinate reference frame 0 to end effector frame I with thermal load applied to transformation matrices.

CNT0: Robot path program such that it does not miss the co-ordinate along path.

FINE: Fine positioning for the robot path programming

F(t): is the temperature as a function of time of an object,

$y_t$: Temperature after a period of time t,

k: Thermal time constant of the material

t: Time period

# 1 Introduction

The aim of this research project was to assess both the geometric and thermal performance of a multi-axis robot which forms an integral part of a smoothing cell intended for the production of metre scale free-form optics.

## 1.1 Background

The Precision Engineering Centre at Cranfield University specialises in research and development associated with 'State of the Art' high precision machine tools and processes. Research into process technologies includes the fields of grinding, diamond turning and Reactive Atomic Plasma (RAP) machining. Both grinding and (RAP) are important technologies for the manufacture of the latest generation of metre-scale optics. Current research is underway to investigate the manufacturing processes for 1.5m optics, see Figure 1, typical of those required for the European Extremely Large Telescope (E-ELT) (Comley et al., 2011). Requirements for the optimum performance of these optics are typically in the order of 75nm RMS form accuracy and 1nm RMS surface roughness (Comley et al., 2011).

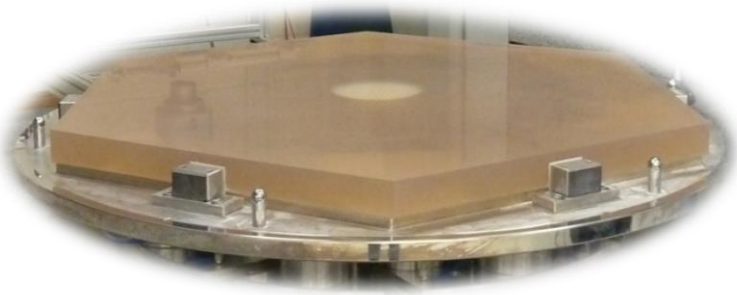

**Figure 1: E-ELT 1.5m Hexagonal mirror segment**

The optic free form surface is produced by a grinding process, followed by an iterative polishing stage to produce an optical quality finish, with the option to final figure correction with reactive atomic plasma machining, see Figure 2.

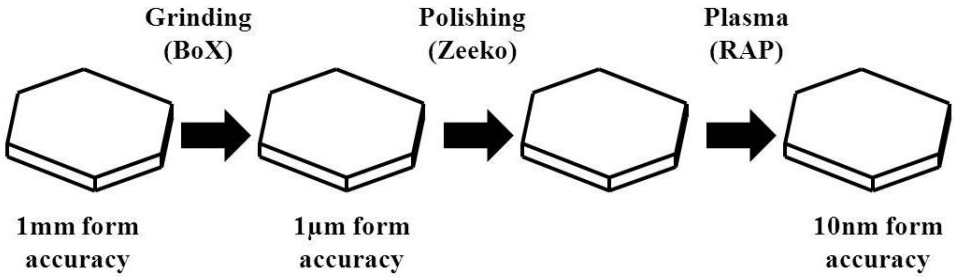


**Figure 2: Current optics process chain**

The high precision grinding takes place on the Box® machine developed at Cranfield (Comley et al., 2011) and polishing on the Zeeko machine developed by Zeeko, these machines provide a UK capability to produce large optics. All processing operations leave a signature on the surface, in the case of the grinding these are referred to as mid-spatials. Polishing out these features effectively is difficult and time consuming, as the mid-spatials are in the 1-20mm range. To remove these more efficiently, a smaller pad is required which increases the cycle time to polish the optic. It has therefore been proposed to introduce an additional process step between these processes to reduce mid-spatials and enable the polishing time to be reduced, see Figure 3.

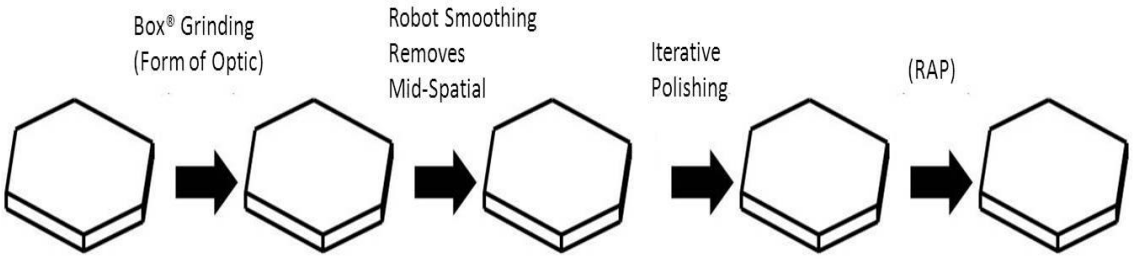


**Figure 3: Proposed optics process chain**

A multi-axis smoothing cell was proposed using a six axis robot, see Figure 4. The robots end effector had a smoothing tool attached. This was made from an air bearing spindle with a flexure unit supporting a lapping tool. The smoothing operation was assessed to require a motion accuracy of 100µm (Ahmed et al., 2010).

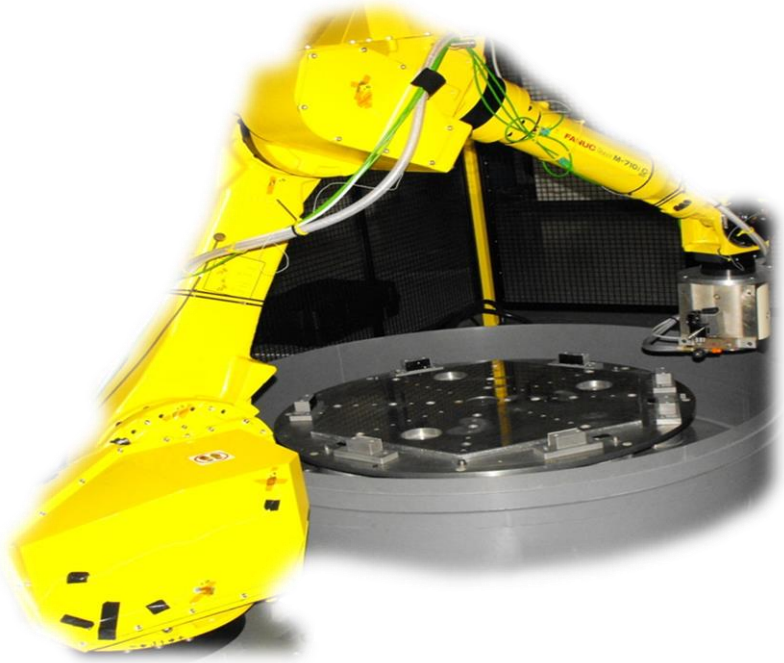

**Figure 4: Multi axis robotic smoothing cell**

## 1.2 Machine performance

Geometric errors are associated with the inaccuracy of a machine's tool to produce a required operation. This may be related to the linear motion producing straightness errors. It may be due to encoders not being directly in line with the point of interest (Abbé error). It may also be due to the environment in which the machine is operating, whether thermal or mechanical.

Thermal effects in machines can be responsible for up to 70% of the machining errors (Bryan, 1990). When high precision is required, (Bryan, 1990) suggests machines should be placed in enclosed cooling boxes to keep them in a temperature controlled environment to remove such problems. Also repeatable errors can be removed with electronic error compensation during machining.

Robot manufacturers quote repeatability values as a criterion for their machine performance. Accuracy is not generally quoted and will vary dependant on the environment the robot will be placed in. In Robots, thermal effects have been acknowledged to produce variations of up to 250µm. The FANUC 710i/50 robot

selected for the robotic smoothing cell has a quoted repeatability of 70µm, no data was provided for accuracy.

## 1.3 Research scope

This research looks at how the robotic multi-axis smoothing cell's accuracy and repeatability is affected by thermal changes. This is a six axis robotic arm with a lapping tool attached via an air bearing spindle. It will discuss possible compensation strategies for any inaccuracies and significant thermal effects. The thermal errors will be modelled and compared to the thermal effects observed thus giving further information for a compensation method.

## 1.4 Work plan

Initially a review of current and previous technologies in the relevant fields was undertaken. This began with geometric machine tools and how to assess them for both geometric errors and thermal effects. Thermal modelling and error compensation strategies were investigated.

The accuracy and repeatability of the robot in the axes was determined to help map the geometric ability of the robot for smoothing within a plane and provide a basis for assessing thermal effects. The robot was thermal mapped to provide an insight into the thermal distribution and variance under load, the information forming the basis for further point based measurements.

A thermal model was constructed based on data from the thermal mapping and used to provide performance data for the robot; this was compared against experimental data at a later stage to provide verification of the model.

The robot thermal performance was then characterised using a combination of thermal and geometric measurement instruments, over an extended running period representative of its intended use.

Based on results possible compensation methods were reviewed and an approach discussed.

# 2 Literature review: History and published work

Machine tool, robot designs and metrology together with their thermal influences are reviewed. Ways of addressing errors in machine tools with compensation strategies are also elaborated here.

## 2.1 Performance factors

This section discusses design of machine tools, thermal effects in machine tools and robots and environmental influences on robots and machine tools.

### 2.1.1 Machine design

Machines' volumetric envelopes range from tens of meters for applications in aircraft manufacture, to compact volumes of millimetres for micro-fluidic devices. Designs need to consider a number of identified principles for high precision motions. As well as the demands of the components to be produced, some of the approaches are described below.

Symmetry within machine tool structures enables the thermal loads, vibrations, and mechanical loads to be evenly distributed throughout, thus reducing distortion effects. This in turn will reduce errors and improve the overall performance of the machine. (Schellekens et al., 1998)

Modal analysis together with Finite Element Analysis (FEA) has been used to model how structures respond to vibrations and movements within the machine tool (Ricciardi et al., 1985). They state larger structures typically have lower natural frequencies of vibrations and higher inertial forces.

Alignment of a machine tool measurement system is another factor affecting performance. One instance is described by the Abbé principle. It is when a machine's tool path is out of line with the measurement system. A simple example of this is the calliper shown in Figure 5. The tilt of the sliding jaw results in a path length difference between the measurement axis and vernier scale axis (Slocum, 1992). The further out the object being measured, the

greater the effect of tilt. Another type of alignment error is a cosine error, where any angular misalignment in the axis motion and measurement path Figure 6, will introduce a path length difference.

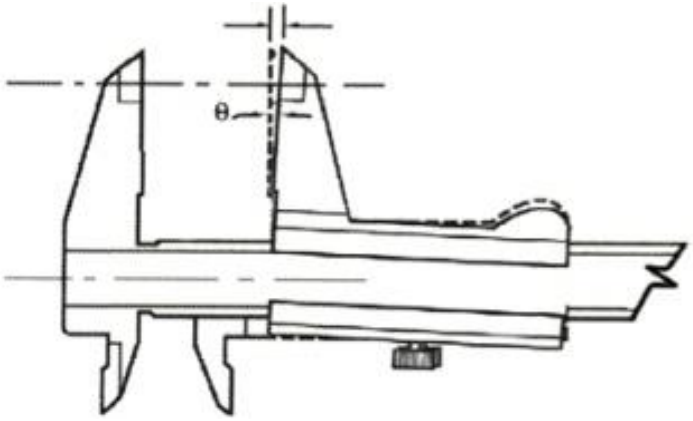


**Figure 5: Abbé error (Source: Mahr U.K. Plc.)**

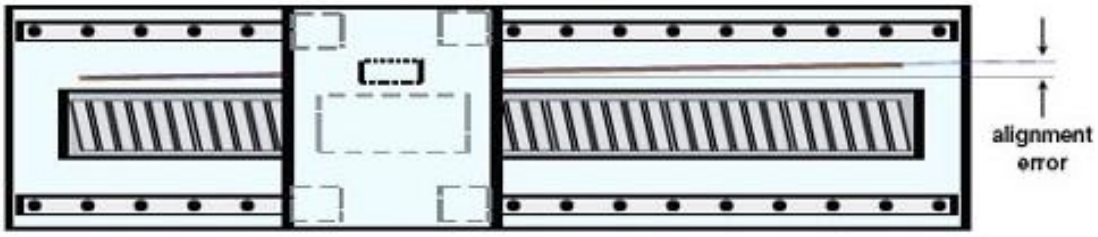


**Figure 6: Cosine errors (Source: Rockwell Automation, Inc.)**

The bearing technology employed will have an impact on machine performance. Fluid film bearings can offer high stiffness but give greater thermal impact due to the friction generated from the greater shear stresses. Aerostatic bearings have lower stiffness but reduced friction. Roller ball bearings with their high contact forces provide higher thermal input. Non-contact technologies such as fluid and air bearings have the longest life, but the higher accuracies lead to higher machine costs. Contact technologies such as roller bearings offer a lower cost and maintenance options. The decision of which bearings to use would depend on the machining requirements (Slocum, 1992). Modelling work for a 500rpm air bearing spindle over a duration of 1.5 hours showed an increase in temperature of 0.5°C (Gim, 1997), with an axial increase in of 2µm. Another simulation showed 4°C over a period of two hours resulting in

increases of 7µm. Gim reasons that thermal growth in an aerostatic spindle of more than 6µm is not negligible in ultra-precision machining. High speed spindle units using roller bearings generate far greater thermal loadings. For example (Zverev et al., 2003) predicted a 40°C temperature rise running at 25,000rpm which compared closely to the experimental data showing a 35°C temperature change. Operation below 1000rpm had a negligible effect. For these reasons an air-bearing spindle fitted to the smoothing cell offers the best solution.

The robot within the smoothing cell has a combination of motors, reducers and gears which are required to produce the desired motion. These have a thermal impact on the structure. Thermal effects can account for up to 70% of the machine tool errors during operation (Bryan, 1990). Many different techniques have been introduced to reduce these, such as cool boxes or increasing the mass of a machine so that its thermal inertia is very high.

A paper by (Schwenke et al., 2008) discusses six major sources of machine inaccuracies namely kinematic and thermo-mechanical errors, loads, dynamic forces and motion control and control software. Often these areas affect the structural loop of the machine. They quote the ANSI and ASME standard B5.54 that “A structural loop is defined as an assembly of mechanical components which maintain a relative position between specified objects”. Their paper discusses kinematic errors consequential from imperfections of the machine geometry, the size of the components, the way those parts are placed in the structural loop, and the measuring system inaccuracies. The paper discusses how thermo-mechanical errors, are partly due to the differences in material co-efficients of thermal expansion. These result in deformations within the machine structure which in turn affect the motion accuracy. Typically robots’ are made using a different material in the motors, arm and base. As such, the expansion co-efficients will cause bending and affect the position of the end effector. They also discuss that machines are not perfectly stiff and hence loads induced by moving carriages or contact forces, influence accuracy. Also vibrations during machining affect performance.

For a motion in a linear direction, there exist six component errors per linear and rotary axis, three location errors per linear axis, and five location errors with every rotary axis that the machine has (Schwenke et al., 2008). The robot trying to move accurately will have six (orientation and location) motion errors. In addition to this, the axes will not necessarily be aligned. There will be a total of two squareness plus one zero point location errors per axis. The squareness error between the Z axis and X axis is the same as that of the squareness of the X and Z, Therefore it will have six axis errors and six motion errors totalling to twelve. This thesis will only look at the linear positioning and straightness errors of the end effector in each axis during the paths which it will undertake.

### 2.1.2 Environment and thermal effects

Environmental influences include properties such as temperature, humidity, pressure, vibration and dust. When working at higher precision, the properties of its surrounding environment such as temperature and humidity are measured and compensated for or controlled. Standard laboratories are maintained at 20°C and for the last 20 years this has remained the case (Bryan, 1990). Bryan's paper discusses the possibility of having this temperature standard changed due to being too cold and uncomfortable for factory workers, especially in developing countries, it is also cheaper to heat a room than to cool it. Reasons to prevent this change were that machines could be placed in cool boxes and that every gauge block and device would go out of tolerance if this was implemented.

In addition to thermal dimensional variation, a paper by (Kim et al., 2002), found an influence on the process chemistry. Environment temperature effects on the removal rate of material are documented; 30°C environment temperature gave about 0.02µm a minute removal rate and at 60°C; 0.2µm per minute.

Laboratory environments are maintained at 20°C so that measurements meet international standards. Techniques are being developed to maintain machines to this temperature. A keynote paper by (Bryan, 1990) discusses on-going development in this field.

Oil showers have been developed to keep machines thermally stable. The paper by (DeBra et al., 1986), describe a system, oil drift temperatures during that time being 0.028°C, air drift temperature was kept at 0.556°C, oil shower drift temperature of 0.0056°C. The result in a constant LVDT (Linear Voltage/Variable Differential Transformer) reading of 20µin = 0.508µm for spindle displacement over a 16 hour period. They propose that oil showers can be more cost effective than temperature controlled rooms.

For robots and this project in particular, this could be an effective means for keeping different parts of the robot and spindle cool and reduce thermal errors. However, whether the robot can deal with the oil shower and not get damaged would need to be assessed separately.

Generally, factory floor temperature variations are of the order of degrees. In this environment the variation and thermal time constants of machines measurement system and components play a part. One paper showed that the variations of factory floor temperatures in Frankfurt is 10°C from summer to winter, such variations were found to cause up to ±50µm radial drift in components produced on a lathe (Weck et al., 1995).

The laboratory in which the robot will be used is going to be temperature controlled to within 0.5°C. This should minimise these environmental issues when smoothing the optic, although it does not eliminate thermal errors from the smoothing process itself, which will need to be characterised.

(Heisel et al., 1997) looked at the thermal and geometric performance of three types of robots. Over a 42 hour period with variation of the ambient temperature, the resulting displacement measured for a six axis articulated robot tool was up to -250µm in Z and (100µm and 160µm in X and Y respectively). They also heated a Selective Compliant Articulated/Assembly Robot Arm (SCARA) via two stages, one with a heat load of moving the robot followed by the ambient air temperature being raised 15°C followed by a cooling phase. During these stages, the motor for the z-axis heats up at most by 35°C

and maximum Tool Centre Point (TCP) displacement was found to be 150µm in X and 180µm in Z.

### 2.1.3 Robot design

This area considers the designs of multi-axis machine tools known as robots and how they are different to the machine tools. They come in various forms from Parallel Kinematic Manipulators (PKM) to serial robotic arms.

The main characteristics that robots have are the type of motion that they are able to produce. While being able to produce linear motions in Cartesian co-ordinates, they do not have the limitation that other machine tools do in being limited to those axes. Some machine tools have rotary axes but generally motion is limited to Cartesian motions and possibly one or two rotary paths.

With a robot, and in particular multiple joint arm robots such as five or six degree of freedom robots, the tool path can describe paths that would prove difficult for other machines to achieve. They can be on a programme for particular tasks such as cleaning, placement, polishing, and as for this application describing a spiral or raster path over an aspherical form. Due to their speed of operation and price in comparison with other machines designed specifically for one task, they are more versatile in what they are able to do. Recently, robots have been used by surgeons in the medical industry due to the versatility and precision of their motions. Robots are now being used by doctors and trained surgeons and their design needs to accommodate this. The robot in Figure 7 is a new type of surgical robot with a force feedback system to provide the surgeon with information on applied forces. The understanding of robot performance is paramount to the safety of people's lives, as well as the overall quality of products a robot will help to make in industry (Camarillo et al., 2004). In medicine the use of a vision guided SCARA robotic system was deemed adequate to perform in an operating theatre and had repeatability ranging from 30µm to 920µm and accuracies of 0.1mm to 1mm depending on the position it was moved to and they state that refining would be required. (Awang and Abdullah, 2010).

As with all machine tools, the surrounding environment will affect its performance to some degree. Vibrations during machining, temperature, humidity and noise, all play a part in the overall performance. If the robot is not in a temperature controlled environment, then the overall performance will vary from one day to the next. The stiffness in the robot will affect the amount of vibrations it will be able to sustain before its overall work is affected.

**Figure 7: Surgeon's Operating Force-feedback Interface Eindhoven (SOPHIE) (Source: World Laparoscopy Hospital)**

In 2010, a fine positioning module was fixed on to a (SCARA) robot (Sulzer and Kovač, 2010) an example of one can be seen in Figure 8. It consisted of a CCD camera with resolution of 2µm per pixel and the micro-positioning piezo-robot had a minimum accuracy of 20µm, the (SCARA) robot had a repeatability of 10µm. This was for enhancing the accuracy of this robot to perform micro-positioning for micro-grinding and milling. It is a relative positioning system which takes care of the thermal error aspect and they suggest that this is not to be limited to SCARA robots. Varying configurations of servomotors being off and on as well as having additional lighting gave the relative positioning-convergence behaviour a repeatability of under 20µm after four iterations. Template matching repeatability had a median position deviation of 455.81 pixels (912µm) with a variation of +90µm and -35µm over 100 measurements. This is comparable to the accuracies in the paper by (Awang and Abdullah, 2010). One could envision with slight adaptations that it could be used on serial robots and possibly micro-smoothing. Robotic arms in general are the least stiff while Parallel Kinematic Manipulator (PKM) devices see Figure 9, are the

stiffest but have limited movement. (Briot and Bonev, 2007) compared the accuracies of a selection of two parallel robots and serial robots. Whilst the parallel robots seemed to show higher accuracy, the paper suggests that the general variations are high so that it is very difficult to make a direct comparison.

Performance of robots is affected by structural design and the accuracies of axis encoders (Greenway, 2000). A number of papers have looked at how to assess the performance for robotic arms and looked at their accuracies; (Van Brussel, 1990), (Dukovski, 1990), (Karan and Vukobratovic, 1994), (Vira and Estler, 1990), (Young and Pickin, 2000; Nawara and Kowalski, 1987) to name a few. Their findings show that accuracies are normally an order of magnitude greater than the quoted repeatability.

**Figure 8: SCARA robot, (Source: Advanced Motion Systems, Inc.)**

**Figure 9: PKM (Source: Innovative Conveyor Concepts Robotics)**

This was also mentioned in a paper by (Young and Pickin, 2000) who found the repeatabilities were within the quoted tolerance by the manufacturer. They did linear positioning and straightness measurements along the X and Y axes of a

number of robots. The better system had accuracies of ±100μm while the worst were 1.8mm

Robots' performance is affected by the loading applied. The maximum deflections seen in the experiment done in the paper by (Eastwood and Webb, 2010) using up to a 35Kg load with three repetitions, gave a displacement in the fifth joint at 90° orientation of 100μm.

As with machine tools, if very accurate and repeatable positions are to be attained, robot designs need to take into account thermal effects and the type of work that will be required.

The main source of heat in a robot will be in the motors located at the joints, the largest motors are normally found in the base of the robot. Heat generated at the joints produces thermal gradients along the interconnecting arms. Dependent on the operation, for example cutting, de-burring or grinding, the process may also have an influence. The spindle itself will also provide a source of heat.

As stated previously thermal errors in machine tools can account for up to 70% of the total errors (Bryan, 1990). There have been various people working to improve the accuracy of robots due to thermal effects. The paper by (Eastwood and Webb, 2009) investigated around the motors of a Hybrid Parallel Kinematic Manipulator (HPKM). Their results showed 70% reduction of mass induced errors and 84% reduction of thermal drift errors in the tool centre position.

There has been much less research into thermal influences on robot performance than for machine tools in general. One reason is that the need to understand this area has been paramount to the type of work that they have to be used for. Generally required accuracies have been too low for thermal effects to be a problem for most applications but it is increasingly becoming an important issue that needs to be addressed (Gong et al., 2000). In their paper it states that other groups have reported that temperature adversely affects the repeatability and accuracies of robots. For the intended smoothing application,

thermal effects of a multi-axis smoothing facility would need to be assessed in order to ensure that the high precision requirements can be met.

An example of how thermal effects cause changes in robots performance can be found in (Heisel et al., 1997), showing that for the six axis robot arm a 12K temperature shift causes a -28.8 arc second deviation in the second axis arm. They found a thermal effect of 2.16 arc second / K. In their experimental results and discussion. They also discovered that the different payloads on a robot arm with six axes did not have such an impact on temperature as that of axis velocity. Doubling the velocity increased the steady state temperature by 1.5 times as much, although the time constant to reach this temperature remained constant.

A masters thesis by (Mackay, 1982) compared robots driven either electrically or hydraulicly. On electrically driven serial robots, deviations seemed to be unaffected by thermal increase or stabilisation time of just over 3.5 minutes with a 5°C to 9°C temperature increase above a 20°C ambient temperature, a constant 300µm was observed from beginning to end (before and after thermal stabilisation). This implies its thermal gradients were not significant enough and electric drive robots have a cooler operating temperature, hence thermal effects are minimal. The measurements were done with a slide-way with a LVDT for making measurements in three dimensions transducer attached to the end effector. The hydraulic drive robots showed a 2mm thermal effect, and one of the robots showed minimal deviation of 300µm after thermal stabilisation with temperatures at 12.5 minutes, ranging from 32°C to 45°C of different components and fluids in the robot. Whereas, another robot showed an increase and stabilisation of temperature of 40°C to 45°C at 7.5 minutes with an increase to a constant thermal error of 2mm, 35 minutes thereafter. Compliance errors varied from 7mm to 12mm and an error of a spray robot was up to 17.5mm over the path length of 750mm. It was found that electric drives stabilise quicker than hydraulic drive robots. This makes sense since hydraulics depend on fluid, while electric drive is the flow of electricity. It is noticeable that robots have a thermal stabilisation time and this may need to be considered

when machining the optic so that when smoothing will take place, the robot is thermally stable so that a uniform smoothing motion is produced free of thermal effects pre-warm up stage. The transducers and setting up of experiment was done in a temperature controlled environment at 20°C, but whether this was always the case is not known, in the appendix it mentions robot ambient temperature of 45°C.

Commercial robots dealing with assembly tasks can have repeatability values of ±0.3mm and absolute accuracy of ±5mm to ±10mm (Reinhart et al., 1998). They state that accuracy can be improved by considering a number of factors such as gear box, beam links elasticity and the kinematics of the robot involved.

At the other extreme, modern robot systems are used for ultra-precision machining. A research group (Lubrano and Clavel, 2010) simulated such a device in a temperature controlled environment. The robot had a working volume of $1cm^3$ and was mounted on a vibration insulated table. Displacement measurements were made over a temperature range of 21°C to 25°C. After thermal calibration and compensation, an absolute accuracy of ±71nm was reached.

## 2.2 Geometric performance measurement

This section discusses the different methods available to assess the geometric performance of machine tools generally and their applicability to the robot.

Metrology of machine tools and robots is advancing, some methods have been in use for a while, contact measurements and non-contact methods have their advantages and disadvantages. For robots, most groups have used non-contact laser based tracking due to the many degrees of freedom and range of different path motion that they undergo. The accuracies of laser tracers show promising ability to assess robots and would be a good tool in assessing thermal effects as well as geometric errors. Laser trackers are not yet accurate enough to get to ten times the accuracies required for robot assessment and the author believes they could be superseded in the future by laser tracers. These are able

to measure at least five degrees of freedom and technologies to measure more degrees of freedom could be developed.

In order to fully exploit a machine tools performance it is necessary to know its accuracy. For precision, machine accuracy is of the order of micrometres and ultra-precision in the order of tens of nanometres. The geometric metrology devices discussed, are categorised as direct and indirect measurement devices. It is important that a device's repeatability and measuring speed be ideally 10 times higher, or at least three times that of the machine being measured (Jiang et al., 1988).

Machine tools have been monitored for their accuracy with many types of different technologies. These range from very fine artefact objects, laser based measurements, non-contact displacement transducers and ball bars for testing circular motions. A very recent analysis of different measuring techniques has been made by (Schwenke et al., 2008).

There is a number of papers concerning on how robots are tested for their accuracies, repeatability and thermal performance: (Jiang et al., 1988), (Van Brussel, 1990), (Dukovski, 1990), (Karan and Vukobratovic, 1994), (Vira and Estler, 1990), (Young and Pickin, 2000; Nawara and Kowalski, 1987). Here, a selection of the most applicable methods currently available are presented.

There are two methods of taking measurements from machines. The two subsections; direct and indirect, will go into more detail of how this is done.

### 2.2.1 Direct methods

This section appraises direct methods of assessing machine tool geometric performance.

Direct measurements of machines involve a device that takes a measurement of the tool path in space. Devices include laser interferometers, touch probes or ball bars. The measurement is taken and compared to the machines

programmed motion. This difference indicates the machines inaccuracies. A number of these are presented here.

In the paper by (Peters et al., 2001) Absolute Distance Interferometers (ADI) are discussed. In laboratory conditions the group attained a 1μm uncertainty in 5m distance. Lasers are used by some groups for pointing at CCD cameras. Such an experiment was done with a laser attached to a robot and the laser was repeatedly pointed at the same co-ordinates, thermal drift was observed. More will be mentioned about similar work (Poonyapak and Hayes, 2006) in the thermal performance of Robots section 2.3 Thermal measurement.

A paper by Nook (1985) discusses various methods for industrial metrology using interferometers. Firstly they discuss measuring the optic of a 2.4m primary mirror in the Hubble space telescope with a coaxial reference interferometer and a reflective null corrector. To look at the contour of an optical surface, a method they developed was using a tetrahedral mount to place interferometers with special precision aiming systems, to send the laser beams to a light reflecting target. With automatic tracking, it was able to look at the contour of an optical surface. Also laser tracking systems were being developed for robot metrology in five dimensions. The laser tracking system showed that over an area of 250mmx350mm, an accuracy of ±12μm was obtained.

Schwenke *et al.* (2008) updates from a keynote paper by Sartori and Zhang (1995) and discusses different methods of characterising the errors in machine tools, with various tools such as simple laser interferometers for linear motion. It also looks at laser interferometers with three beams to measure distance, pitch and yaw along one axis of motion simultaneously. Ball plate and artefact methods are also queried in this paper, as well as different types of LVDT probes and non-contact probes which shall be viewed later.

Developments in interferometer technology are being made; one group simultaneously measured the relative displacement position of a straightness error (Chen et al., 2009). They used two heterodyne interferometers, one being a proposed device and the other made by Agilent. The experimental setup

provided them a resolution of 0.316nm, each measurement was made with the proposed interferometer and simultaneously compared with the Agilent interferometer straightness measurement. There also were two linear displacement devices with a different resolution. One device had 0.1µm resolution while the other had a resolution of 1nm. With the linear displacement step size of 1mm with the 0.1µm resolution device, the magnitudes of straightness error was 0.55177µm to 0.57430µm between 83mm and 84mm of the linear displacement compared to the Agilent straightness value of 0.40992µm at 84mm. In the micrometre range of 0µm to 5µm and step scale of 100nm using the device with nanometre resolution, the magnitude of straightness error was 24.92nm at position 0.2967µm. The Agilent interferometer measured 24.74nm at position 0.1895µm and in the nanometre step size 10nm, measurement straightness error values were 11.51nm at 283.72nm displacement and compared well to the Agilent device of 12.56nm at a displacement of 274.93nm. This device could be used to simultaneously measure the linear displacement error and straightness error and also measure the position of the straightness errors. Whether this is available to be used in universities is another matter.

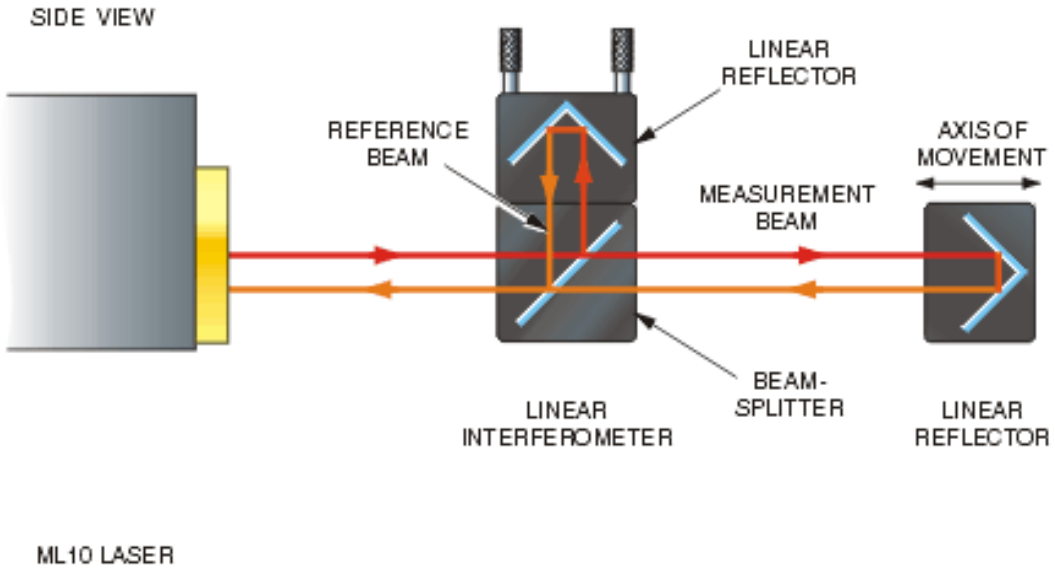


**Figure 10: Linear positioning (Source: Renishaw Manual)**

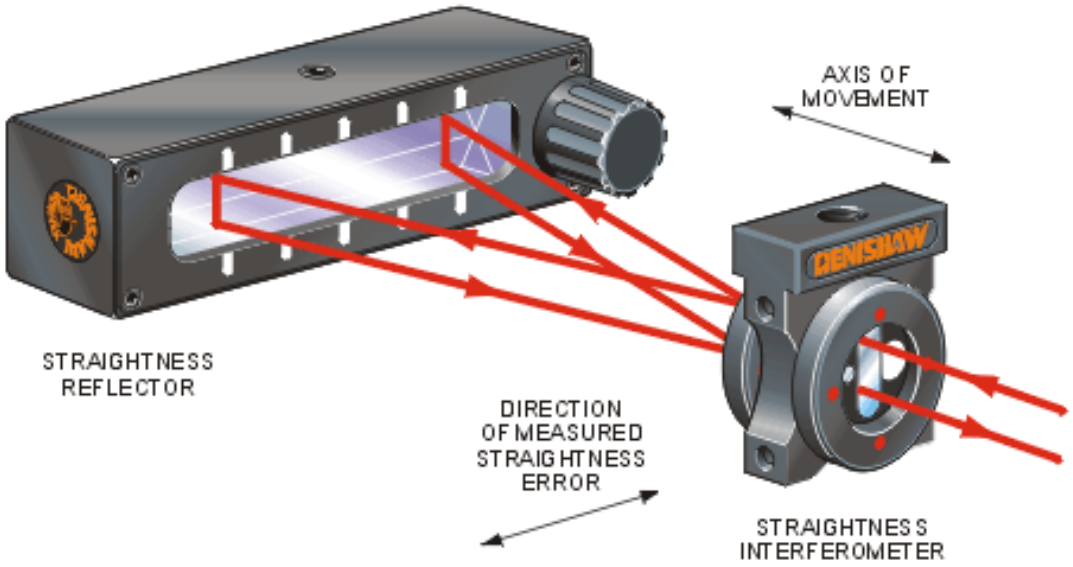


**Figure 11: Straightness measurement (Source: Renishaw Manual)**

The principles of straightness and linear positioning measurements can be seen in Figure 10 and Figure 11. The change in the beam path difference produced during motion gives the error. Linear positioning error is the inaccuracy of a device to attain a specified position along the motion of travel. Straightness error is the horizontal or vertical error motion perpendicular to the motion of travel.

Another metrology device intended to look at circular motion of machine tools is a ball bar. Ball bars work by measuring the deviation from a mathematically perfect circle. There is a transducer inside the centre of the bar which measures the change in position of the balls as the spindle to which they are attached, deviates from the ideal circular path. The balls are magnetic allowing a large degree of movement of the ball bar.

The authors Jiang *et al*. **(1988)** look at ball bars and suggest this is a method that can be used on robots although with limited path analysis. In the paper the principle was based on a tripod, spherical ball with a magnetic base, the ball has a mathematical centre of origin and the end of the ball bar is attached to the robot end effector.

Ball bars could be used to maintain circular motion accuracy and its variation over time. Renishaw provide bars up to 600mm in length.

**Figure 12: Ball bar (Source: Renishaw plc.)**

Non-contact probes have been used to assess machine tool geometric performance over short distances. Gim (1997) used a fibre optic sensor and inductor sensor to also measure displacements of a spindle in a machine as it was spun at different rates and measurements accurate to 1μm. Some of the measured displacements were found to be 5μm for a 2˚C change and 2μm for a 0.5˚C difference.

Mian *et al.* (2009) used non-contact displacement transducers to measure displacements of a vertical milling machine tool in the X, Y and Z axes. This data was fed in to support the modelling for the experiment for off line thermal performance giving less than 10μm difference to simulated and experimental data. Both fibre optic and non-contact transducers may be useful for assessing robots to position the end effector on the optic as it will smooth to help maintain accuracy and repeatability.

Laser trackers use laser interferometry in conjunction with angular encoders to track motion. The way they work is to send a laser beam through a series of mirrors mounted on rotary encoders out to a retro reflector and back to be compared to the reference path. Movement of the retro reflector can then be measured as a displacement and angle. The main errors with such a system arise with the beam path through the mirror system. A schematic showing the

basic principle of how a laser tracker works is shown in Figure 13.

The Leica Tracker 901 model is a commercially available instrument, with a maximum permissible error (MPE) of 15µm + 6 µm/m, if used as only an interferometer, much higher accuracies can be achieved.

Linear positional errors of a robot have been assessed (Alici and Shirinzadeh, 2005) using a laser tracker device. Inaccuracies of almost 10mm were found along the axis of measurements. Their model estimation of the errors reduced this to less than 1mm in one of the paths and the difference in the predicted and measured data was of the order of 2mm.

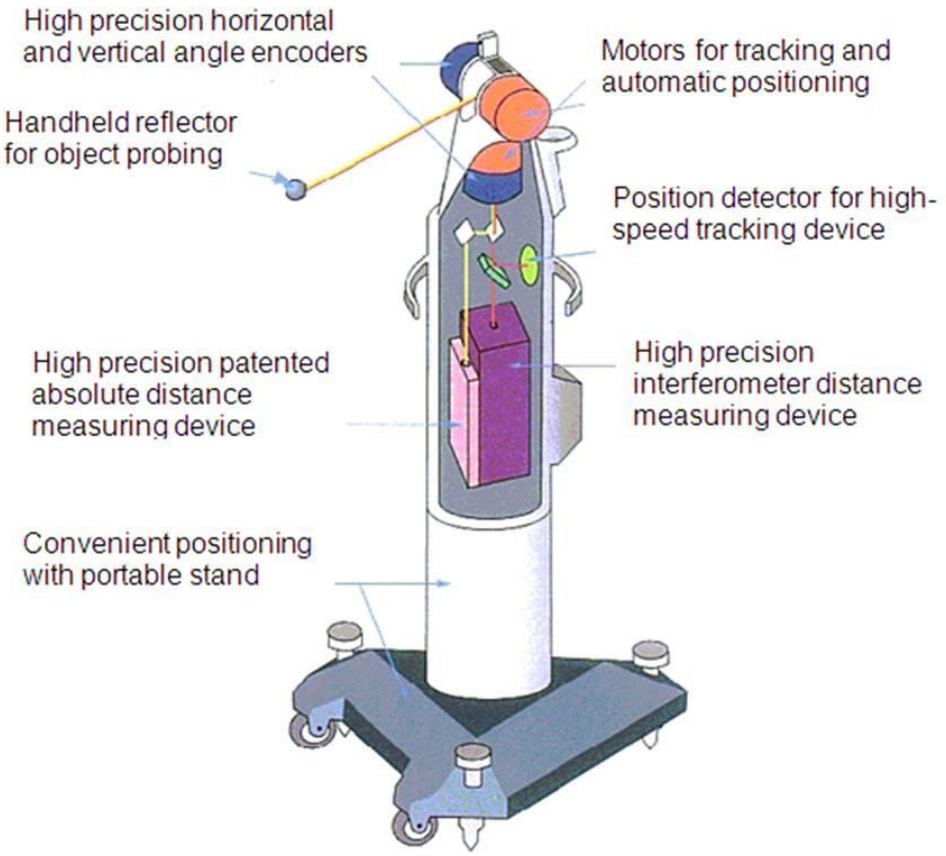


**Figure 13: Laser tracker principle (Source: LDB Corporation)**

Another device similar to a laser tracker is the Laser Tracer, see Figure 14. These are far more accurate and can achieve accuracies of 0.2µm to 5µm. The availability of such a device though is through the National Physical Laboratory

(NPL) and Etalon. A white paper written on this, **(Schneider, Carl-Thomas. AICON 3D Systems GmbH, 2004)** indicates the principle.

They work on a similar principle except that their reference is a spherical ball which has a sphericity up to 50nm. This removes the inaccuracies introduced by angular encoders in trackers. Associated software developed directly accesses a machine controller and program paths that carry out the required motion for measuring according to a standard. From this the geometric performance can be automatically assessed and compensated for. The system is ideally suited for measuring the geometric performance of the robot.

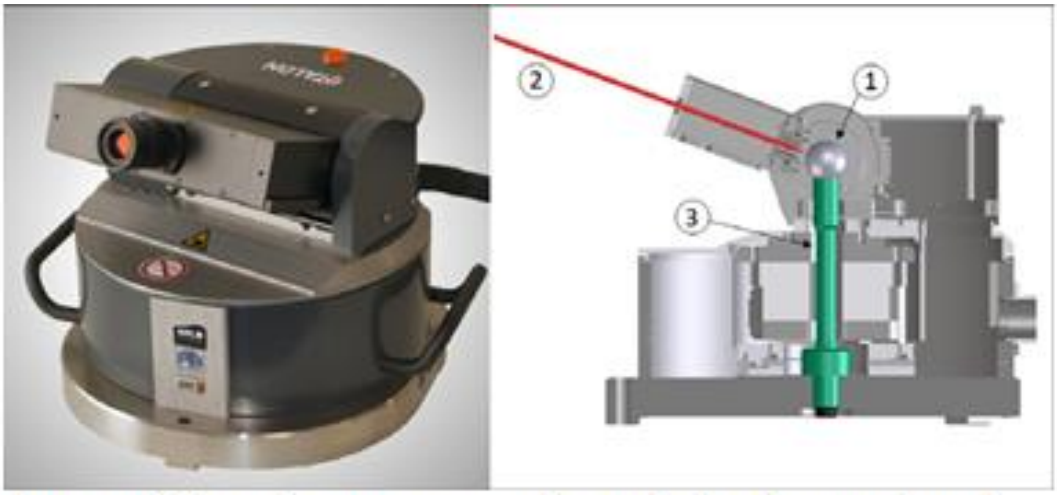


**1) A precision sphere serves as the optical reference for all distance measurements**
**2) Measuring beam of the laser interferometer**
**3) Mechanically decoupled pillar for the reference sphere**

Figure 14: Laser tracer principles (Schneider, Carl-Thomas. AICON 3D Systems GmbH, 2004)

### 2.2.2 Indirect methods

This section concentrates on indirect methods of assessing machine tool geometric performance.

Indirect methods involve using an artefact device that is made very accurately and has been characterised prior to its use. This is then used as a reference to

measure machine motion. These measurements are then compared to the known positions of the artefacts to determine the errors.

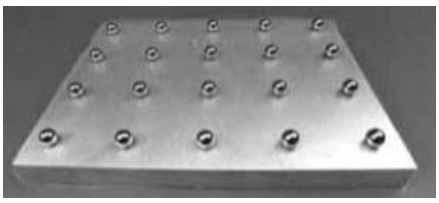

**Figure 15: Ball plate (Source: Bal-Tec Inc.)**

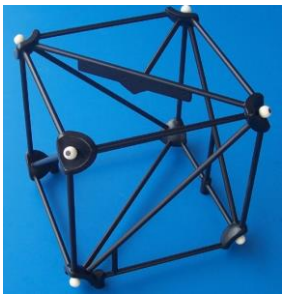

**Figure 16: Ball cube (Source: Trapet Precision Engineering)**

Artefact devices can use spherical balls, these balls held on a plate for single plane or cubes for measuring multiple dimensions see Figure 15 and Figure 16. Each device has its advantages and disadvantages. Artefact sizes vary but typically they require several time consuming measurements of the artefact repositioned in different locations in a machine to produce a volumetric error map.

A different variation in Figure 17 is shown where the plate that has three v-sections primarily intended for testing a machine's volumetric performance. The ability to measure positions is given more freedom to manoeuvre due to the space in between each of the artefacts.

**Figure 17: 3D Ball plate (Source: Bal-tec Inc.)**

In Figure 18, a large ball bar measurement artefact designed to calibrate CMM's is shown. The position of the ball bar is shifted and the software provided by the supplier produces a position error map.

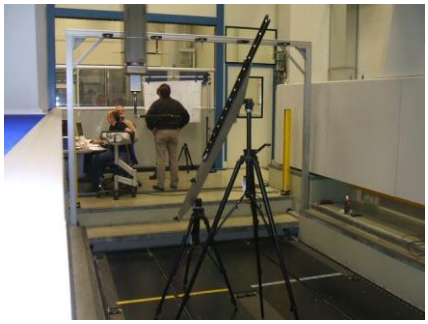

**Figure 18: Giant ball bar (Source: Trapet Precision Engineering)**

Typical artefact devices are used in conjunction with direct measurement systems to provide a volumetric error map of machine tools.

## 2.3 Thermal measurement

This section evaluates temperature measurement devices suitable for investigating machine tool thermal performance, both contact and non-contact types are covered.

In order to assess thermal effects in machine tools and robots, the measurement of temperature or at least prediction of temperature, is necessary. Ideally the temperature should be monitored simultaneously, with any assessment of the machine's geometric performance. A number of different ways of measuring the thermal effects with contact and non-contact devices such as thermocouples and thermal imagers are discussed. Monitoring temperatures before, during and after a machine is working, allows the thermal influences to be assessed.

### 2.3.1 Contact devices

Devices covered include thermocouples, thermistors and thermometers.

Contact devices work using a principle of attaching a metallic material onto the surface of interest and measuring properties such as change in resistance or

electric field. The property relationship is calibrated against known temperatures, for example the boiling point of water and ice.

If the thermal time constants for a machine are rapid then a very quick response time of a device will be necessary, otherwise large thermal time constants will not need such rapidly responding devices. If a machine has large thermal errors resulting from small temperature changes then the sensing device needs a high sensitivity. Generally good machine designs have long thermal time constants and low thermal sensitivities.

An electric field forms when there is a thermal gradient across a material (Seebeck effect). Thermocouples use the change in voltage created by the changes in electric field of two different materials subjected to changes in temperature.

There are many types of thermocouples available including T and K type. These devices do not require the sensor heads to be powered. Different types can deal with a large range of different temperatures and are fairly robust. One disadvantage is that they are susceptible to noise and have a large working range reducing sensitivity. C type thermocouples have a 15μV/°C sensitivity and operate over a range of 0°C to 2000 °C. Type J are sensitive to 15μV/°C operating in the range -210°C to 1200°C. Response times are dependent on the joint between the two different types of metal. Dependencies include on the size and conductivity of the join and type of metal, as well as the thickness of material. Naturally thinner joints will respond very quickly but will be more fragile. PTFE K type with a soldered join of about 1mm diameter thermocouples have a response time of about 0.5 seconds. A whole range of different products are available from manufacturers, hand held touch probes have a longer response time of between one second to two seconds due to the joint configuration.

The attachment of thermocouples to PCB (Printed Circuit Board) surfaces was assessed in a previous study by a research group (Cameron, 1999), they found that soldering the thermocouple head to the solder pad of the (PCB) connection

produced the most repeatable temperature results followed by aluminium tape overlaid with Kapton© tape, both Kapton© tape alone (an electrically insulating polyimide tape working at a high temperature range) and conductive epoxy dry set on the thermocouple head was not repeatable . Using a tape with thermal paste is suggested as a means for attaching the thermocouples to a robot to work sufficiently (Mackay, 1982). Thermocouples are suitable for use on articulated structures such as robots provided they are positioned so that they will not undergo duress.

Devices working on the relationship between resistance and temperature are known as Thermistors. These work on the basis of measuring the change in resistance of a wire as the temperature changes. There are either Positive Temperature Co-Efficient (PTC) or Negative Temperature Co-Efficient (NTC) thermistors, PTC's provide an increase in resistance whereas the NTC's a decrease with increasing temperature. Thermistors are very sensitive being able to measure at almost milli-Kelvin with careful calibration. They have advantages and disadvantages; they are very sensitive and cheap, but readily available devices available with the plugs and assembled casing is hard to find. Devices need to be powered which also causes stray heat which can potentially affect measurements unless a three or four wire thermistor is used. Resolution is well beyond the requirements for measuring machine structural thermal effects. Platinum based thermistors are (PTC) devices, and offer the best linearity, although they are more expensive than other thermistors. The temperature needs to be very high before linearity begins to fail (Nawrocki, 2005).

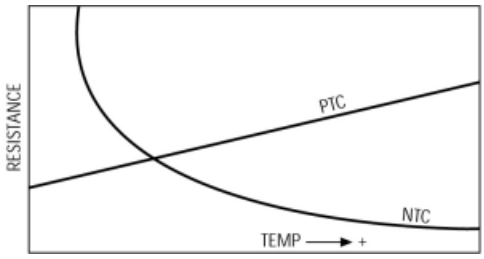


**Figure 19: PTC curve (Source: Amwei Thermistor Co., Ltd.)**

Yoshioka *et al*. (2004) attached a micro platinum thermometer to a diamond cutting tool where micro-machining takes place with an aerostatic spindle on an ultra-precision diamond turning machine. It is mounted on the tool tip with dimensions of 0.52mm x 0.025mm placed 0.8mm from the cutting edge. The temperature of the machined part can be monitored with better accuracy.

Contact devices are more prone to damage from the environment and operation of the machine. Care needs to be taken when mounting on articulated structures such as robots. The advantage of these devices is that they can give a relatively accurate measurement of the surface (without external interference) of a material and can be placed as required e.g. on a cutting tool (Yoshioka et al., 2004). They are relatively cheap compared to other methods simple to use and readily available in many different varieties.

### 2.3.2 Non-contact

Non-contact devices usually consist in using Infrared cameras picking up infrared radiation or laser spot devices which measure the reflected amplitude of light that comes from the surface of the material.

Non-contact devices include Infrared cameras detecting emitting infrared radiation, laser spot devices which measure the amplitude of reflected light. Thermal imagers, see Figure 20, use emitted infrared radiation from a surface to measure temperature. The infrared radiation emitted from objects, represent the thermal gradient as a colour gradient see Figure 22 and Figure 23 (Blue to Red to, yellow to Bright white). From this data surface temperatures of an object can be measured (as these instruments look at areas). Thermal maps can be obtained for surfaces, these maps are very useful initially as an indication before higher accuracy measurements are made. Pyrometers or radiation spot meters take measurements of a particular point. They require calibration if accurate readings are required. If a number of instruments are required, then this is impractical due to the high unit cost. Their principle of operation is via an infrared laser focused onto the surface, the reflected energy coming from the material surface converted into temperature readings via Stefan Boltzmann's

law, which relates energy to the temperature of an object.

The emissivity of a material needs to be calibrated so that the temperature of the material being measured reads the same from a black dull surface as it does when reading from a shiny surface. Careful setup is required in viewing angles and reflective surfaces for good measurements. Readings can be affected by environment and dust, (Kral and Matthews, 1996). Figure 21 shows the relationship of spectral radiance and temperature with the wavelength of light.

**Figure 20: (Source: of Pyrometer Instrument Company, Inc., Pyrometer)**

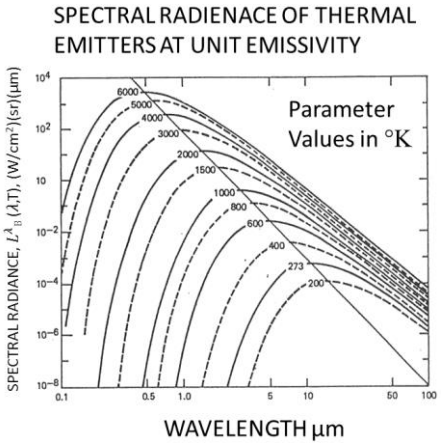


**Figure 21: (Source: of Pyrometer Instrument Company, Inc.)**

Thermal Imagers can map a thermal distribution across a surface of a whole robot as shown by (Poonyapak and Hayes, 2006).

**Figure 22: Image of a pump (Source: FLIR Systems, Inc.)**

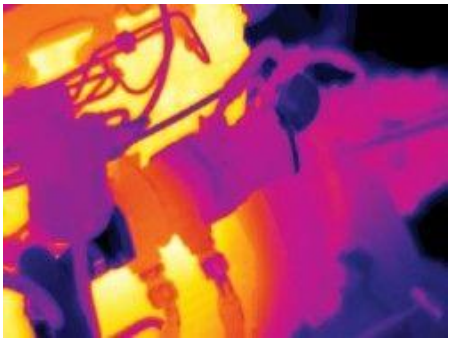

**Figure 23: Thermal image of pump (Source: FLIR Systems, Inc.)**

Temperature of a large surface can be observed with accuracies of the order of one to two degrees Celsius. For accurate temperature readings, calibration of the object against a known hot object is necessary. Imagers can produce data quickly if accurate measurements are not a key issue and only a relative thermal map is required. Thermal imaging cameras have been used on machine tools, spindles, and robots; monitoring where the heat produced may induce distortion (Mian et al., 2009). Thermal imaging of a micro-milling process at a microscopic level was carried out by Davies *et al.* (2005), high temperatures were observed at approximately 500°C to 900°C with inaccuracies of up to 12°C and variation of 100°C observed in their results. Readings were obtained with a custom made infra-red microscope.

Poonyapak and Hayes (2006) used a thermal imager with a CCD device to map the temperature increase relative to changes in geometric performance and observed -140µm variation in the Y axis and +55µm in the X axis with a thermal increase of 4.70°C and 6.75 °C respectively. Typical results from a thermal imager are shown in Figure 23.

## 2.4 Compensation strategies for machine tools and robots

This section looks at the different methods for the implementation of compensation strategies and possible application to robot systems.

With robots, it is common to find errors of up to several millimetres but with good repeatability it is possible to compensate for these errors. When thermal effects are present and repeatable, these too will need to be added to the compensation strategy. The majority of the literature relating compensation models or geometric models involve the Denavit-Hartenberg tables and transformation matrices, going from the base frame of reference to the end effector. It is often an additional adaptation to this, that the robot kinematics are produced in order to give more accurate results.

### 2.4.1 Temperature control

This section reviews different approaches for maintaining machines in a thermally stable state, temperature controlled laboratories, applying thermal models, placing machines in cool boxes and using specialized equipment to keep the temperatures down.

Two methods for reduction of temperature drift are stated by Reinhart *et al.* (1998): “Minimization of disturbance inputs through design measures (primary measures)” and “Minimization of effects through compensating measures (Secondary measures)”. From the primary measures, they state how the design of the robot allows the thermal changes to be distributed symmetrically and introduced as part of the thermal parameters in the kinematic model. In order to identify these parameters a thermal model can be created, in this paper FEM is used to calculate distortion from the lengths of the robot links and material expansion co-efficients. This is known as the bottom up approach. The top down approach they also discuss is to measure the position of the tool centre point with respect to its intended position during long term tests incorporating several load profiles.

Most research into error compensation arises from computer controlled methods and online/offline changes to an algorithm based on some initial measurements of temperature and deformation (secondary measures). There is the use of coolants being applied such as a mist spray for cutting with a drill bit. Other methods include a factory having specially temperature controlled rooms in some cases to better than one degree Celsius accuracy. In some situations machines are placed in special boxes so as to keep the machine temperature even more strictly controlled (Bryan, 1990) and (DeBra et al., 1986).

Other situations exist where there is no temperature control happening in a room where machining is occurring such as a car factory floor and as such, other factors may be more useful such as using machine controller compensation techniques.

A thermal model of machine tools was developed by Attia *et al.* (1999) incorporating a new s-domain Inverse Heat Conduction Problem (ICHP) solver with a developed Laplace procedure to improve the computational efficiency of the solver in predicting thermal errors. Accuracy and stability are retained while the speed of the solver is an order of magnitude above other methods mentioned in the paper such as function specification (FS); Stoltz, Regularization methods (RM), Space Marching Methods (SMM), Monte Carlo Methods, Iterative Regularization, Mollification methods and more. The S-domain (ICHP) solver method can be used in many different types of machine tools due to its general formulation and solution algorithm.

Mendes *et al.* (2001) uses matlab/Simulink for thermal modelling and analysing thermal performance and temperature control methods. They look at possible variations and discuss how most temperature controlled environments do not consider, thermal inertia, conduction heat fluxes, envelope thermal capacity, lighting and people loads, infiltration, fenestration and thermal inertia of heating systems. They show that traditional on off strategies demand higher energy inputs. Also they find that the temperature difference at the on-off points of temperature control devices are very different, which causes even bigger implications for accurate temperature controlled laboratories.

Thermal error analysis by Eastwood and Webb (2009) is implemented for error reduction in robots. The results from their paper show that thermal drifts of 200µm to 780µm in the X and Z motion were reduced to less than 50µm, an 84% reduction in thermal error. For a 17°C to 50°C temperature variation in the robot, a deviation in the tool centre point vector magnitude of up to 780µm and at best 60µm was observed. The paper suggests strategies for making an error analysis methodology and suggests that information from temperatures and deformation measurements to be fed into the compensation strategy.

A recent summary of robot control systems (Brogårdh, 2007) suggests that in the future, these need to take into consideration the temperature variations a robot will be subject to, so as to model the mechanical stress of structures within the robot. This could be done in real time with dynamic robot models.

### 2.4.2 Offline compensation techniques

Offline compensation techniques are commonly used by researchers to improve machine tool and robot accuracy. Typically tests are run and then measurements taken to implement into a thermal distortion model to improve a machines performance. The program from the thermal compensation is normally applied through the controller. To validate the compensation, machining is re-assessed again to check for thermal deformations.

In their description of Environmental and Thermal Effects, the research group Heisel *et al.* (1997) look at ambient temperature effects on a six axis robot and a SCARA robot. They compensate for the thermal errors, reducing from 200μm in the X and Z axis to 80μm by 50μm in the X and Z respectively. In compensation strategies they find it is better to take measurements of the positional and path accuracies for obtaining a thermal error map of the robot rather than to model all the different thermal effects.

Improvements to a machines error predictive model can be shown to reduce errors by at least 60% (Alici and Shirinzadeh, 2005). The method introduced in this paper uses third and fourth order Fourier polynomials and second harmonics. Their approach is novel since after an initial comparison of simulated results with experimental data, they do not need to carry out a second set of measurements. A laser tracker was used to monitor the path of a motorman SK120 robot manipulator. A kinematic model is developed with an estimation of kinematic parameters using both the interior reflective Newton method and Levenburg-Marquardt methods. They found both methods produce the same numerical results. The inaccuracies in the manipulator are predicted and they find that compared to the initial nominal values for the parameters, when the 18 parameters are identified the improvement is from -5mm to 5mm to -2mm to 2.5mm.

Kim *et al.* (2004) uses thermal mode analysis and an If-then routine in the compensation method to predict thermal drift errors in the vertical type high speed machine tool (HSMT) as a black box and for predicting axial offset. The

machine spindle had T-type thermocouples placed on it and dummy cut routines done to find the thermal mode gains. Sets of data are produced for different spindle speeds. Overall an improvement from 40µm to 10µm in X and 70µm to 10µm in Z was achieved.

Creighton *et al.* (2010) ran a test on a spindle assembly and modelled using (FEA) the thermal errors. They then carried out measurements which show a thermal error of 6µm in-line with the model prediction. Compensation allowed the thermal error to be reduced to 1µm.

Offline compensation for modelling the robot and spindle assembly during motion as a result of thermal effects would be beneficial for the robotic smoothing process considering the thermal errors introduced and the most practical of the above methods may be utilised for this task.

### 2.4.3 Online compensation techniques

This section considers methods used by researchers in having thermal measure actively inbed with compensation systems in real time. These concepts are also presented in relation to the intended robot application.

Reinhart *et al.* (1998) uses thermal parameters introduced into the kinematic model of the robot which calculate thermal effects and then applied these to the robot controller. They find that during a heating/cooling cycle, robot deviations were reduced from a maximum just over 500µm to 100µm.

Eastwood and Webb (2009) develop an error significance analysis for combining different errors and their effect on a Hybrid Kinematic Parallel Manipulator (HKPM). This could be applied to other robots and machine tools. There is a scale of one to ten which considers the percentage of how often an error occurs and also the magnitude of the error in the machine. The advantage of this approach is that it can take into account multiple types and sources of errors and have them applied to the machine tool. They find from a 40kg load, error deformations in the X axis are (x, y) (300µm, 400µm), Y axis (x, y) by (400µm, 300µm) are reduced by 70% after compensation. They also reduce

mass deflection errors by 70% which is also useful due to the different loads a robot will have, as more weight is attached to the end effector. Applying this to the robot, which is under investigation, would be useful as the thermal affects that will be compensated for with a 34kg spindle mass and after all the other equipment which will be added to the end effector, the total mass may be close to 50kg limit of the robot. The load compensation brings the compensated value to within 20µm of the value of no load deflection. This would then produce more accurate positional data. This can be applied to the robot in this project as they mention that their kinematic model would need to be changed to be suitable for other robots. They suggest that the temperature modelling be developed and since they only use three thermocouples to obtain temperatures in the motors, it would be necessary to change and develop the thermal model. As a result a variation of the Error Significance Analysis would be developed (ESA).

In 1994 an improvement to modelling techniques was done by (Yang et al., 1996). The algorithm applied learns and predicts thermal effects. It was more accurate in predicting the thermal errors than other methods tested. Their model showed that there was at most a 10µm difference between experimental values and modelled/predicted values.

The thermal errors produced by robots can account for up to 16µm according to Oitzman and Campbell (2000) they suggest warming cycles for robots in order to bring the temperature of the different parts to operating temperature before producing an error map due to the thermal effects. They then produce an error map with a camera mounted system and a grid to produce the error map.

Work by a group (Gong et al., 2000) investigated robot errors. Robots position was monitored with a tracker and temperature variation was shown to be 10°C. The robot had a warm up time of five hours at 50% duty cycle with a seven hour cool time. They managed to reduce the errors an order of magnitude from a maximum 2mm down to 0.2mm, compensating for geometric, compliance, and thermal errors. Then taking into account the compliance errors further reduces the error from 0.126mm to 0.088mm. The thermal effects were monitored at 15 different positions and give mean residual errors of (1.0mm to 1.2mm), after

geometric and compliance compensation is applied this reduces to (0.1mm to 0.3mm). After, thermal effects are removed giving a (20µm to 190µm) improvement with (80µm -0.110µm) accuracy. Overall this is an order of magnitude improvement over the original errors observed. The robot was operated on at faster speeds than that proposed for this research.

# 3 Experimental methodology

In chapter two, different factors that influence machine tool and robot performance were reviewed, in addition to the methods for assessing the thermal and geometric performance of a serial robot. Furthermore, different compensation approaches via known or predetermined errors programmed into the robot controller for the robot end effector were also presented. This chapter will describe the approach used to assess the geometric and thermal performance of the smoothing cell robot. The objective was to determine the geometric performance of the robot, assess its thermal characteristics and, determine the thermal influences on the geometric performance.

## 3.1 Geometric assessment

The initial geometric assessment in the “cool” state without induced heat was ascertained using a combination of a laser tracker and a Renishaw laser interferometer over linear and circular motion paths, in line with the intended use as a smoothing tool. Measurements were also taken in accordance with the ISO standard (ISO 9283, 1998) for robots. In order to assess accuracy and repeatability in the positioning measurements of the robot, the end effector was moved linearly at 20mm/s in the X Y and Z axes to specified co-ordinates at stationary fixed points. The other linear positioning program measured the repeatability of the robot at the same co-ordinates as before, while moving fast at 100mm/s in continuous motion. It underwent a type of raster path from the initial co-ordinate to other points along the axis as before, until all points were measured to at least nine times. The method selected for both of the motions is referred to as Fine on the Fanuc robot controller and CNT0 for the ISO path.

### 3.1.1 Smoothing axes accuracy and repeatability

The accuracy of the smoothing robot was tested in the proposed plane (XY) operation. The X and Y axis were assessed with the laser interferometer, while the laser tracker was used to measure the Z axis. The tracker was also used to measure the overshoot repeatability in all three axes, the circular motion and

the ISO standard because of its suitability for volumetric measurement. These measurements without induced heat provided the geometric assessment of the robot's base performance when cold.

A laser interferometer was used to assess the robots geometric performance in the smoothing plane. It provided higher accuracy geometric data over a more limited range of motion, namely linear paths. The bidirectional linear motion in the robot's X and Y axes were tested. This was intended to assess the accuracy of the robot in both directions. The motions were akin to a raster smoothing process.

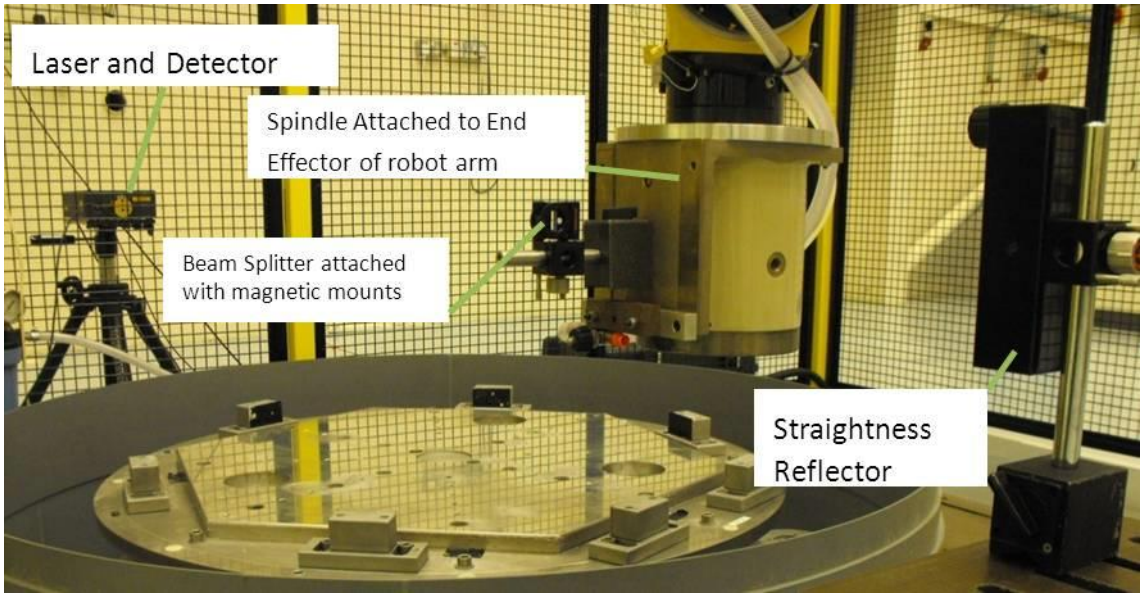


**Figure 24: Straightness in Z along linear motion in the Y axis**

In the Renishaw operator's manual, schematics of the laser paths split for straightness and linear positioning measurement are shown. The path differences of the two laser beams as the object being measured moves provides displacement or straightness data. The accuracy of the interferometer is sub-micrometre and most machines are tested with interferometers to gauge their performance. The reading stability of the wavelength of the laser is of hundreds of nanometres.

The straightness in the perpendicular directions to the motion of travel as well as the linear positioning ability, was assessed in order to measure the error

motion for the smoothing process. Each test consisted of 11 stationary point measurements 130mm apart, a total bidirectional motion of 2.6m.The end effector was moved at 20mm/s and held stationary at each co-ordinate, a measurement was then taken and repeated for each point along the whole axis in a bidirectional manner. In order to have a successful measurement of straightness in the perpendicular directions of motion, beam alignment was achieved to less than 40µm at each end of the motion. An image showing one such straightness measurement can be seen in Figure 24.

The linear positional measurements look at how accurate the robot is at moving to a point along the linear co-ordinate direction of motion. The interferometer was attached to the spindle and the retro reflector was stationary. The distance to the interferometer was changing as a result of the end effector's motion. Beam alignment and the removal of slope error with the robot end effector's motion was achieved.


**Figure 25: Robot and tracker setup**

A laser tracker (as illustrated in Figure 25) was used to make the volumetric measurements, Linear Z in the Z axis, circular path motion and an ISO path assessment. This is an interferometric based device measuring the divergence in the interference fringes to determine how much an object has moved (see

literature review sub-section 2.2.1 for the principle of operation). The stated traceable accuracy is 15μm + 6μm $m^{-1}$ therefore, over the full working stroke, for the Z axis (1m) measurement accuracy was 21μm, and for the XY plane (1.3m) accuracy was 22.8μm. The objective with the tracker was to check the robot's performance for geometric accuracy and repeatability in both circular and linear paths.

The laser tracker device was situated three meters from the base of the robot with the retro-reflector fixed onto the smoothing spindle which was bolted on to the robot's end effector.

Before every test, the tracker locked on to the retro-reflector and the home position of the robot was determined ('homed'). Similarly, once the laser tracker had locked on to the retro reflector, it remained focused on it for the duration of the measurements. From there on, the linear, spiral and circular motions were tracked and assessed.

The tracker system was equipped with a probe for measuring humidity and air temperature. This provided automatic compensation for changes in the refractive index of air for the laser path. For assessing the geometric accuracy two different types of measurements were made using the laser tracker. The measurements were taken as described below:

1. Linear: The measurement consisted of ten repetitions of a linear path along the Z axis 100mm apart in the robot's positive motion. The total length of the motion for the Z axis was 1m. 11 stationary measurement points were taken including the beginning and end of the path with the end effector moving at 20mm/s between measurements.

2. The geometric repeatability was measured in a circle motion of 1.3m in diameter to provide an assessment for the robot operating in a plane along the majority of the optic dimension of 1.45m. The end effector was moving at 100mm/s.

### 3.1.2 ISO standard

The ISO standard (ISO 9283, 1998) defines a number of paths for testing the accuracy and repeatability of industrial robots. Of these paths, two were used to assess the robot's overshoot repeatability in the X Y and Z axis as well as path repeatability for an ISO stated path. This is shown in Figure 26. To look at the repeatability, three areas were checked in greater detail.

Two of the ISO standard tests were used for assessment:

1. Standard test path repeatability: Check of the repeatability of defined points on a path defined by the ISO standard, see Figure 26. The end effector was moved at 100mm/s with the timed trigger on the laser tracker set at every 100ms.

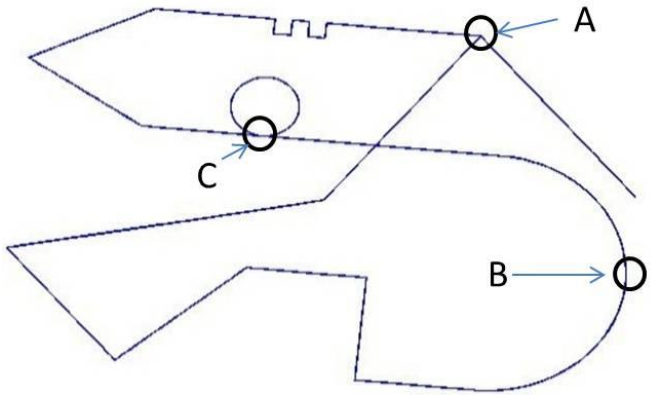


**Figure 26: Points of assessment for ISO standard**

2. Raster Measurement Repeatability: The end effector was moved at 100mm/s in a continuous raster motion repeatedly to pre-determined co-ordinates in a linear path (point 1, point 2, point 1, point 3, point 1 etc.). This was executed along the X Y and Z axes separately of the robot, see Figure 27. The repeatability of the measurement at which the end effector reached its programmed co-ordinates during continuous motion was assessed. Each measurement consisted of at least nine repetitions at the co-ordinate in that axis. As a result, the initial co-ordinate was measured 90 times. Only in the X axis did the last co-ordinate 2000mm

get measured 10 times. The end effector was moved at 100mm/s, with tracker timed trigger set at 50ms.

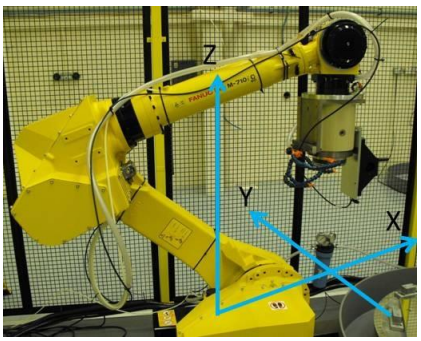


**Figure 27: Robot Cartesian co-ordinate system**

## 3.2 Thermal mapping

In order to create a thermal map and ascertain the key thermal areas of the robot a thermal imaging camera was used. The mapping was subsequently used to identify the areas for further investigation using thermocouples. The thermal mapping in addition provided information for the thermal model in the form of thermal temperature gradients along the robot arms.

### 3.2.1 Thermal mapping procedure

The thermal imager was used to assess the thermal characteristics of the smoothing cell. The imager uses the infrared radiation given off by a material and converts it into a representative colour image with the setup used in the uncalibrated mode, so as to provide the maximum intensity over multiple images.

The thermal imager used was a FLIRA320 with an accuracy of ±2°C or 2% of the reading (whichever is greater). The resolution was 320x240 pixels implying that an image representing $1m^2$ gave a pixel resolution of $1.30x10^{-5}m^2$. This provided the thermal map information required for the placement of the thermocouples.

The image of the complete robot structure was made up from a number of successive images in order to provide a reasonable image resolution, as illustrated in Figure 28, and Figure 29. For the reference images, the robot was measured when it was in a state where no work had been done.

The robot was then heated up via seven sets of spiral paths at 100mm/s for a mapping followed by the robot returning to the stretched out position shown in Figure 28. Mapping of the robot lasted approximately 10 minutes. The robot's time constant for cooling is well above this value and therefore, the temperature of the robot will not change significantly to impact the temperature measurements.

**Figure 28: Thermal imager positions to view robot**

The "heating" spiral path was repeated along with mapping seven times. The thermal maps were then analysed to determine key areas and effects.

### 3.2.2 Implementation of thermal profiles to modelling

The thermal profile of the robot arm served as temperature gradients to be mimicked by the thermal model. Each measurement had a duration of 30 seconds and this proved to be adequate since the temperature variation was minimal in that time.

The placement of the thermal imager in Figure 33, was positioned so as to view the first link length. This produces the thermal profile seen in Figure 31 and Figure 32. The information on the thermal map of the robot is shown in Figure 29. The vast majority of the heat is produced in the motors. The largest motors are located in the base and the smaller motors in the middle robot joint.

A typical gradient across the robot arm is illustrated in Figure 31 and Figure 32. The temperature ranges from the beginning of the joint at 26.5°C to the centre of the first link at 24°C. From there to the end of the first link length, the temperature approaches 29°C. The thermal profile gradient lines shown in Figure 30 do not go to the joint centre. Whereas the middle joint in Figure 29 and far right of Figure 30 is close to 30°C. Based on these profiles it was decided that exponentially increasing and decreasing lines would be representative of the thermal profile in the arm.

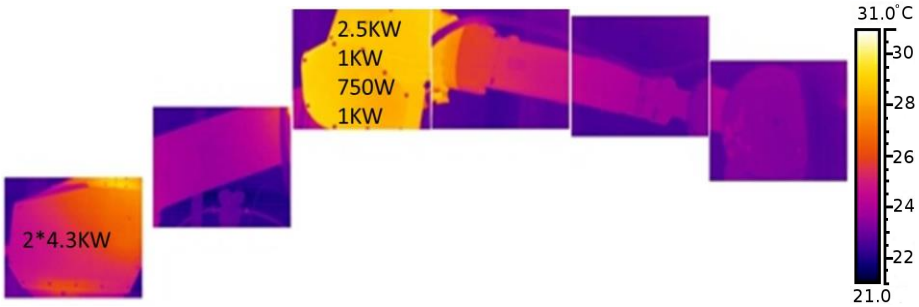


**Figure 29: Thermal image of robot arm**

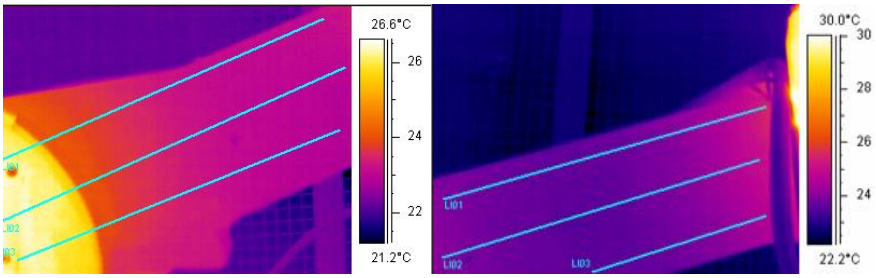


**Figure 30: Thermal image gradient lines along link 1**


**Figure 31: Thermal profile across link 1 first half**

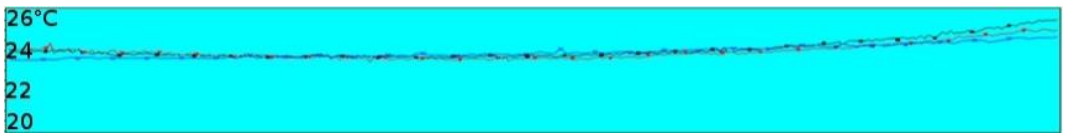


**Figure 32: Thermal profile across link 1 second half**

The temperature change during the thermal imaging measurements which lasted approximately 30 seconds each, were insignificant as can be seen by the variation at joint two (Figure 34) shown in the graph (Figure 35).

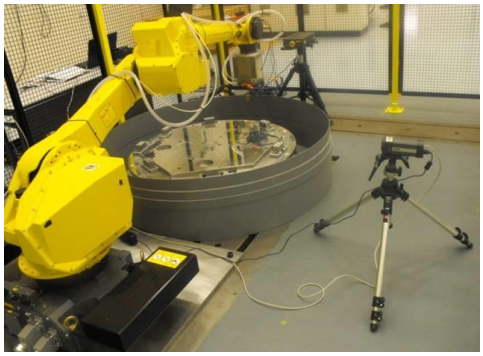

**Figure 33: Position of robot for mapping with the thermal imager**

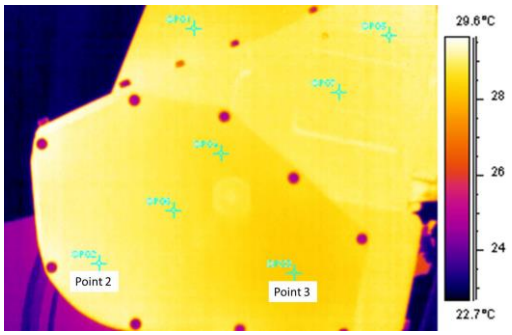


**Figure 34: Positions of thermocouples on robot joint two**

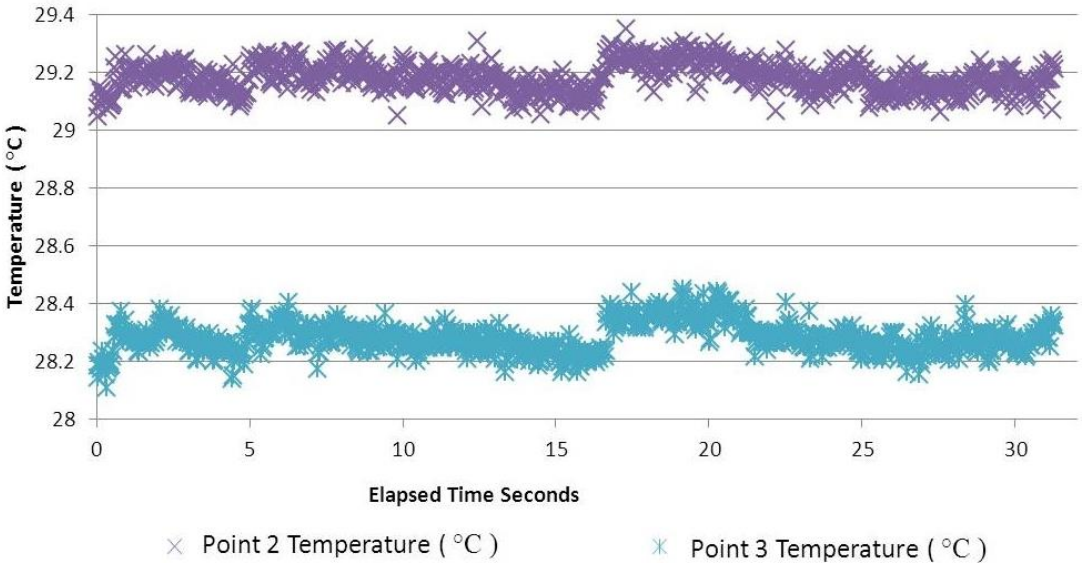


**Figure 35: Thermal variation during measurement duration**

## 3.3 Thermal assessment

Initial thermal assessment experiments were carried out so as to obtain a thermal map of the robot for the purpose of identifying the best positions for placement of the thermocouple probes for temperature measurement. The thermocouples gave more accurate information to the thermal model for the joint temperatures.

Geometric measurements were undertaken in conjunction with the temperature measurements to correlate thermal influences during the robot operation. A combination of laser tracker and interferometer measurements were used.

Heat was induced by moving the end effector at a speed of 100mm/s, five times that of the smoothing requirements (Ahmed et al., 2010). A spiral motion was utilised simulating that of the intended application.

The motors are the primary source of heat input. The first two motors control the lateral positioning of the end effector and the vertical motion of the first link. The remaining motors control the angle of the second link in the vertical direction, its roll and the spherical wrist of the robot's end effector. This also includes pitch and roll, totalling to six degrees of freedom, as shown in Figure 36.

**Figure 36: Six degrees of freedom on robot**

### 3.3.1 Initial temperature measurement system

Having used the thermal imager to identify the locations for more accurate temperature measurements, K type thermocouples (typical accuracy is to 2.2 °C) were used. Initially there were 11 temperature measurement positions in total with five more positions added later.

This level of temperature accuracy was considered adequate for this application. A temperature rise of 1.5°C causes a change in length of 34µm, based on a linear distortion of a 2.05m aluminium bar with an average co-efficient of expansion of 11.025µm $m^{-1}°C^{-1}$.

In order to map the thermal profile, circular trajectory tests were undertaken for a duration of approximately 30 minutes of continuous circular motion. Temperature measurements were taken as soon as possible after this motion and the robot had been made safe. For the Z linear measurements, the temperature was measured after each axis repetition was completed. For spiral trajectories, measurements were taken after five sets of spiral movements had been completed. This took approximately 10 minutes.

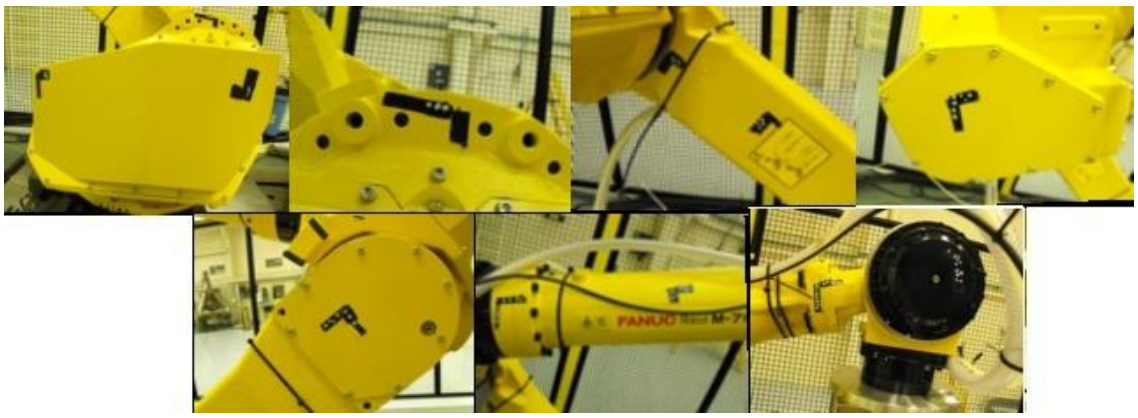

**Figure 37: Placement of thermocouples based on thermal map**

In order to monitor ambient temperature effects on the optic fixture, temperature was measured as shown in Figure 38.

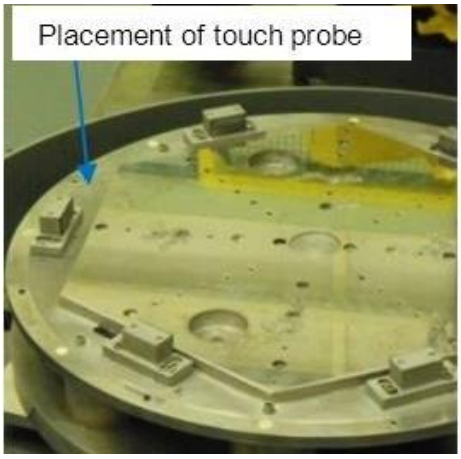


**Figure 38: Position of thermocouple on fixture**

### 3.3.2 Implementing the temperature measurement system

For the measurements which were carried out in conjunction with the interferometer, a real-time temperature measurement system was implemented. Measurements were made at the beginning and end of each assessment. This also provided input data for the temperatures of robot parts in the thermal model.

The thermocouples used on the robot were K Type as previously indicated. These had an accuracy of 1.5°C and were terminated with a Poly-Tetra-Fluro-Ethelene (PTFE) coated wire attached via a plug and socket to an insulated cable. This in turn had a connected plug to a data logging device.

The thermocouples were calibrated with the boiling point and freezing point of water 100°C and 0°C respectively. For 100°C, the thermocouples were placed in a kettle whilst for 0°C calibration point, they were placed in an ice bath as shown in Figure 39.

The thermocouples in the ice bath gave the results shown in Figure 40. From the graph on the ice calibration, the thermocouple readings are within 0.9°C of each other. This is well within their quoted accuracy. After they were placed in steam, in order to assess their ability to measure 100°C. During the cooling phase of the kettle, the values recorded by the thermocouples are within 1.5°C

of each other Figure 42. When the kettle was hot enough (as the water was boiling inside and steam was produced), the values were less than a degree Celsius apart. When the kettle stopped boiling water, the variation in the temperature reading on the thermocouples was about 1.5°C of each other.

**Figure 39: Views of ice bath for thermocouples calibration at zero**

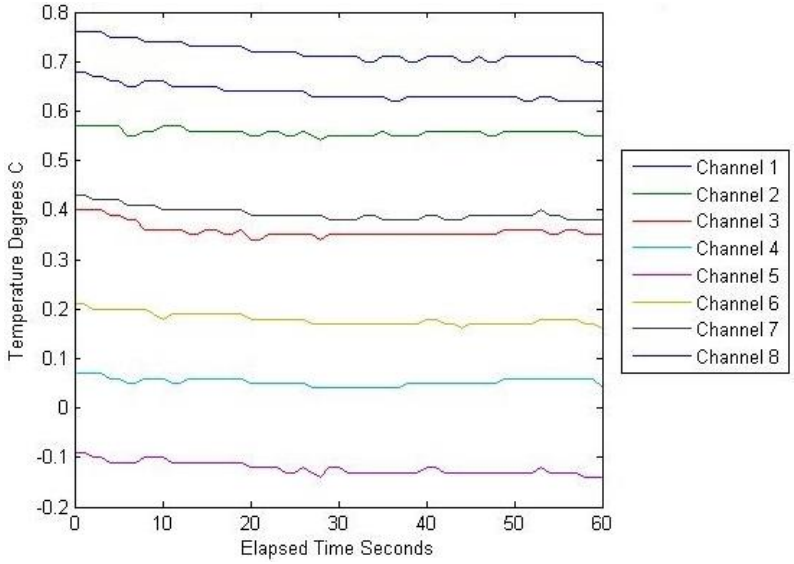


**Figure 40: Thermocouple responses in ice bath**

**Figure 41: Thermocouples in steam/boiling water calibration at 100°C**

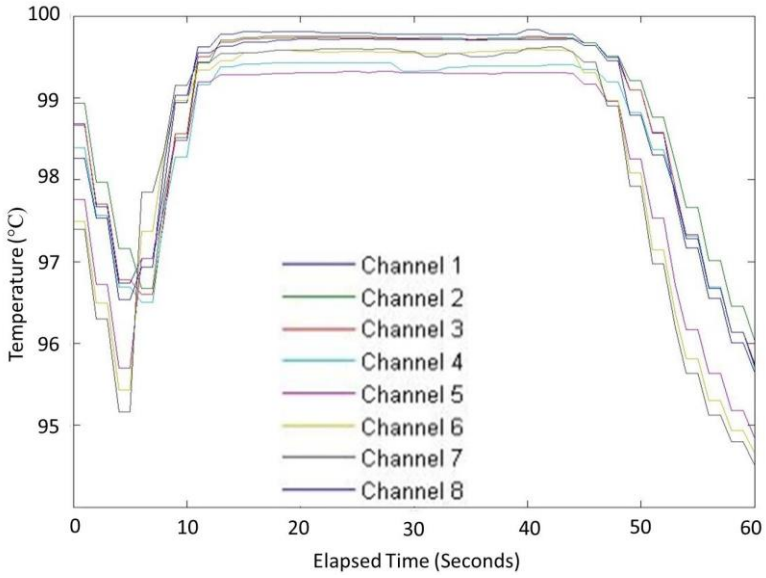


**Figure 42: Thermocouple response 100°C**

Following calibration, the thermocouples were attached to a metal surface of a copper plate fixture and tested as described below to verify functionality.

Thermal paste was used between the thermocouple and the metal surface to be measured. For providing a high level of thermal conductivity, aluminium tape and Kapton© tape were used to secure the thermocouples in place. Aluminium tape was used to provide additional thermal conduction to the surface as well as for fixing the thermocouple in place. Kapton© tape was used to retain the aluminium tape and thermocouple in place and provide isolation, as shown in Figure 43 and Figure 44.

**Figure 43: Thermocouple attachment method**

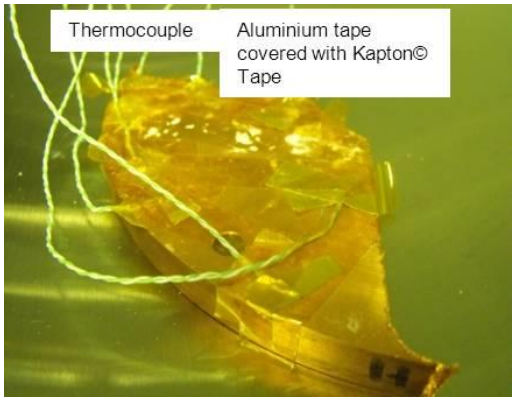


**Figure 44: Thermocouple testing in a temperature controlled oven**

To test this method and check the response of the thermocouples mounted as described, the copper plate fixture with the attached thermocouples was placed in a temperature controlled oven. The temperature was monitored over 9 hours from the early morning till day time within an oven turned off. The thermal responses of the thermocouples on the copper plate are similar to one another and within 0.5°C. There is slight cooling and warming due to the night time and the warming in morning, see Figure 45.

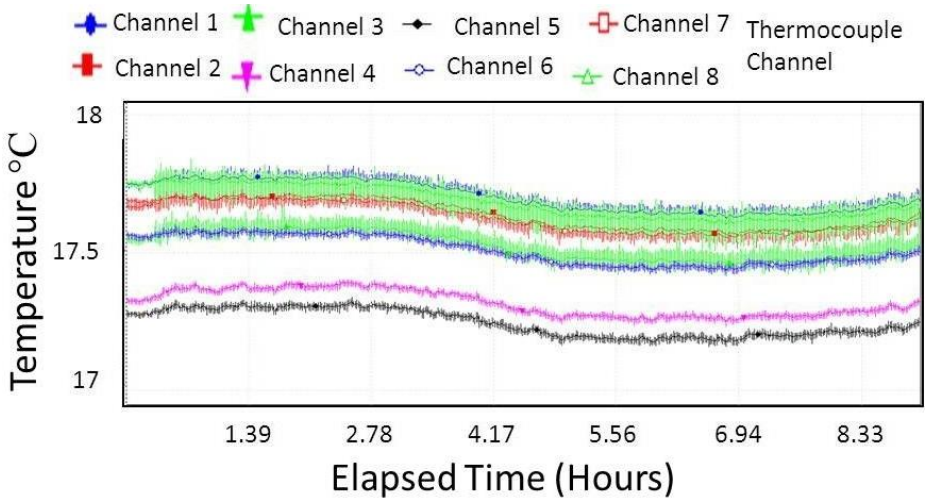


**Figure 45: Thermocouple on copper plate over nine hours ambient**

The oven was also heated to 80°C (Figure 46 and observing the cooling curve in Figure 47) to provide the thermal performance characteristic of the thermocouples over a temperature range. If left for longer, the temperature was expected to increase but the time was limited so power was turned off. As such, cooling was observed from 86°C to 83°C to 25°C to 26°C, in the space of two hours. The cooling curve shows exponential decay behaviour and the thermocouples stayed to within 2°C to each other.

Using Newton's law of cooling Equation 1, and measuring the temperature drop over time from the following equation, the thermal time constant of the copper plate can be estimated.

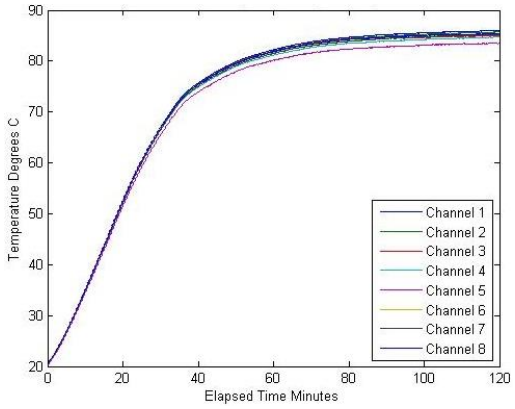


**Figure 46: Thermocouples heating to 80°C on copper plate**

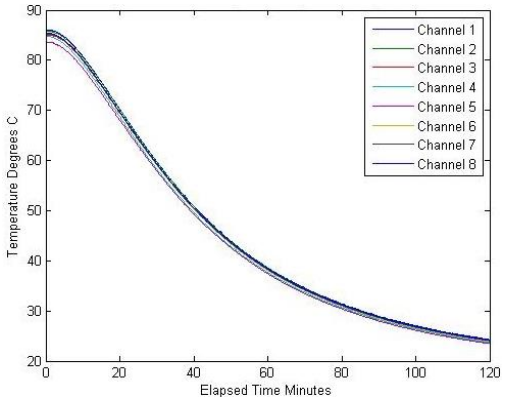


**Figure 47: Thermocouples Cooling from 80°C on copper plate**

**Equation 1: Newtons law of cooling**

$$\boldsymbol{F(t) = y_t e^{-kt}}$$

*Where:*

*F(t): is the temperature as a function of time of an object.*

*$y_t$: is the temperature after a period of time t.*

*k: is the thermal time constant of the material.*

*t: is the time length.*

After rearranging, Equation 2 is formed.

**Equation 2: Equation for thermal time constant**

$$\boldsymbol{k = \frac{ln\left(\frac{y_t}{y_0}\right)}{t}}$$

*Where*:

*$y_0$ is the initial temperature.*

*$y_t$ is the temperature after a period of time t.*

*k is the thermal time constant of the material.*

*t is the time length.*

Substituting the temperature values of 86°C and 25°C from Figure 47 in the equation and the cooling time of 120 minutes, the result for the thermal constant for copper is: $-0.103 \times 10^{-3}$ °C / minute.

This is for thermal conduction not convection. k is a function of the mass and thermal conductivity of the material. The value of k is positive when considering temperature increases rather than cooling.

The thermocouples were then placed onto the robot in the positions indicated and the signal cables passed to a datalogger, see Figure 48. The temperature sensor for compensation of the linear interferometer measurements, was placed along the first link. Seven of the available eight data logger channels were utilised to monitor the hot and cold points on the robot arm, as well as the ambient temperature.

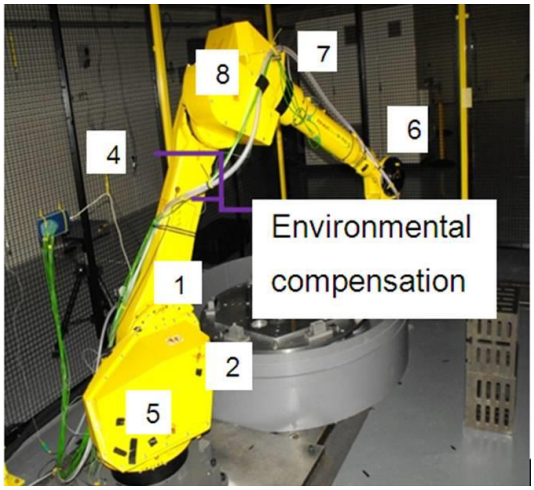


**Figure 48: Thermal key points on robot and their channels**

The interferometer used for geometric measurement was also set up to measure the humidity and temperature. This ensured that any affects attributed to changes in the refractive index of air were compensated for in the geometric result. Extra temperature measurement points were included using a handheld thermocouple during the laser interferometer tests. This complemented the real-time measurement system of thermocouples attached to the robot. Namely one extra on part one, three more on part six, and one extra for parts 10 and 11. Comparing Figure 37; to Figure 49, Figure 50 and Figure 51 shows the extra

points of measurement. This was carried out so as to gain more readings and to provide additional information of how the heat was distributed around each part of the robot. It was intended for this to provide an understanding on any twisting action currently not accounted for in the thermal model.

Readings were obtained to investigate if the sides of the robot near the robot motors heat up just as much as the top and to see if the connections for the spherical wrist show any thermal gradient. The spindle temperature was also monitored to detect if any of the temperature built up in the robot would be transferred to it.

### 3.3.3 Thermal effects

To assess whether there are any thermal effects on the robot, temperatures of the key thermal points were identified from thermal mapping. These produced the offline (user manually measures thermal key points after the robot is made safe) and online (operational regardless whether robot is stationary/made safe

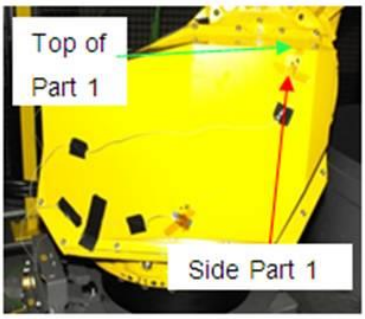


**Figure 49: Extra point of measurement part one (green), before (red)**

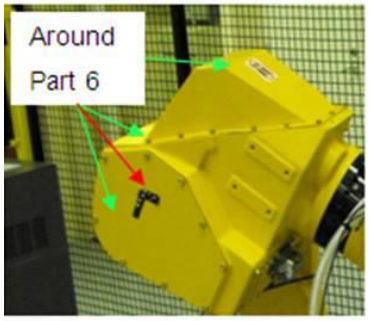


**Figure 50: Extra points of measurement part six (green), before (red)**

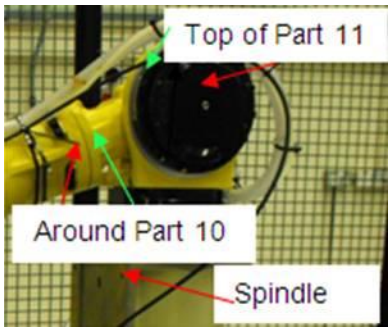


**Figure 51: Extra points of measurement parts (10 to 11) (green), before (red)**

or in motion and utilises a data logger) temperature measurement system. They were combined with the geometric measurements to associate any trend in the observations with the thermal output from the robot. A repeatable change in position with a corresponding change in temperature would imply a thermal effect. Thermal effects were assessed for Linear X, Y and Z motion. Circular

motion and spiral motion temperatures were measured to put into the thermal model.

For modelling the temperature of joints for different end effector paths, spirals, circles and linear motions were monitored. The spiral motion was fast at 100mm/s and lasted approximately three hours. Geometric measurements were made for the linear and circle motion. The linear motion was slow at 20mm/s, positioning at stationary co-ordinates. The duration of the assessment was three hours. The circular motion had two speeds at 100mm/s and 200mm/s, which lasted between five to eight hours.

This temperature data also provided information for the thermal model. Linear motion measurements were assessed for both cold and hot states. The thermal information was combined with the geometric data, so that a comparison was made between the motion for hot and cool states. This was done in order, to assess the thermal effects, as well as make comparisons on the accuracy of the thermal model predictions.

Thermal measurements were carried out with the thermocouple probe at positions indicated by Figure 49, Figure 50 and Figure 51 at the beginning of both the cold and hot geometric performance test. The online thermocouple measurement system was also utilised in order to provide more thermal performance data on the robot during its heat up cycle. Both measurements gave information as to how the temperature changes in the robot.

Linear positioning and straightness measurements were taken by the interferometer in the X and Y plane, as carried out for the geometric test (section 3.1) when the robot was cold. These measurements were repeated when the robot was hot. Measurements consisted of the bidirectional 11 point stationary measurements for straightness in perpendicular motion and linear positioning over 1.3m.

The cold bidirectional stationary positioning technique was used to assess the robot’s thermal performance and thermal effects. This was repeated four to ten

times. Then the robot was programmed to continuously move in a circular path with a diameter of 1.3m at 200mm/s motion for at least four and a half hours, to simulate worst operating conditions. When the robot was hot, the bi-directional motion was initiated again and any difference in the results outside of the possible error margin indicating a thermal effect.

The test for thermal effects in the Z axis along a 1m length, was carried out as the robot heated up from the mono-directional linear motion 11 point measurements. The thermal acquisition was done via the initial offline thermal measurements. This slow stationary positioning lasted approximately an hour.

# 4 Thermal modelling

In chapter 3, the method for carrying out thermal mapping, bidirectional linear positioning accuracy and repeatability, circle repeatability, ISO standard measurements and the thermal measurement system for detecting thermal effects was described. This chapter will explain the approach used to simulate thermal effects in the robot structure. In order to predict how the robot will behave with the different heat loads generated from a number of geometric paths, a geometric model is developed using thermal characteristics from test input contained in sections 5.2 and 5.3. This was used later to predict the path thermal effects. A comparison of the experimental results to the model's predictions is made in the discussion, this indicates how efficient the model will be for predicting thermal errors for future geometric paths the robot will move through. The thermal model was derived using thermal gradient data for slow linear motion at 20mm/s, spiral motion at 100mm/s and circular motions at 200mm/s. It does not take into account twist or bending of the robot arm.

## 4.1 Modelling strategies

This modelling approach will not cover an in depth analysis of how robots thermally distort but will focus on a basic linear expansion model to predict the thermal effects. This takes into account the intended smoothing operation at different speeds using temperature profiles and readings from the thermal performance results. This chapter covers the fully extended uniformly heated arm undergoing expansion, a non-uniform heat profile along the arm undergoing distortion.

### 4.1.1 Initial estimation

Initial estimation of the potential expansion can be made by considering a uniform temperature along a fully extended arm. The robot is made from a number of different metals. The base is made from cast iron, the robot arms are made from aluminium and the motors which are the major source of induced heat, are made predominantly from steel. Steel and iron have a co-efficient of

expansion of 10µm $m^{-1}$ $°C^{-1}$ to 15µm $m^{-1}$ $°C^{-1}$. Aluminium ranges from 17.5µm $m^{-1}$ $°C^{-1}$ to 27.5µm $m^{-1}$ $°C^{-1}$. Therefore an approximation for the co-efficient of expansion would be 11.25µm $m^{-1}$ $°C^{-1}$. This is half the mid-point of the co-efficient's of linear expansion for aluminium, and in the region for iron and steel. The hottest areas are akin to that from steel, hence the choice of co-efficient of thermal expansion. Using these approximations Figure 52 shows an estimation of the thermal expansion for the robot. A magnitude of up to 338µm for a temperature rise of 15°C is possible. This provided a guide for the instrumentation and approaches selected.

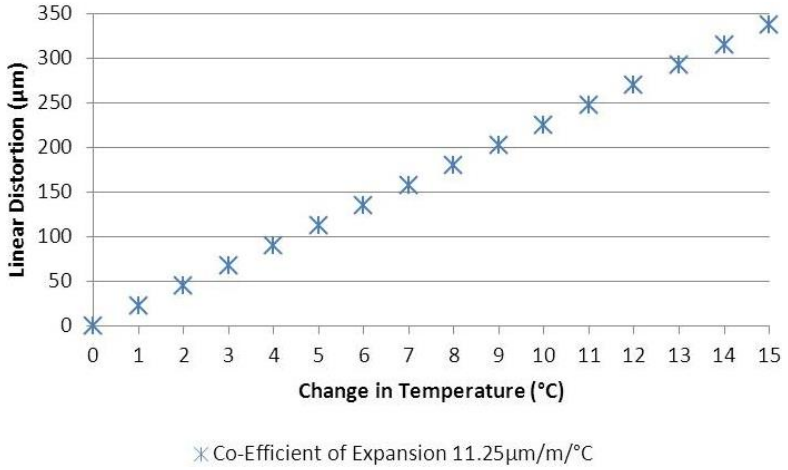


**Figure 52: Predicted expansion for a fully extended arm**

### 4.1.2 Linear distortion modelling: non-uniform thermal distribution

The robot will only heat up where the most work is done by the motors. This heat then transfers to the other parts primarily by conduction. The higher the motor power and the longer the duty cycle, the greater the intensity of heat produced.

The data obtained from the thermal mapping results in section 5.2, are used to provide a model for simulating a thermal gradient across the links of the robot. The thermal gradient will cause the arm to extend in length in a non-linear fashion. To model this behaviour, the peak temperatures of the heat sources which are the motors and gearboxes in the robot, need to be predicted. The temperatures of the joints in the model use the data contained in the thermal

performance section, see sub-section 5.3.2, Figure 125 for the linear motion at 20mm/s, Figure 127 and Figure 129 for the spiral and circular motion at 100mm/s respectively. For the faster circular motion of 200mm/s, the data is taken from the temperature profiles of Figure 110 and Figure 111.

Figure 31 from chapter three shows that the first section of the joint sees the highest thermal effect. There is a non-linear thermal profile from the joint to the beginning of the robot arm. After this point, a linear approximation to the thermal gradient across the arm can be used. The thermal profile information can be explained by the large change in masses, material and heat injection as shown in Figure 53. This would help to explain the rapid temperature decay in the far left of the temperature profile. The thermal distribution in the robot from joint one and two to the third joint in the middle of the structure, can be simulated with exponential temperature decays. The minimum temperature is slightly to the left of the link centre and the peak temperatures are at each end of the joints containing the motors. This is simulated with two exponential curves, each one will originate from the joint along a short section of the link. Thereafter a constant temperature will be simulated to the start of the exponential increase near joint three. To illustrate this, Figure 54 shows the structure and proposed thermal distribution.

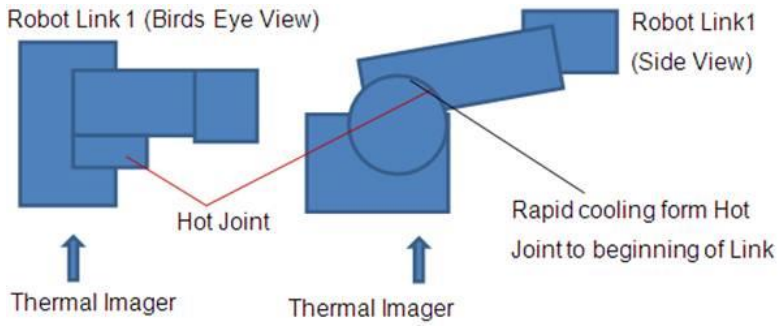


**Figure 53: Robot structure and rapid cooling from joint to arm**

Over time the height of the whole curve will change due to the contained heating from the motors. The results of the interferometer and tracker measurements indicate that for a linear path motion in X, Y, and Z, the temperature trend was linear, over a period of three hours. Non-linear thermal

increases resulted from circular motions at speeds of 200mm/s over six hours as shown by Figure 64, Figure 65, and Figure 66. The slow linear motion results in Figure 123 and Figure 124 respectively have been extrapolated and indicate that three hours or less of linear motion at 20mm/s, increases in temperature linearly. This is supported by Figure 129 and Figure 110 showing a 100mm/s and 200mm/s motion respectively. These figures show that a comparatively linear trend in heat occurs in the robot motors for less than three hours. Speeds less than this are assumed to cause similar behaviour.

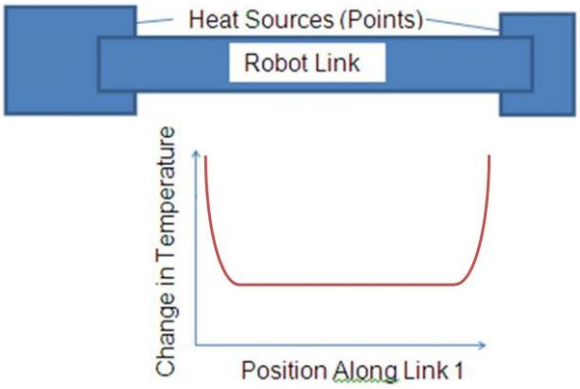


**Figure 54: Simulated thermal gradient across link 1**

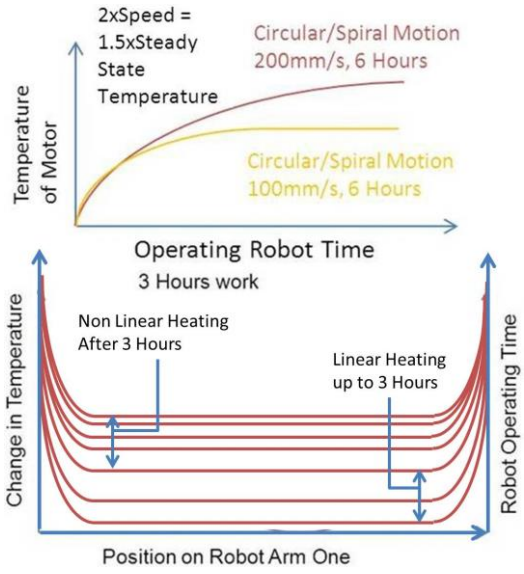


**Figure 55: Non-linear behaviour motor temperatures**

Different paths for the end effector will produce different temperature changes in each of the motors because for a circular path, the motor demands are different.

Whereas, for a linear path in X, the motor in the base of the robot does not operate at all to keep the end effector moving in the X axis. As a result the temperature across the link will be different. Spiral paths are shown to heat up slower than the circle paths because the size of the motions for a spiral, approximate a circle repeated at different diameters. By comparing Figure 127 and Figure 129 in sub-section 5.3.2, at approximately 80 minutes a 0.5°C difference is observed in the robot joints. The smaller the diameter, the less work the robot motors have to do, therefore less heat is produced.

The flow chart in Figure 56 shows the initial conditions for the model to obtain the temperature in the arm given the type of; motion of the end effector, the speed, and time duration. The flow charts later in the chapter provide further detail of how these initial conditions relate with the position of the robot's end effector, the kinematic model and resultant thermal effect.

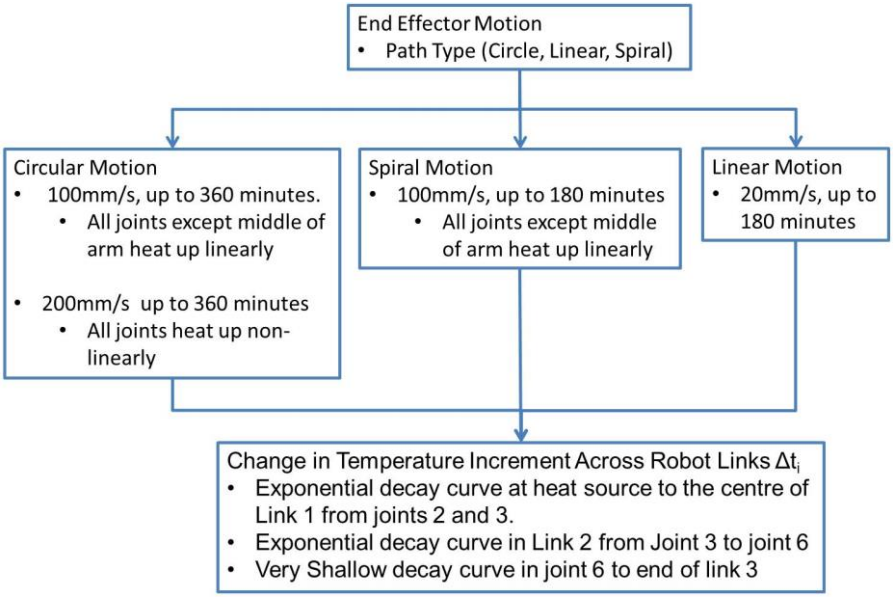


**Figure 56: Building blocks for offline temperature modelling**

There are two methods for modelling the thermal effect in the robot and applying the compensation methods. The first method is using offline compensation, to provide a compensation during smoothing. The other method uses online temperature measurements of the robot joints and links and

supplies this information to estimate the linear extension of the robot with a curve fitting tool.

The disadvantage for offline measurements is that the temperature profile is dependent on the path and motion of previous measurements. There was limited time available to produce all motions necessary on the robot at the relevant speeds. This did not allow a full thermal assessment of the robot at maximum speed for different paths. Assumptions are therefore made from a limited set of measurements on how the temperature behaves, based on the speed and type of motion the robot undergoes. This is covered in sub-section 5.3.1 Geometrical measurement.

The advantage in using the offline compensation is avoiding the constant calibration of temperature measuring devices, maintenance, feedback problems, interference in the signal, as well as ensuring that the devices remain interfaced with the robot during operation.

The flow chart in Figure 57 shows on the left side of the diagram an offline model and on the right side an online model for a compensation. For the offline model, the thermal expansion calculation is from the pre-set constants. These include the thermal expansion co-efficients and thermal gradient profiles across the links. These are combined with the predicted temperature input dependant on the speed, duration and motion of the robot end effector.

This thermal expansion calculation is either sent to a linear distortion program or a non-linear distortion program. The linear program assumes the robot arm is connected via links, with the thermal profile causing a non-uniform linear expansion in each link.

The non-linear distortion program is similar except it would consider the robot to twist and bend. These would be due to the different co-efficients of expansion from the other robot materials together with the twisting and bending of the structure, due to the parts fitted together in various orientations. As initially mentioned, non-linear distortion is not going to be modelled but a future

researcher could develop such a program for understanding how bending and twisting affect the robot end effector's position. The box in Figure 57 saying (Material Expansion) refers to the model that is being used. It could be purely a linear distortion program, or one that combines all linear, bending and twisting effects on the robot structure.

The linear distortion calculation from the thermal expansions in the different parts of the arm then become outputs that feed into a robot kinematic model, which in turn calculates the new position of the end effector of the robot.

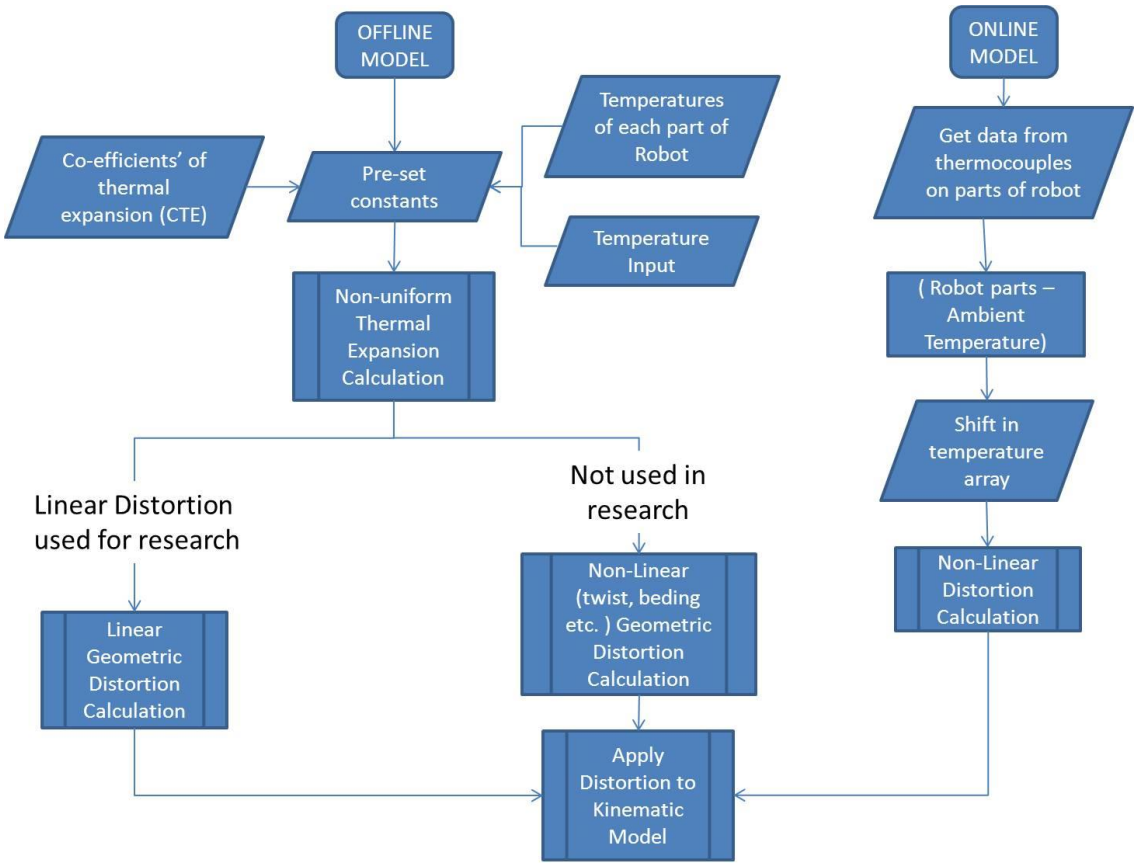


**Figure 57: Flow chart of thermal model**

For the online model, the joint temperatures and different sections along the arm are measured to create a thermal profile across the arm with a curve fitting tool based on previously measured thermal profiles and assumptions on how heat travels through a material. The initial ambient temperature at the beginning of the day would then be subtracted from the temperature measurement to get

the change in temperature. Following this, the new position and thermal effect are calculated as executed in the offline model.

## 4.2 Geometric model

Inverse kinematics is used to determine the angular positions of the robot links for pre-determined x, y, z co-ordinates. With the isolated robot link data, thermal calculations can be applied. Forward kinematics are then used to recalculate the new x, y, z robot co-ordinate. The old value will be taken away from the new value to give the thermal effect. From this, compensation can be recommended for the smoothing process.

### 4.2.1 Inverse kinematics

Inverse kinematics is the process by which given an end effector's co-ordinates a solution for the angles in the joints of the robot are found. Several methods exist and involve numerical solutions of transcendental equations.

The robot has six joints and for each joint the angle needs to be worked out for a given set of end effector co-ordinates. This enables the robot to position each of the joints appropriately, for its end effector to reach the desired co-ordinate positions in space.

The technique to work out the inverse kinematics for the transformation matrix is complicated and requires solutions to transcendental equations. If a solution for the angles in the robot's joints is not achievable for the end effector position, it means that the position required for the end effector is beyond what the angles in the robot joints can move it to. There are also joint singularities where the number of solutions reaches infinity for a particular position, due to the joint redundancies for a multiple degrees of freedom device. In a six degree of freedom manipulator such as a robot arm, there are six robot joints with motors and encoders. Each of these angles is worked out for a particular end effector position. The analytical solution to each of these angles can be found in text books, (Ellery, 2000) sub-section 6.12. Numerical solutions to these equations are also used. A matlab based robot toolbox (Corke, 1996) freely available for

download on the internet is utilised for this thermal model to obtain a numerical solution for the inverse kinematics.

### 4.2.2 Forward kinematics

Forward kinematics is the process by which the position of a robot's end effector is found, given the angles for each of the links between the joints in the robot arm.

To find the end effectors orientation and position there are two main methods. The most common method described in text books (Ellery, 2000), (Chritchlow, 1985), (Koivo, 1989) uses matrices. The most efficient one is using the quaternion method, this method has the advantage of using less computing resources (Sahul et al., 2008).

The robot can be considered as having separate Cartesian co-ordinate frames for each degree of freedom. Each of these can be described with a four by four matrix describing the orientation and position of the frame (Equation 3). The orientation of the end effector with respect to the base frame ($X_0$, $Y_0$, $Z_0$) is described in columns one to three by three vectors: $\vec{\boldsymbol{n}}$, $\vec{\boldsymbol{s}}$, and $\vec{\boldsymbol{a}}$. The vectors $\vec{\boldsymbol{n}}$ being in the negative $Z_0$, $\vec{\boldsymbol{s}}$ in the positive $Y_0$ and $\vec{\boldsymbol{a}}$ in the positive $X_0$, see (Ellery, 2000) sub-section 6.1.1. The rows represent the unit vectors ($\hat{\boldsymbol{\imath}}$, $\hat{\boldsymbol{\jmath}}$, $\widehat{\boldsymbol{k}}$) along each of the vectors $\vec{\boldsymbol{n}}$, $\vec{\boldsymbol{s}}$, and $\vec{\boldsymbol{a}}$. The position of the frame is described in column four. The first three columns in the fourth row show the perspective transformation along those vectors. The fourth row in column four is a single unit indicating the scale of the co-ordinate transformation unit vector.

The final position and orientation of the end effector is found by multiplying all the matrices. The robot has six joints and therefore will have six transformation matrices.

**Equation 3: Transformation matrix from start frame to robot's i$^{th}$ frame**

$$A_i^0 = \begin{pmatrix} \cos(\theta_i) & -\cos(\alpha_i)\sin(\theta_i) & \sin(\alpha_i)\sin(\theta_i) & a_i\cos(\theta_i) \\ \sin(\theta_i) & \cos(\alpha_i)\sin(\theta_i) & -\sin(\alpha_i)\cos(\theta_i) & a_i\sin(\theta_i) \\ 0 & \sin(\alpha_i) & \cos(\alpha_i) & d_i \\ 0 & 0 & 0 & 1 \end{pmatrix}$$

Where:

*i = subscript indici for the number of values for a given property, e.g. number of angles for a six axis revolute robot is six.*

*$a_i$ = perpendicular distance between the $z_i$ and $z_{i-1}$ axis (the length of the link).*

*$\theta_i$ = Angle of joint in the robot.*

*$d_i$ = Distance d between the joint axis normals ($x_i$ and $x_{i-1}$) offset (d).*

*$\alpha_i$ = Angle of rotation about the positive (counter clockwise) $x_i$ axis, measured to the positive $z_i$ axis.*

A description of the above can be found in Kiovo (1989). The Denavit Hartenberg (DH) table (see Table 1) describes these parameters in a concise manner for use in the matrix.

**Table 1: Denavit Hartenberg table for six joint robot**

| Joint | Distance d between the joint axis normals ($x_i$ and $x_{i-1}$) offset (d) variable only for prismatic joint | Link length(a) | Offset link twist angle between axis $Z_i$ and $Z_{i-1}$ (α) | Angle of joint θ (variable only for a revolute joint) |
|---|---|---|---|---|
| 1 | $d_1$ | $a_1$ | $\alpha_1$ | $\theta_1$ |
| 2 | $d_2$ | $a_2$ | $\alpha_2$ | $\theta_2$ |
| 3 | $d_3$ | $a_3$ | $\alpha_3$ | $\theta_3$ |
| 4 | $d_4$ | $a_4$ | $\alpha_4$ | $\theta_4$ |
| 5 | $d_5$ | $a_5$ | $\alpha_5$ | $\theta_5$ |
| 6 | $d_6$ | $a_6$ | $\alpha_6$ | $\theta_6$ |

In order to find the different parameters for the robot's structure, the reference co-ordinate frame needs to be chosen. The reference frame is made from the zero position co-ordinate system of the robot.

In a kinematic model, there are either prismatic or revolute joints. Revolute joints revolve robot links around an origin in a circular motion. In prismatic joints, the link is moved along the direction of motion (see Figure 58). In the first and last column of Table 1, the parameters describe the type of joint in the link. If prismatic, d is a variable in column one and θ is a constant in the last column, while if the joint is revolute, the variable and constant are reversed. The other parameters need to be found from the schematics that are provided by the manufacturer, or if not available, measurements of the different sections of the robot.

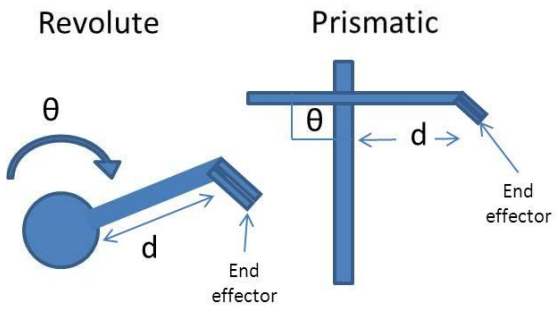


**Figure 58: Different motion of prismatic and revolute joints**

Each co-ordinate frame is assigned a set of axes, e.g. joint two, the ortho-normal axes of X, Y and Z, where Z is the direction along which a joint revolves around for a revolute joint and slides for a prismatic joint. The next set of parameters can be deduced by transforming the first robot frame to the next one until the end effector has its co-ordinate frame setup. In Figure 59, two joints are illustrated. This is showing that ($\alpha_{n+1}$) would be zero, because in this case the z axis for the frame has not needed to be rotated from frame $z_n$ to $z_{n+1}$. The value for ($d_{n+1}$) is also zero as the distance between the joint positions has the same value. If this were a prismatic joint, the angle of this joint would be a constant (θ) but the joints are revolute so ($\theta_i$) is a variable. The only parameter that would have a non-zero value would be (a) due to the distance between each of the joints or (d) if the frame being considered, is in another section of the robot links.

For the revolute model of the robot, the following schematic from the robot manual, as shown in Figure 60, was used to obtain the correct parameters. Robot parameters were applied to the robot toolbox (Corke, 1996) in Matlab for this particular robot model.

The schematic in Figure 60 shows the position of the robot with all the angles of the encoders in their zero position. The zero point of the co-ordinate system of the robot base is at position (0, 0). With the joint of the robot at position (0, 0), the next joint could be considered to be joint two +150mm to the right and 565mm in the vertical. Joint three would be +870mm in the vertical, parallel to joint two. Joint four would be considered 170mm vertical from joint three. Joint five would be considered in line with joint four and offset 1016mm to the right and joint six would be considered in line and offset 175mm from joint five. Joints four to six in this robot are considered as a spherical wrist, as all the axes intersect at the position of the end effector.

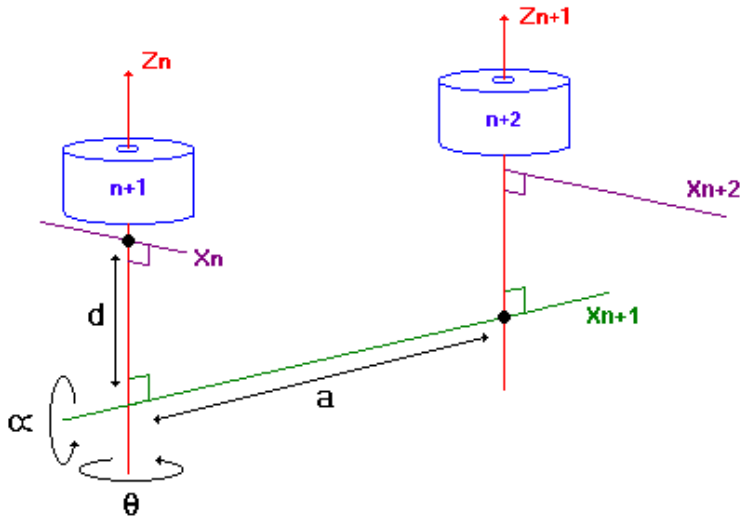


**Figure 59: DH parameters (Source: University of New Brunswick)**

These values shown in Table 2 are substituted into the relevant matrices and then the matrices (see Figure 61) are multiplied together from the base to the end effector as shown in Equation 4 and Equation 5. This calculates the final position and orientation of the end effector in the co-ordinate space, with respect to the original reference frame. The Denavit Hartenberg (DH) parameters for this robot model are contained in Table 2:

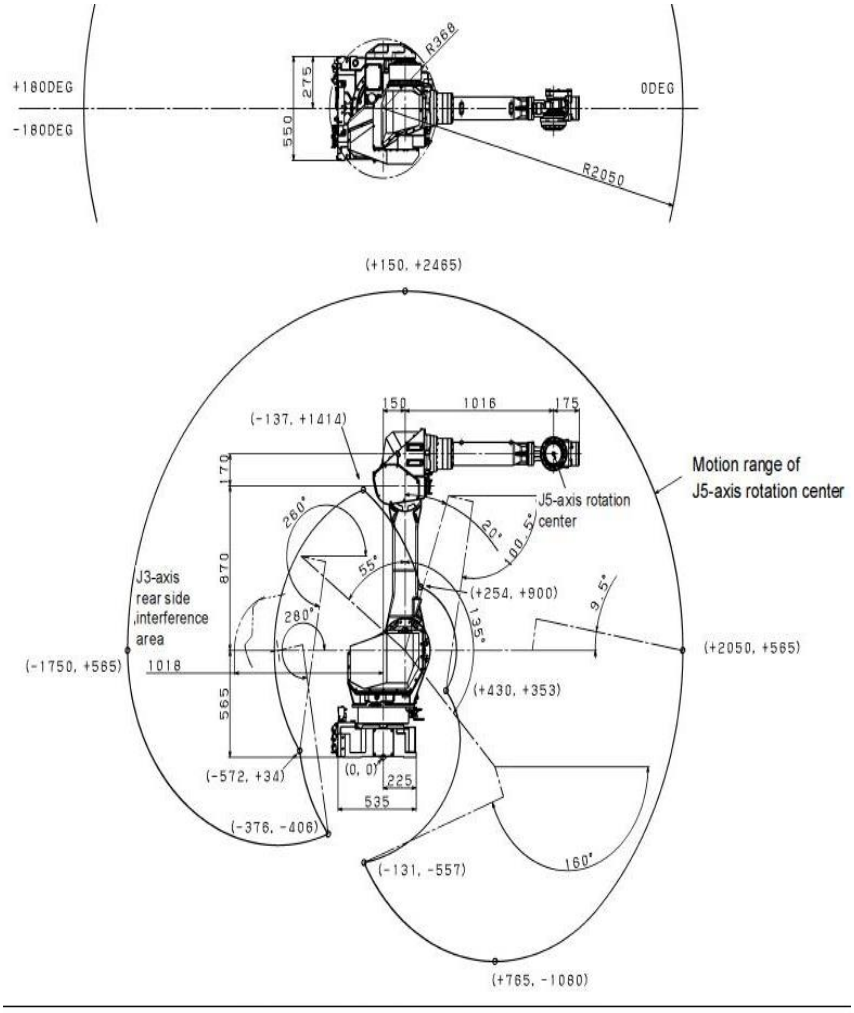


Fig. 3.2 (a) Interference area (M-710*iC*/50, /70)

**Figure 60: Fanuc robot 710iC/50 Source (Fanuc Robotics)**

**Table 2: DH parameters for Fanuc robot 710iC/50**

| Joint | Distance d in metres between the Joint axis normals ($x_i$ and $x_{i-1}$) Offset (d) Variable only for Prismatic Joint | Link Length (a) In metres | Offset Link Twist angle between Axis $Z_i$ and $Z_{i-1}$ (α) | Angle of Joint θ (Variable only for a revolute joint) |
|---|---|---|---|---|
| 1 | 0 | 0.15 | -π/2 | $\theta_1$ |
| 2 | 0 | 0.87 | π | $\theta_2$ |
| 3 | 0 | 0.17 | -π/2 | $\theta_3$ |
| 4 | -1.016 | 0 | π/2 | $\theta_4$ |
| 5 | 0 | 0 | -π/2 | $\theta_5$ |
| 6 | -0.175 | 0 | 0 | $\theta_6$ |

**Equation 4: Transformation robot's frame to end effector on robot**

$$T_6 = A_6^0 = A_1^0 A_2^1 A_3^2 A_4^3 A_5^4 A_6^5$$

**Equation 5: End effector transformation matrix**

$$T_i^0 = \begin{pmatrix} n_x & s_x & a_x & p_x \\ n_y & s_y & a_y & p_y \\ n_z & s_z & a_z & p_z \\ 0 & 0 & 0 & 1 \end{pmatrix}$$

The other method for working out the position of the end effector is to use quaternions. As previously mentioned the efficiency of quaternions over the transformation matrices method is higher as it requires less technical resources and requires less time to compute (Sahul et al., 2008). The toolbox available on the web for robotics in matlab has the facility to use quaternions (Corke, 1996).

A quaternion has two parts to it, a vector and a scalar. It is often labelled as in **Equation 6**:

**Equation 6: Quaternion expression**

$$\overrightarrow{\boldsymbol{q_i}} = \cos\left(\frac{\alpha_i}{2}\right) + \begin{bmatrix} a_i\hat{\boldsymbol{\imath}} \\ b_i\hat{\boldsymbol{\jmath}} \\ c_i\hat{\boldsymbol{k}} \end{bmatrix} \sin\left(\frac{\alpha_i}{2}\right)$$

where $\vec{\boldsymbol{q}}$ is the quaternion vector, $\alpha_i$ is the angle of rotation around the Z axis for the $i^{th}$ co-ordinate frame change, a b or c is the magnitude of the translation vector: ($\hat{\boldsymbol{\imath}}$, $\hat{\boldsymbol{\jmath}}$, $\hat{\boldsymbol{k}}$) are unit vectors in the respective x y and z axis where i is the subscript of the rotation vector, that may be the third or sixth translation rotation co-ordinate frame to get to the end effector position.

In the same sense that the matrices are multiplied together to reach the end effector position, so are the quaternions for each of the links of the robot. In this equation for $\overrightarrow{\boldsymbol{q_1}}$ to $\overrightarrow{\boldsymbol{q_6}}$, the parameters $\alpha_i$ and $d_i$ are inserted from the DH table for the robot and in this case would be obtained from Table 2 and put in place of $a_i$, $b_i$ or $c_i$. For a more thorough understanding of the use of quaternions in robots, the reader is advised to read (Koren, 1985).

## 4.3 Geometric and thermal modelling

In order to integrate the 'thermal and geometric' model, the inverse kinematics for each of the joints are found and have a thermal load applied to the links to provide a linear deformation. Forward kinematics are then carried out and the new end effector position and orientation, calculated. The thermal effect is calculated by subtracting the old end effector position values from the new one.

Predictions for various thermal effects on different robot paths given different temperatures along the robotic arm, can then be produced. Once the model has been validated against experimental data, other predictions could be made using motion paths and tests. This model could also be used as part of an online temperature measurement system, where the heat input can be fed in real time for predicting other thermal effects.

### 4.3.1 Applying thermal load to geometric model

Each matrix for the co-ordinate transformation has a heat load applied to each link expressed by the fourth column of the transformation matrix in Equation 7. Each matrix is then be multiplied together to give the final thermal effect at the end effector as shown in Equation 9. Depending on the heat loads throughout the robot, different thermal gradient will be present and resulting in a different thermal effect.

**Equation 7: Transformation matrix and linear heat input**

$$A^{0}_{i\ Hot} = \begin{pmatrix} \cos(\theta_i) & -\cos(\alpha_i)\sin(\theta_i) & \sin(\alpha_i)\sin(\theta_i) & a_i\cos(\theta_i) + a_i\cos(\theta_i)\times\Delta T_i\times CTE \\ \sin(\theta_i) & \cos(\alpha_i)\sin(\theta_i) & -\sin(\alpha_i)\cos(\theta_i) & a_i\sin(\theta_i) + a_i\sin(\theta_i)\times\Delta T_i\times CTE \\ 0 & \sin(\alpha_i) & \cos(\alpha_i) & d_i + d_i\times\Delta T_i\times CTE \\ 0 & 0 & 0 & 1 \end{pmatrix}$$

*Where:*

*i = subscript indici for the number of values for a given property, e.g. number of angles for a six axis revolute robot is six.*

*ΔT = Change in Temperature.*

*CTE = Co-efficient of Thermal Expansion for majority of link material along specified section* $a_{i.}$

If there is a thermal gradient along the link $a_i$ or $d_i$ for the spherical wrist, then the new thermal effect will have the temperature distribution applied to different points of that length. The constants $a_i$ and $d_i$ will then be split up into small elements and have the same linear equation for thermal expansion Equation 8 applied to it.

There are three links for the robot. The loop in Figure 61 shows that the thermal effects are to be applied to each link in the robot structure. Each link is split up into (n) millimetre elements along its length and has the thermal profiles from sub-section 5.2.1 applied to them. The linear distortion calculation is applied to the $j^{th}$ element of the link. This is contained in the fourth column of the geometric matrix and part of the parameters ($a_{i,j}$ and $d_{i,j}$) in the $i^{th}$ frame of the robot in Figure 61. Then a sum of the (n) element distortions is obtained to provide the overall thermal effect in the link. There are six co-ordinate frames represented by a matrix from the base to the end effector. Due to the simplicity of the model, only $a_2$, $d_4$ and $d_6$ have the applied thermal effect. These are the link lengths of the robot arm, the others are the co-ordinate transformations relating to the remaining orientations. A more complex model would take other parameters into consideration within the robot structure and therefore simulate bending, twist and other deformations.

**Equation 8: Application of thermal gradient to matrix**

$$A^0_{i\ Hot} = A^0_i + A^0_{iTi} = A^0_i + \begin{pmatrix} 0 & 0 & 0 & a_i\cos(\theta_i) + \left[a_i = (\Delta a_i \times \Delta T_i \times CTE_i)\right]\cos(\theta_i) \\ 0 & 0 & 0 & a_i\sin(\theta_i) + \left[a_i = (\Delta a_i \times \Delta T_i \times CTE_i)\right]\sin(\theta_i) \\ 0 & 0 & 0 & d_i + \left[d_i = (\Delta d_i \times \Delta T_i \times CTE_i)\right] \\ 0 & 0 & 0 & 1 \end{pmatrix}$$

*Where:*

*$CTE_i$ = Co-efficient of Thermal Expansion for Majority of Link Material along specified section $\Delta a_i$.*

Thus, to work out the position of the end effector when it is hot, the transformed matrices need to be multiplied together and the difference from this and the old

end effector position will be the thermal effect expressed by Equation 9 and Equation 10.

**Equation 9: Transformation matrix base frame to end effector of robot**

$$T^0_{6\ Hot} = A^0_{1\ T1} A^0_{2\ T2} A^0_{3\ T3} A^0_{4\ T4} A^0_{5\ T5} A^0_{6\ T6}$$

**Equation 10: Thermal effect at robot's end effector**

$$T^0_{6\ ThermalEffect} = T^0_{6Hot} - T^0_6$$

The flow chart in Figure 62 shows a summary of how the thermal and geometric model will work together to predict the thermal effect for a given end effector path motion.

In summary an initial set of co-ordinates are programmed and the inverse kinematics is done for each of the robot's joints in order to calculate the joint angles. After this, the thermal effect is found.

The thermal model creates the thermal profile along each robot link from the initial conditions of the robot paths. This is from the duration of work, end effector path and speed which the end effector is operating. When this is found the thermal effect on the robot link extension is then calculated and applied to the forward kinematic model, to produce a new end effector position. This thermal effect is then found by subtracting the old position from the new one. The thermal effect and new robot position will be for this initial co-ordinate. Thereafter, the next set of co-ordinates of the path for the end effector needs to be calculated. From this, the same process happens again until all the co-ordinates have their thermal effects calculated. Following this, a compensation can be formed for this path.

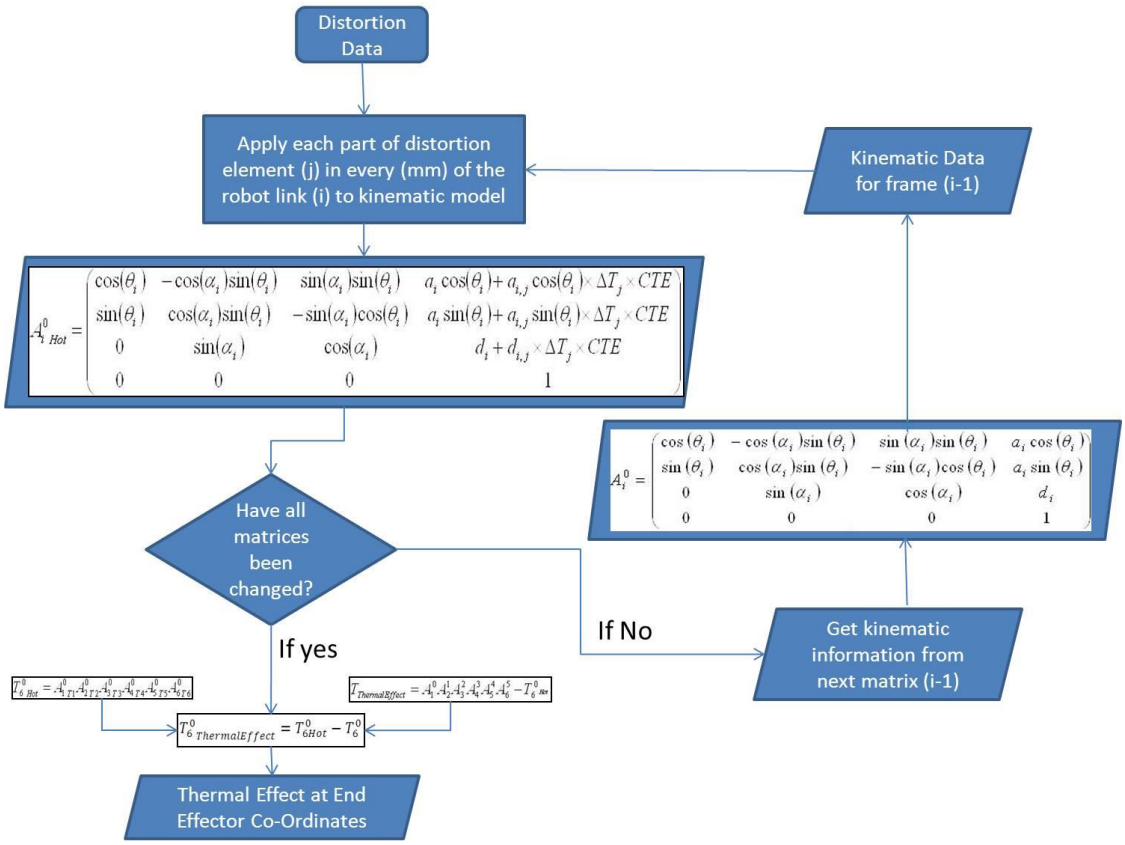


**Figure 61: Thermal calculation applied to kinematics**

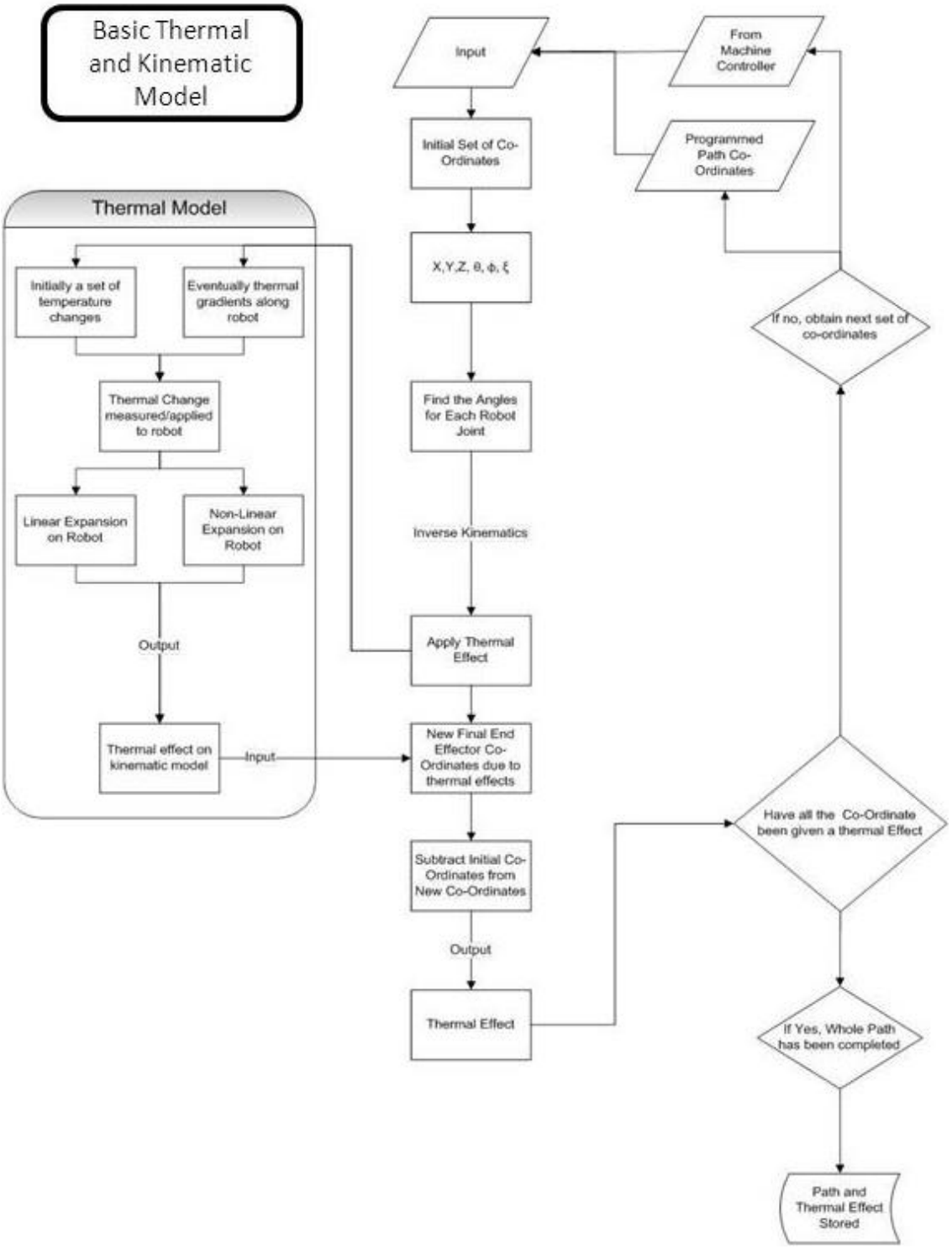


**Figure 62: Overview for thermal and geometric model for this study**

## 4.4 Thermal results

The initial results from the temperature distribution along a fully extended arm with the link lengths from the schematic (see Figure 60) as input parameters (a and d from Table 2) for the robot, and the thermal effects as a result are discussed.

### 4.4.1 Results for thermal modelling of robot arm

The temperature profile along the link length and time period together with the extension are shown in the first set of graphs over time see Figure 64, Figure 65, and Figure 66. The result that is shown in the thermal model is circular motion of the end effector moving fast at 200mm/s after six hours. This induces a heat load of up to 13°C in the hottest sections of the robot. This would be considered a worst case scenario of a smoothing operation. Some of the positions for the thermal model have the arm in the undesired orientation see Figure 63. In the X axis this is at positions 830mm and 1090mm, the Y axis does not have any issues and the Z axis has the arm in the reverse orientation for 303mm, 403mm, 603mm, 803mm and 1103mm.

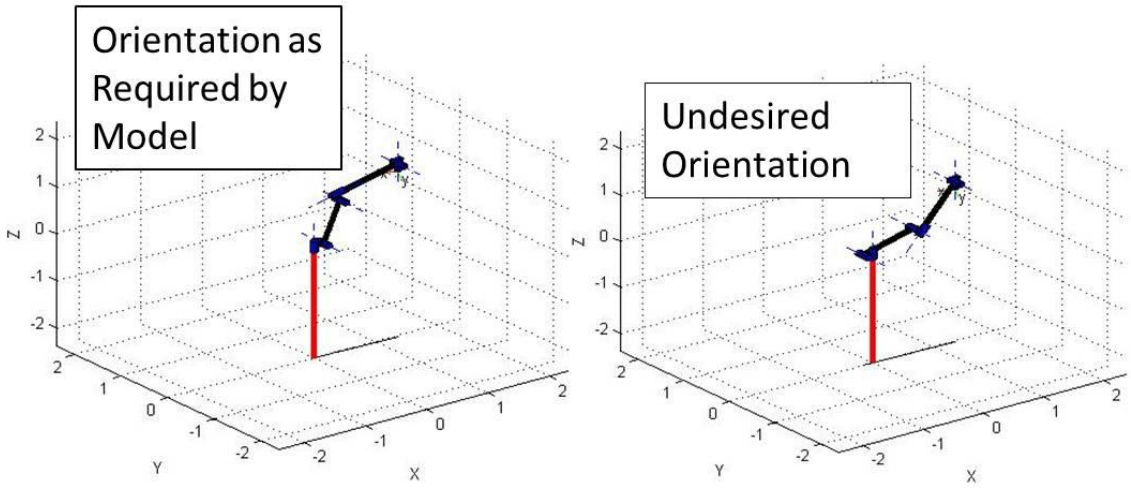


**Figure 63: Schematic of possible robot orienations (robot toolbox)**

The thermal profile of link one is shown in Figure 64. The end effector motion causes an exponential temperature increase along all the links. The edges of the link both have a greater thermal increase above ambient when compared to

the majority of the link's length. It shows the hottest part after six hours of work to be the middle section of the robot having a temperature above ambient of 13°C. From a base joint temperature of 11°C, there is a sharp exponential decay in the first 100mm to just less than 4°C, then a constant temperature for 450mm across the link. At 750mm along link one the temperature exponentially increases to 13°C.

The thermal profile of link two is shown in Figure 65. The thermal increase at the middle joint connects to the previous thermal profile of Figure 64. The end effector joint at the end of link two shows that as time goes on, the temperature increases up to 3°C above ambient.

The thermal profile of link three is shown in Figure 66. It joins to that in Figure 65. The temperature difference of the ends of link three is linear at 0.7°C so that the end of link three is 2.3°C above ambient.

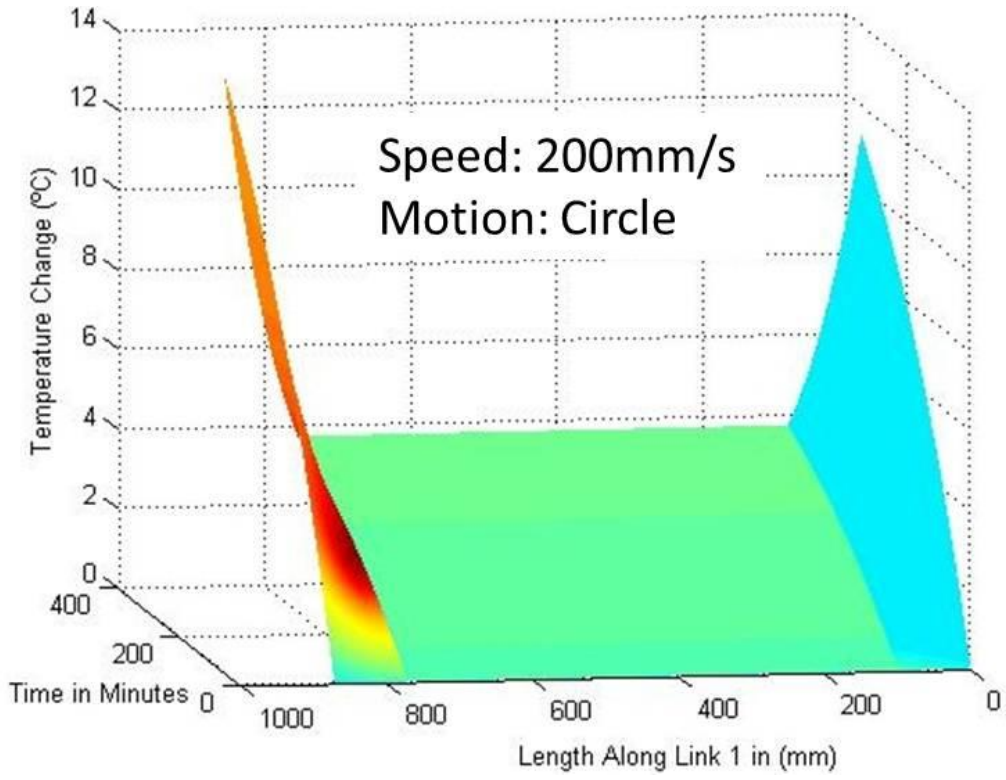


**Figure 64: Temperature profile extension link 1**

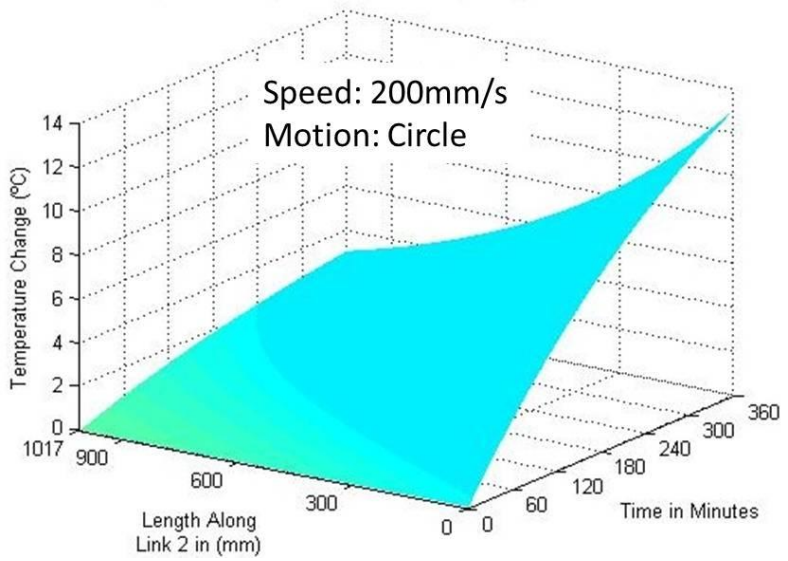


**Figure 65: Temperature Profile Extension link 2**

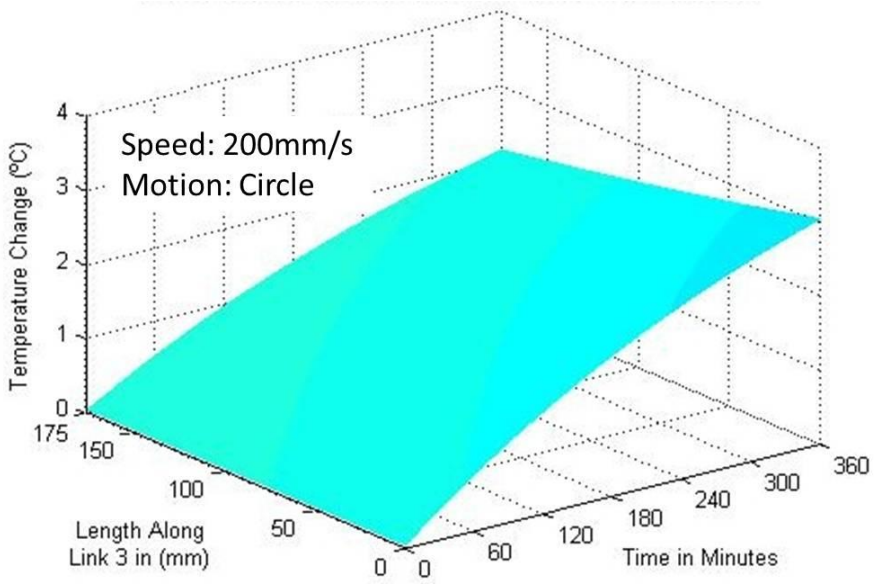


**Figure 66: Temperature profile extension link 3**

The thermal effect at the end effector is predicted for the linear motion in X in Figure 67. The thermal effect in linear positioning ranges from 70µm to 120µm. This increase from the initial co-ordinate to the end co-ordinate is expected due to the distortion of the different links combined together as a result of their orientation aligning. The straightness in Y shows at most a -3µm thermal effect while the straightness in Z shows a maximum of 20µm in the correct robot orientations.

The thermal effect in the Y axis is shown by Figure 68. The linear positioning has a thermal error prediction of -40µm in the initial co-ordinate and this reduces to zero in the mid-point of the robot axis. The thermal error continues to 40µm error at the end of the axis. For the straightness in X, the thermal error is 80µm. The straightness in Z error is 80µm at the start and in the rest of the motion of the end effector the error is -5µm.

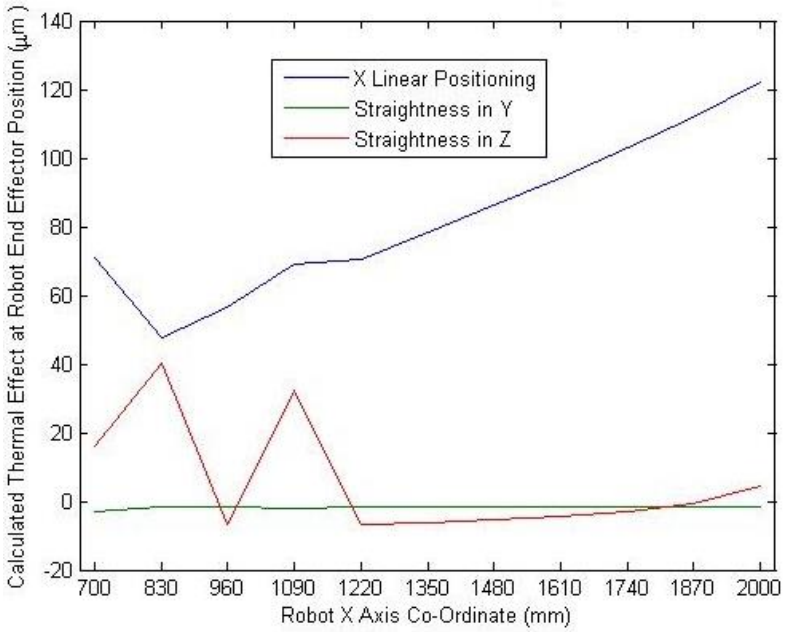


**Figure 67: Thermal effect at end effector for linear motion in X axis**

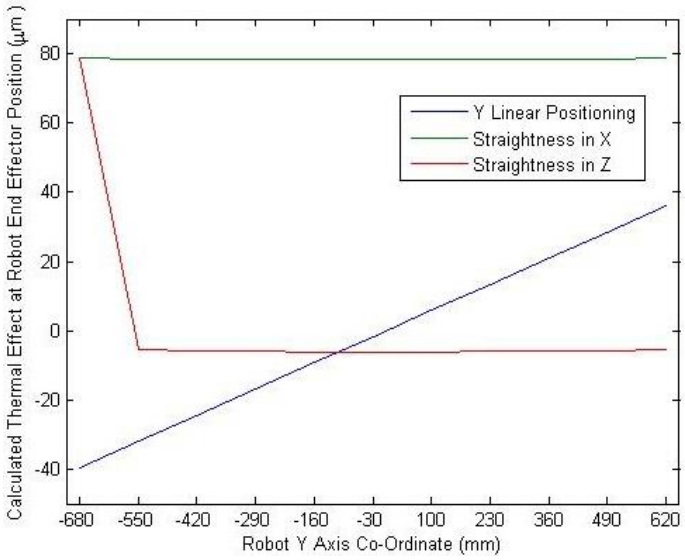


**Figure 68: Thermal effect at end effector for linear motion in Y axis**

The Z axis thermal effect is shown in Figure 69. There is an error in the linear positioning ranging from 77µm to 7µm, the straightness in X error ranges from 80µm to 90µm and the straightness in Y error is -3µm.

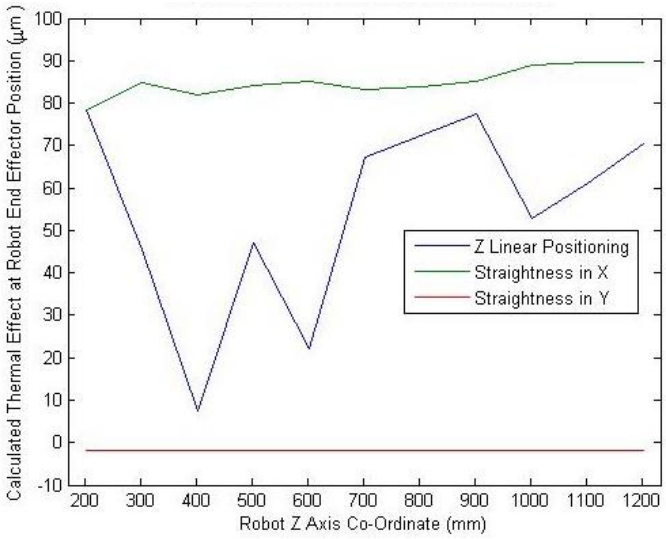


**Figure 69: Thermal effect at end effector for linear motion in Z axis**

The thermal effect at the end effector of the robot for spiral and circular motion moving at 200mm/s for six hours is shown in Figure 70 and Figure 71. The large circle has a 1.3m diameter while the concentric spiral has eight revolutions until its diameter is the same as that of the circle. The thermal effect is very similar to the spiral, except the spiral path shows the thermal error increasing gradually as the diameter of the circular motion increases.

For the circle path in Figure 70, the X and Y error motions have a phase difference between them of 90° polar angle. The X error motion peaks at 120µm and has its minimum at 50µm. The Y error motion has its peak at 40µm and minimum at -40µm. The Z error motion changes minimally in comparison to the X and Y error.

For the spiral path in Figure 71 the X and Y error are offset to each other by 90° polar angle and at the start have a difference of 80µm. The error in X slowly increases in amplitude. The overall error at the end of the spiral ranges from 50µm to 120µm. In the Y error, the error starts off at zero, like the X error the amplitude gradually increases so that the maximum errors are +30µm and

-30µm. The straightness in Z error marginally changes compared to the other two motions from -5µm to 5µm.

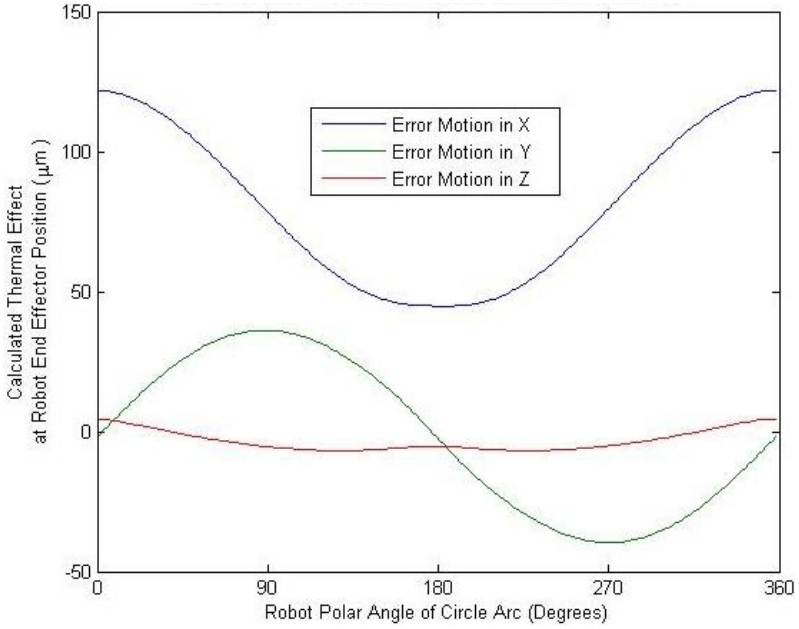


**Figure 70: Thermal effect at end effector circle path**

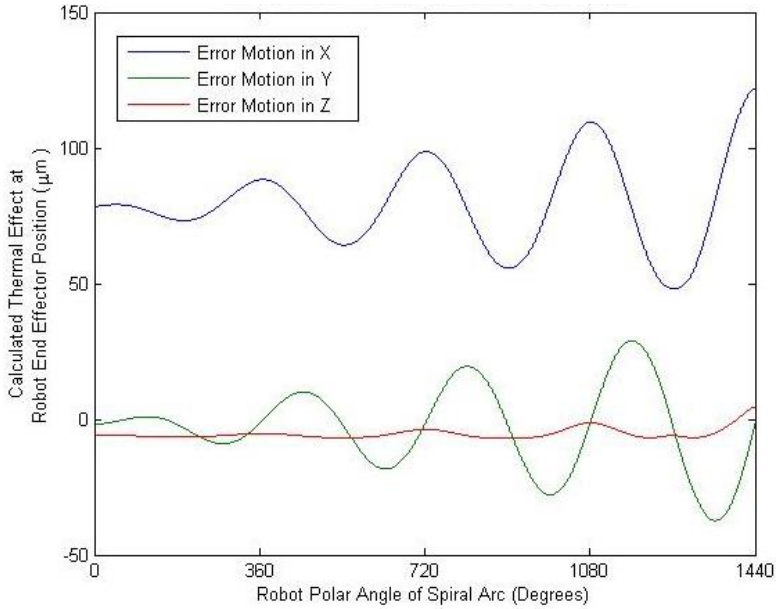


**Figure 71: Thermal effect at end effector spiral path**

# 5 Robot performance results

This chapter presents the results obtained from the geometric accuracy measurements of the thermal mapping of the robot, and finally the full thermal performance analysis. The thermal performance analysis provides the foundation for the thermal modelling and a recommendation for compensation proposed in the discussion chapter.

## 5.1 Geometric evaluation of the robot

The robot was assessed geometrically for linear path motion. The linear positioning as well as the lateral and vertical straightness in each axis was examined. The circular path motion was then analysed and finally measurements undertaken to ISO standards.

### 5.1.1 X Axis geometric accuracy

Results are presented for the X axis linear motion, both for displacement and straightness. All results are for the robot in a “cool” state i.e. without having undergone a working cycle.

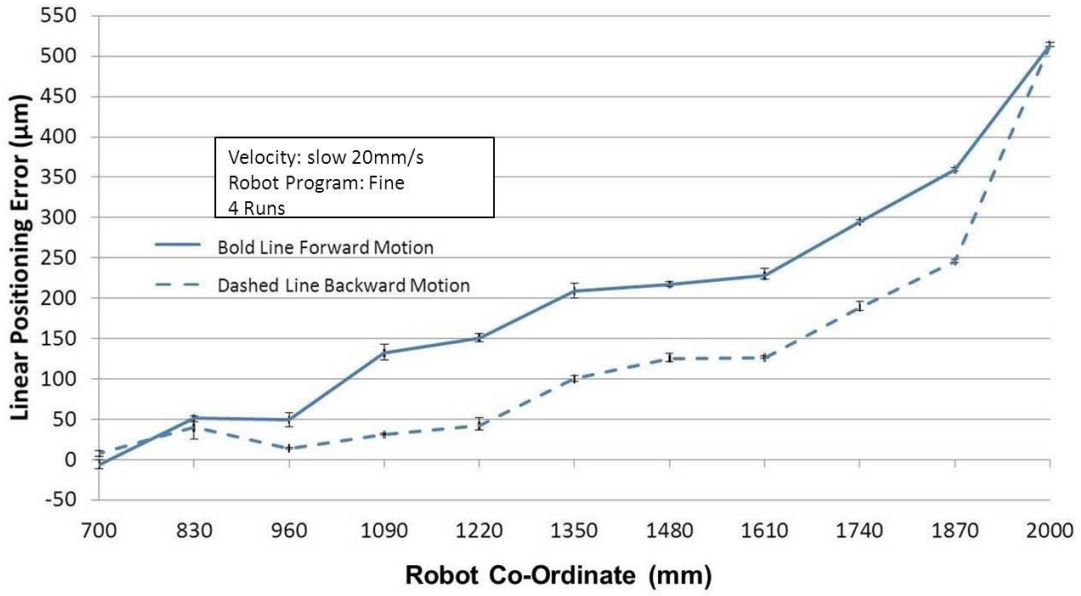


**Figure 72: Linear motion X axis linear positioning (X direction)**

Figure 72 shows the X axis motion; linear positioning error. It shows a maximum error of 525µm at the full travel (2,000mm). The forwards and reverse result demonstrates that the robot has hysteresis. The maximum deviation between direction being 110µm at x co-ordinate of 1870mm. Repeatability is good at less than 25µm (error bars).

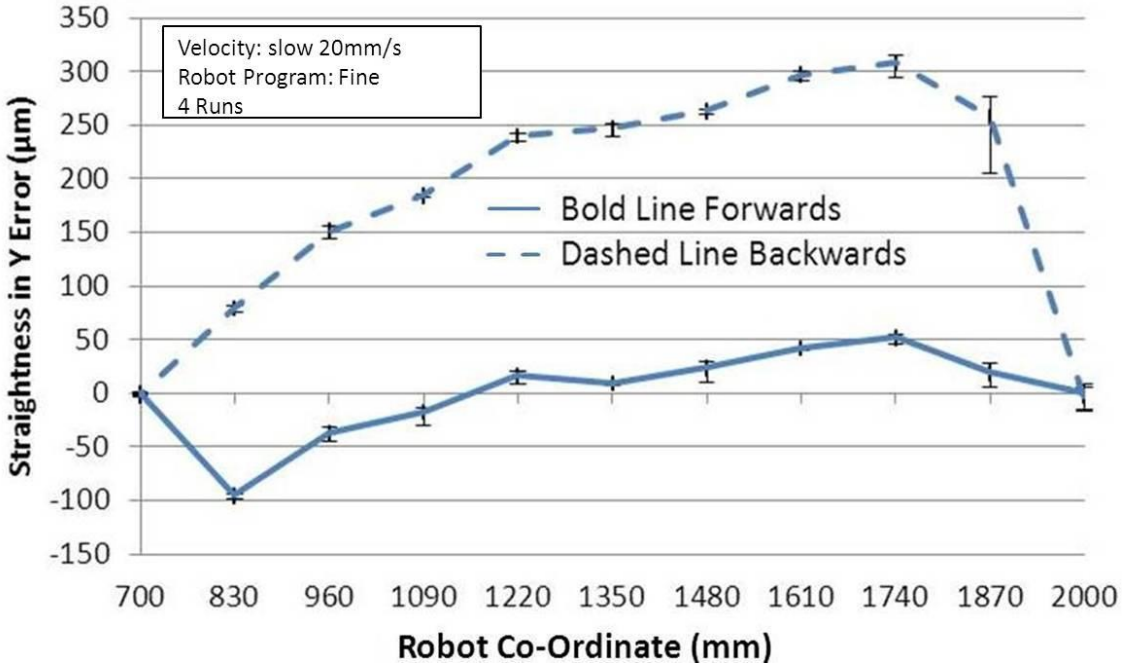


**Figure 73: Linear motion X Axis straightness (Y direction)**

Figure 73, shows the X axis straightness in Y error. The maximum errors are -100µm and 300µm on the forward and reverse motion respectively close to the start and end co-ordinates at 830mm and 1740mm. Hysteresis is significant in the motion and is greatest by up to 250µm at x co-ordinate 1,740mm. Repeatability is good at 25µm (error bars), but on the reverse motion is 75µm at co-ordinate 1,740mm.

Figure 74 shows the straightness in Z error along the X axis. The area of the greatest error is in the central region of the robot motion measuring at 356µm. The repeatability is at worst 70µm and 92µm (error bars) about a quarter of the error magnitude, at the last two co-ordinates respectively.

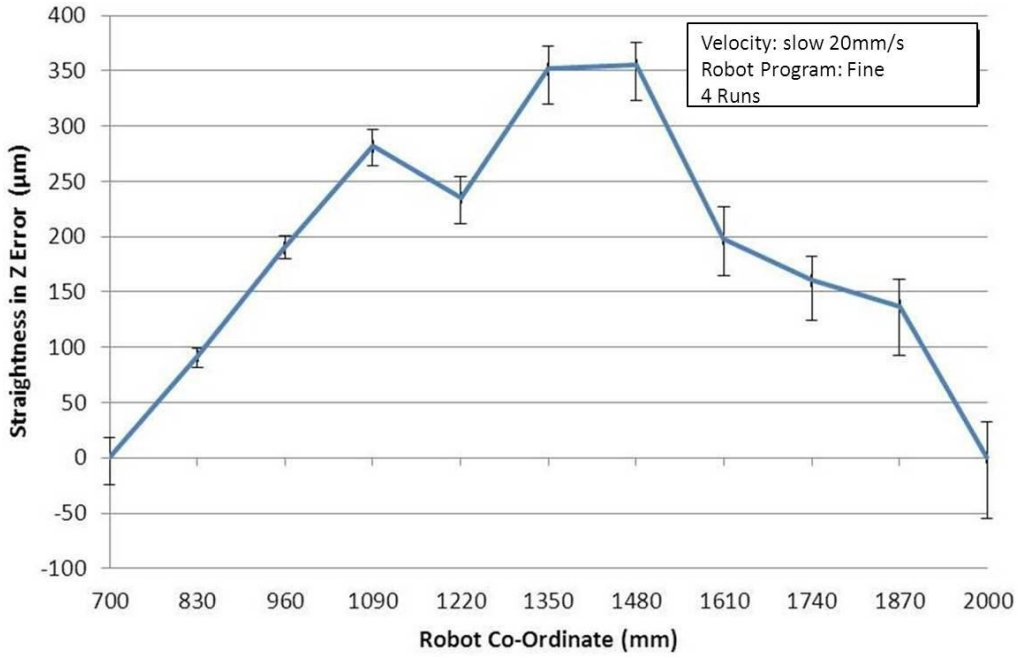


**Figure 74: Linear motion X axis straightness (Z direction)**

### 5.1.2 Y Axis geometric accuracy

The Y axis geometry is the information gathered by the interferometer on how the robot performs in the Y axis when relatively cool. It includes; straightness in the vertical and lateral directions and linear positioning assessments.

Figure 75 shows the linear positioning error in the Y axis; the results show that the error motion is up to 736µm at the end of the robot motion of 2,000mm. The error motion shows that hysteresis accounts for up to a maximum deviation of 327µm at x co-ordinate -230mm. The repeatability along the whole motion is very good at least 30µm (error bars) such that it is minimal compared to the error motion.

Figure 76, shows the straightness in X error along the Y axis. The largest error is up to -153µm at robot co-ordinate -100mm. Hysteresis is more relevant in the first half of the robot co-ordinate system having a deviation of at most 80µm rather than in the latter, where the difference is up to 40µm. From co-ordinates 100mm to 620mm the hysteresis makes the error motion cross over. Repeatability is good at 20µm (error bars).

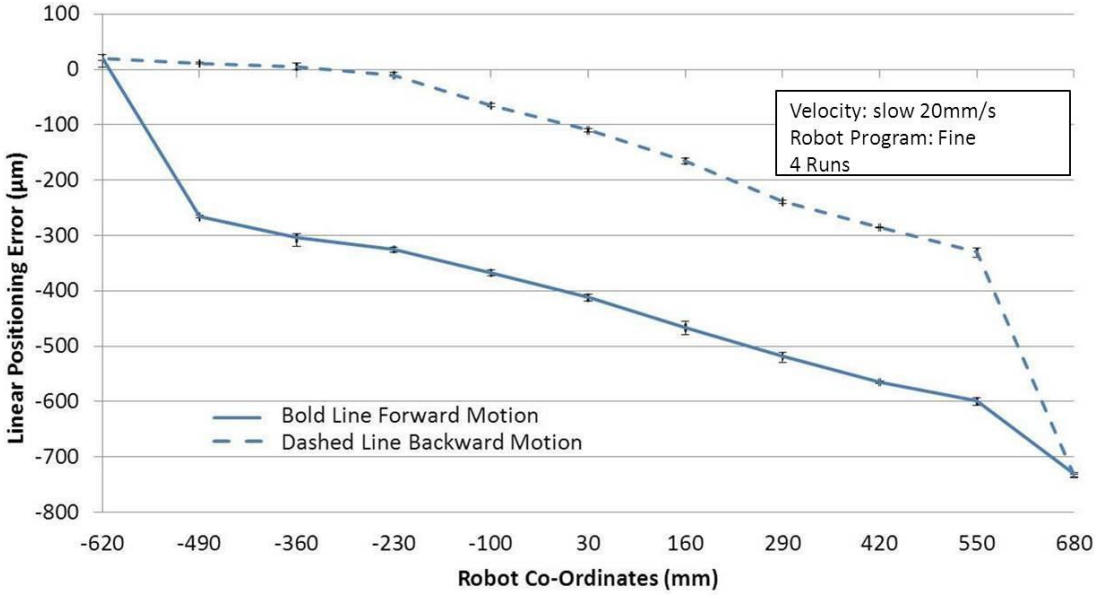


**Figure 75: Y Linear motion positioning (Y direction)**

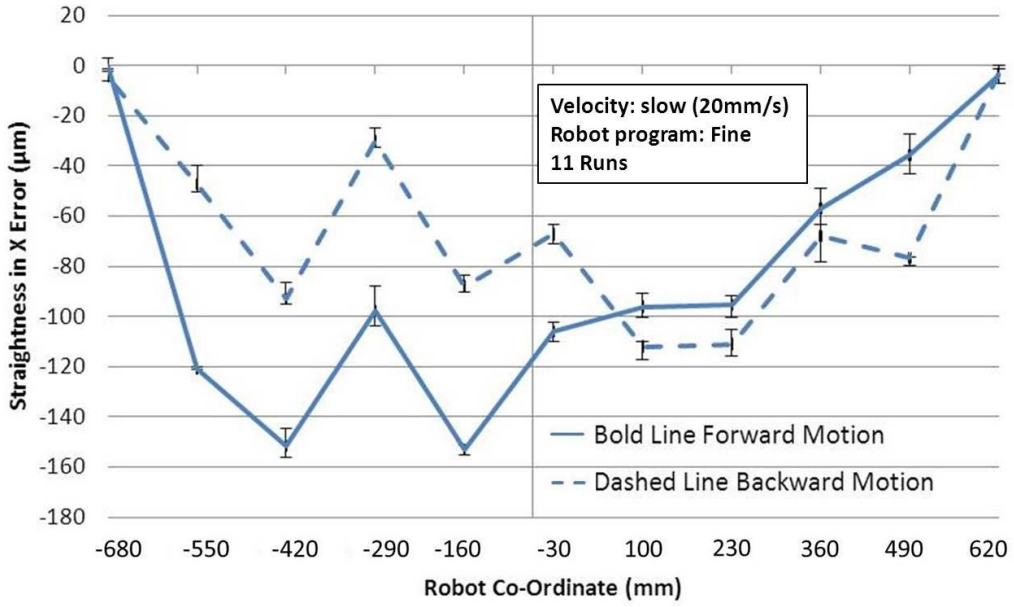


**Figure 76: Linear motion Y axis straightness (X direction)**

Figure 77 shows the straightness in Z error along the Y axis. The results show that the robot is least accurate at 337µm in the centre of its motion at co-ordinate -30mm. The difference caused by hysteresis is greatest by up to 50µm at x co-ordinate -420mm. Hysteresis causes the error motion to cross over by up to 25µm from x co-ordinates 100mm to 620mm. Repeatability is good to a minimum of 17.4µm (error bars).

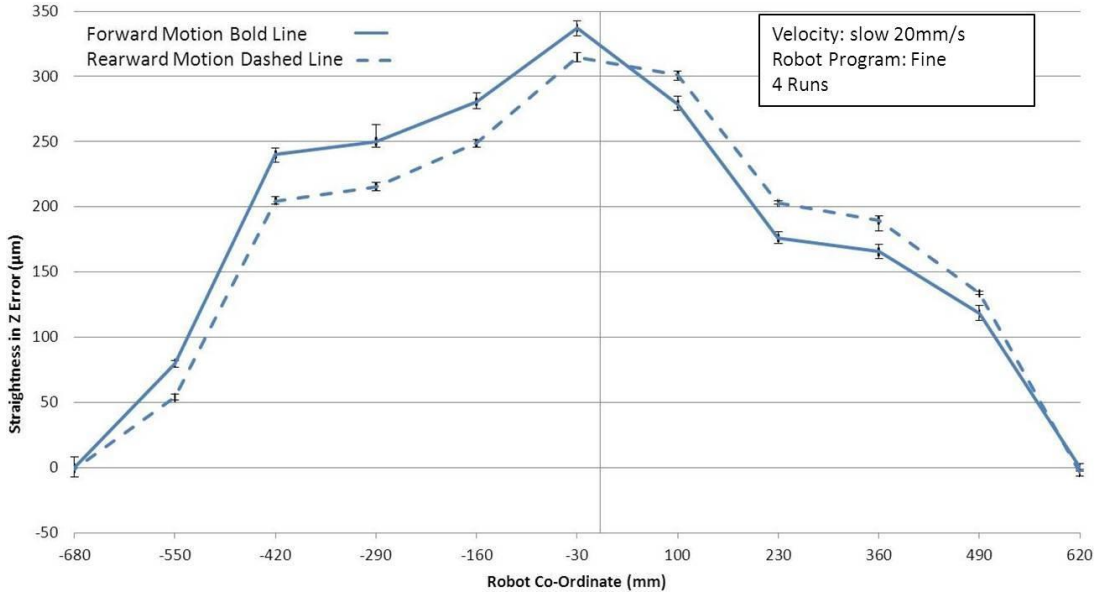


**Figure 77: Linear motion Y axis straightness (Z direction)**

### 5.1.3 Z Axis geometric accuracy

As discussed in the Experimental methodology chapter 3, the robot was moved along the Z axis and its position was assessed for accuracy in three dimensions. The error bars are the upper and lower bounds of the repeatability of the robot.

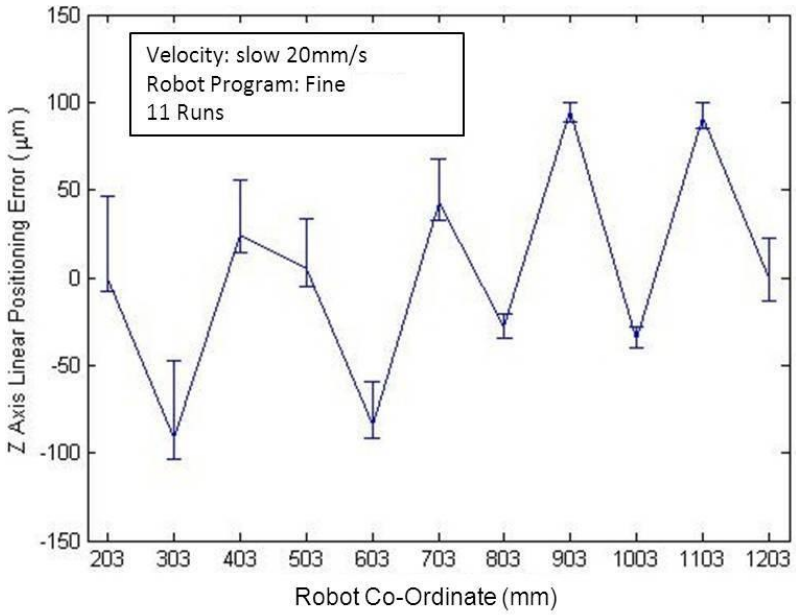


**Figure 78: Z Linear motion linear positioning (Z direction)**

The linear positioning in Z error in Figure 78 of the Z axis has a maximum inaccuracy of ±100µm. The repeatability in the measurements range from 16µm (error bars) to 56µm (error bars).

Figure 79 shows the straightness in Y error of the Z axis. The results show a maximum negative inaccuracy at co-ordinates 603mm of -87µm and positive inaccuracy at 57µm at Z co-ordinate 1003mm. The repeatability ranges from 34µm to 52µm (error bars).

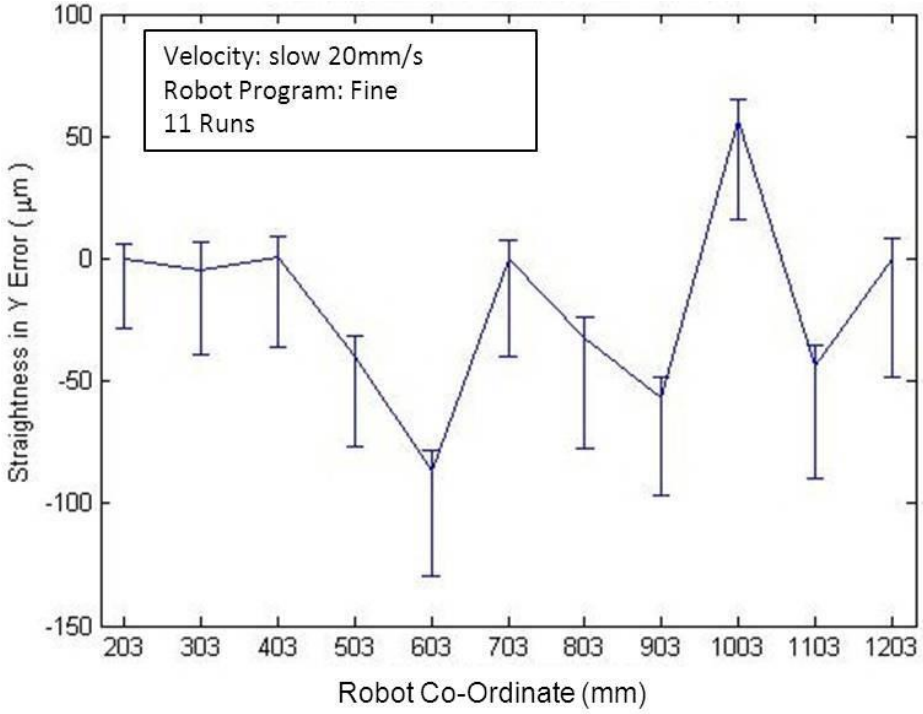


**Figure 79: Z Linear motion straightness (Y direction)**

The straightness in X error is shown in Figure 80. The Z axis has maximum negative inaccuracies of -22µm at co-ordinates 1003mm. The most positive inaccuracy is 31µm at the co-ordinate 403mm. The range in repeatability was from 21µm to 43µm (error bars).

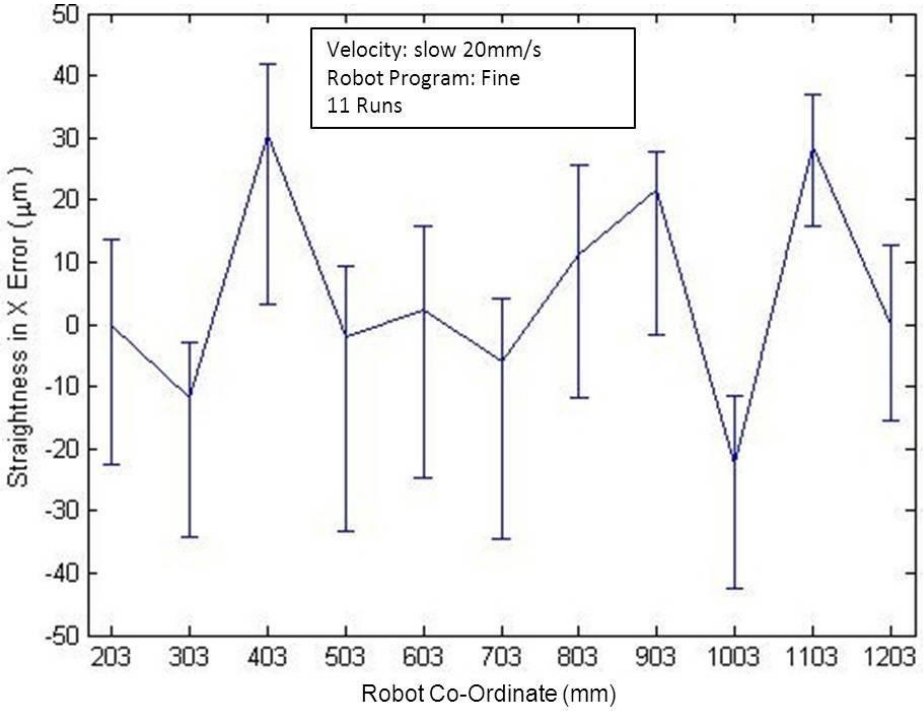


**Figure 80: Z Linear motion straightness (X direction)**

### 5.1.4 Circular motion of robot end effector

There were three single circles of 1.3m diameter moved by the end effector.

The images show that the circles are very closely followed see Figure 81and Figure 82. One of the most extreme areas of the X and Y differences are seen in the view of the circle. It can be seen that the difference between the measured points are at most within 0.5mm of each other. The circles themselves are only testing the repeatability of the robot in a short space of time. The errors in the repeatability of the robot moving in a circle from the initial to the third repetition has shown an error up to a 1.3mm in the repeatability of the motion in y and 1.5mm error in the repeatability of the motion in X. Between the first and second repetition the difference shows that in the first half of the motion of the circle, that repetition one has higher repeatability by approximately 100µm in the X and Y. After half way through the motion, its repeatability equalises and then towards the end becomes worse by 100µm in the X and Y motion.

The images show that there are 166 measured points along the circle from the start of the shape to the end. The repeatability of the robot to those positions (while it was moving at 100mm/s with a fine motion setting) was up to 0.5mm and in the Z up to 0.35mm or 0.15mm to -0.2mm.

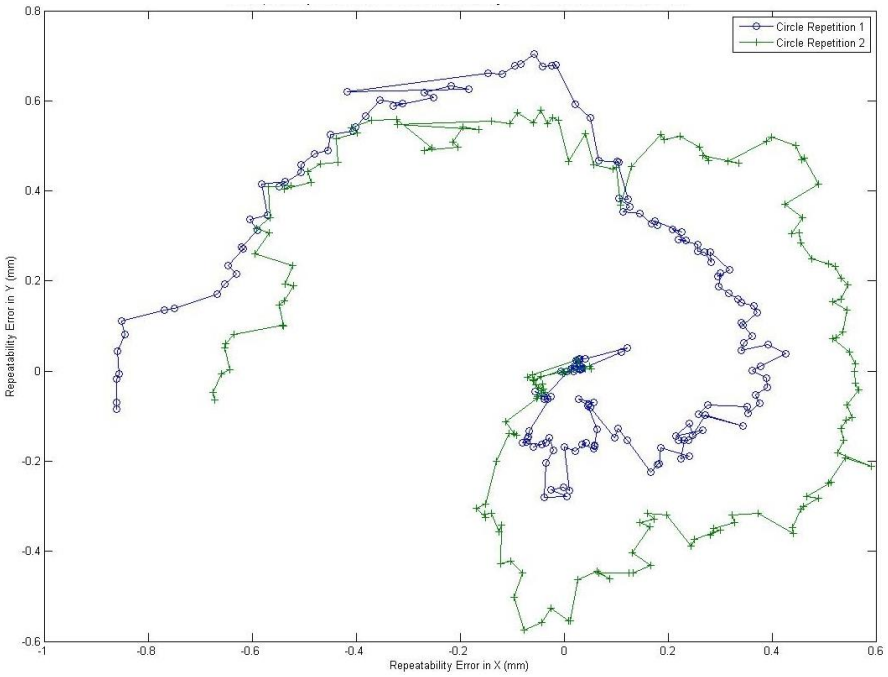


**Figure 81: Repeatability for circular motion X and Y axis**

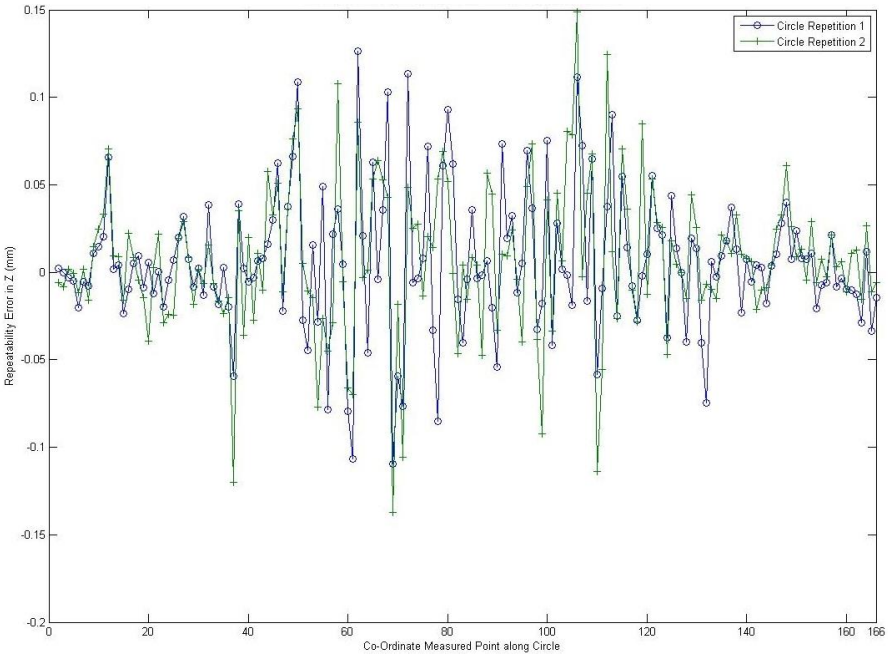


**Figure 82: Repeatability for circular motion Z axis**

### 5.1.5 ISO Standard geometric assessment

As described in the Experimental methodology chapter, in Figure 26 sub-section 3.1.2 ISO standard, the defined robot path was utilised to assess repeatability over five successive runs. The points of measurement for the ISO standard illustrated by points A to C are associated with graphs Figure 83 to Figure 85.

The robot path measured with the laser tracker; see Figure 83, in image A (Figure 83) shows that the motion in the X axis in the corner (A) is repeatable to approximately 70µm and in the Y axis 60µm.

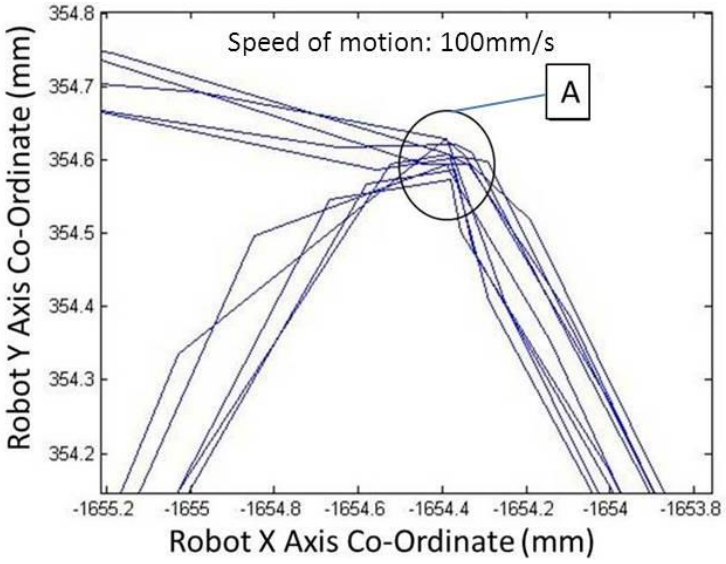


**Figure 83: ISO Corner motion repeatability**

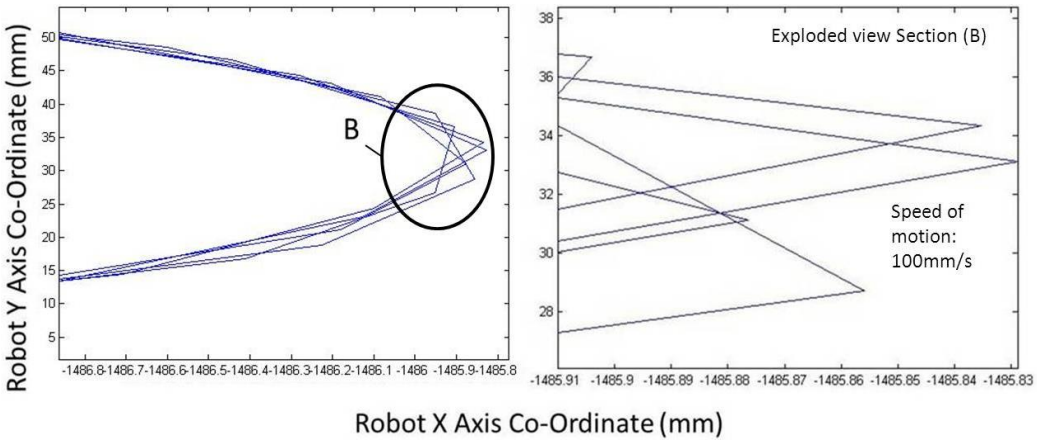


**Figure 84: ISO Circular motion repeatability**

For the large circular motion of the ISO path (Figure 84), assessment of the right edge motion shows repeatable to 70µm in the X axis.

Figure 85 shows the closing performance circular loop motion. The exploded view of C shows the repeatability for the X axis in the region of 75µm.

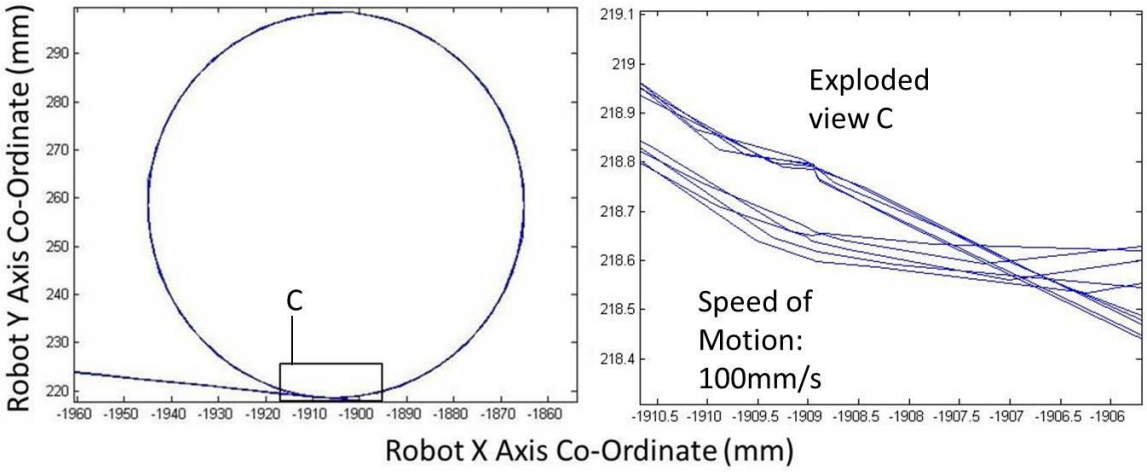


**Figure 85: ISO Path small circle loop**

Next the result for the robot overshoot tests for the three co-ordinate axes x, y, z are presented. These were carried out dynamically with an axis velocity of 100mm/s.

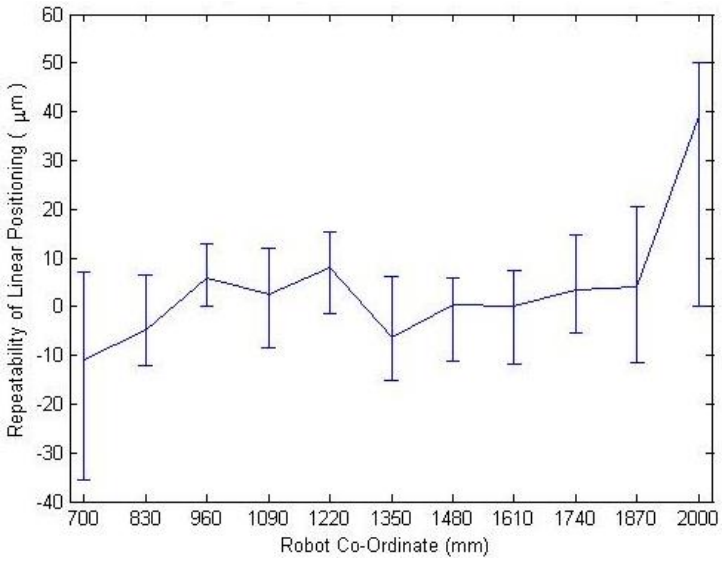


**Figure 86: Repeatability linear motion (X Direction)**

The repeatability for linear motion in the Y axis (Figure 87) is just over 70µm.

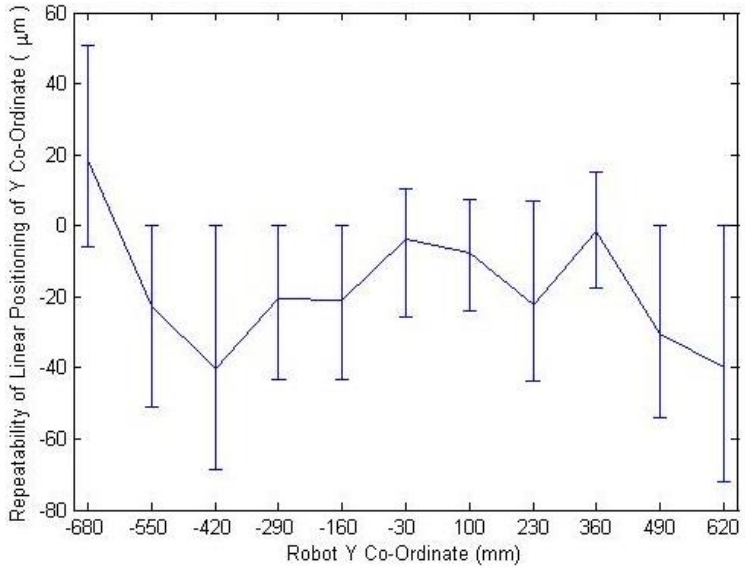


**Figure 87: Repeatability linear motion (Y direction)**

The repeatability of the Z axis linear positioning is a 60µm in Figure 88

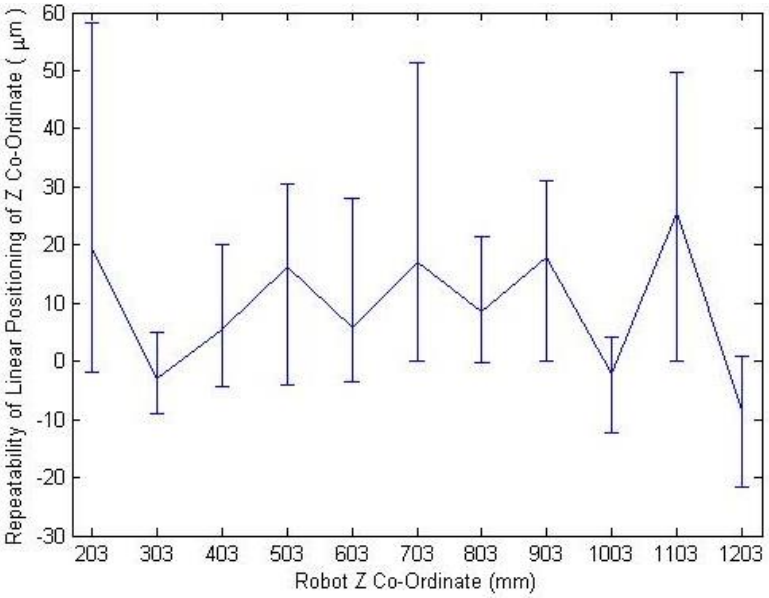


**Figure 88: Repeatability linear motion (Z direction)**

## 5.2 A Thermal mapping system

An image of the robot's thermal distribution was acquired via a thermal imaging camera. The key thermal areas were identified for implementation of the thermal measurement system. Thermal profiles were used as an input for the thermal modelling.

The cool thermal image of the robot is displayed in Figure 89. This was taken prior to any robot motion at ambient temperature. It was noted that the joint surface for the end effector (image F) of the robot was slightly reflective and so thermal data taken from this region was affected.

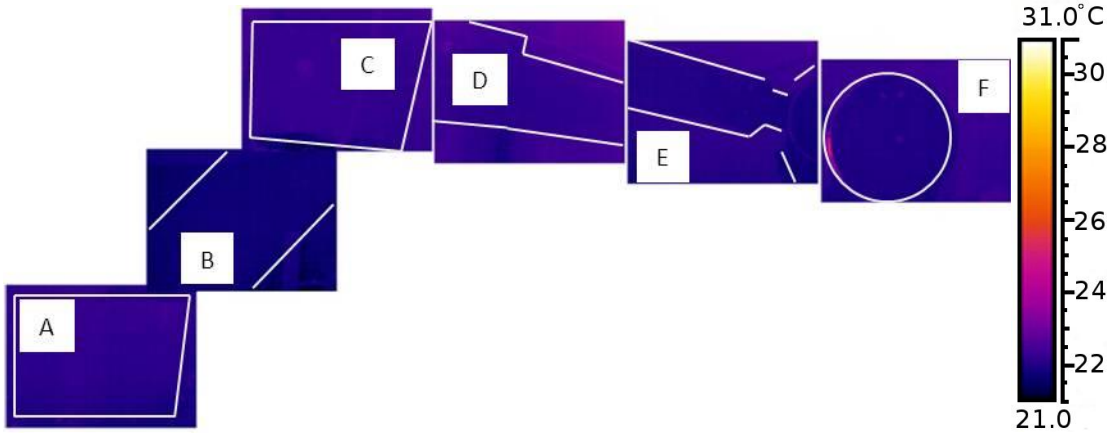


**Figure 89: Robot thermal image at ambient**

The highest workloads were for the middle and base joints. These joints have motors driving the robot arm through gearboxes in each joint. Investigation established that the end effector produced minimal heat at the gearbox for this joint. This implies that the majority of the heat travelling along the two robot links originated from the motor regions.

Figure 90 shows the shows the thermal progression over a run of seven spiral sets at 100mm/s. The first spiral set (image i), confirmed that the heat from the robot is generated mainly in the second joint of the base (position a) responsible for the vertical motion and the middle joint for the spherical wrist. There were two motors located in the base, each rated at 4.3KW power. These control the motion in the horizontal plane of the robot and vertical direction of the first link. The middle joint in the robot contains the rest of the motors as indicated in the Experimental methodology sub-section 3.2.1, Figure 29.

The third spiral set (image iii position b) indicate that the coldest part of the first robot link is at the right and continues along almost three quarters along its length. The end effector joint in (position f) is still approximately at ambient temperature. The heat increased from the middle joint of the robot (position c)

and along the surface of the base of the robot (position a) where the second base joint is.

The fourth spiral set image (iv) shows that the heat intensity originates from the vertical motor in the base of the robot (position a) and is increasing further in the middle robot joint (position c). The robot arm shows that heat is being conducted along its length, and that the bottom of the base joint (position a) is increasing in temperature.

The robot clearly heats up above ambient temperature during the spiral motion. When comparing the hottest images of spiral set seven (image vii, positions a and c), with the images of the robot at ambient (Figure 89), we can see that the base (position a) and middle section (position c) of the robot responsible for the vertical motion, heat up the most. This is because those parts (positions a and c) of spiral set seven (image vii) of the robot have the highest loads for this type of motion. The first link (position b), shows heat only near each joint, while the centre remains cooler. The joint in the middle of the arm (position c) heated up by 10 degrees over ambient and this heat was partially transferred to the two connecting links (position b, and positions d to e). The larger link on the left (positions d to e) conducted heat at a slower rate due to its greater thermal inertia, whereas the heat flowed faster into the smaller link (position b).

The first key thermal point on the robot is in the right hand corner of the base (position a). This contains the motor responsible for the vertical motion of the entire robot arm. Next the lower section of the base (position a) shows the heat produced from the motor controlling the lateral motion of the robot. The middle joint (position c) controlling the second link (positions d and e) of the robot is also significant, containing the remaining four motors responsible for the rest of the robot arm’s second section and orientation of the end effector. Due to concentrated heated areas along the arms and this joint, these will be considered as the key thermal points. The temperature profile from the key points along the links (positions b, d and e) provide data of the thermal distribution along them, as a result of the heat generated through the motors.

This will provide an increased understanding for thermal modelling in combination with the thermal profile results from the following section.

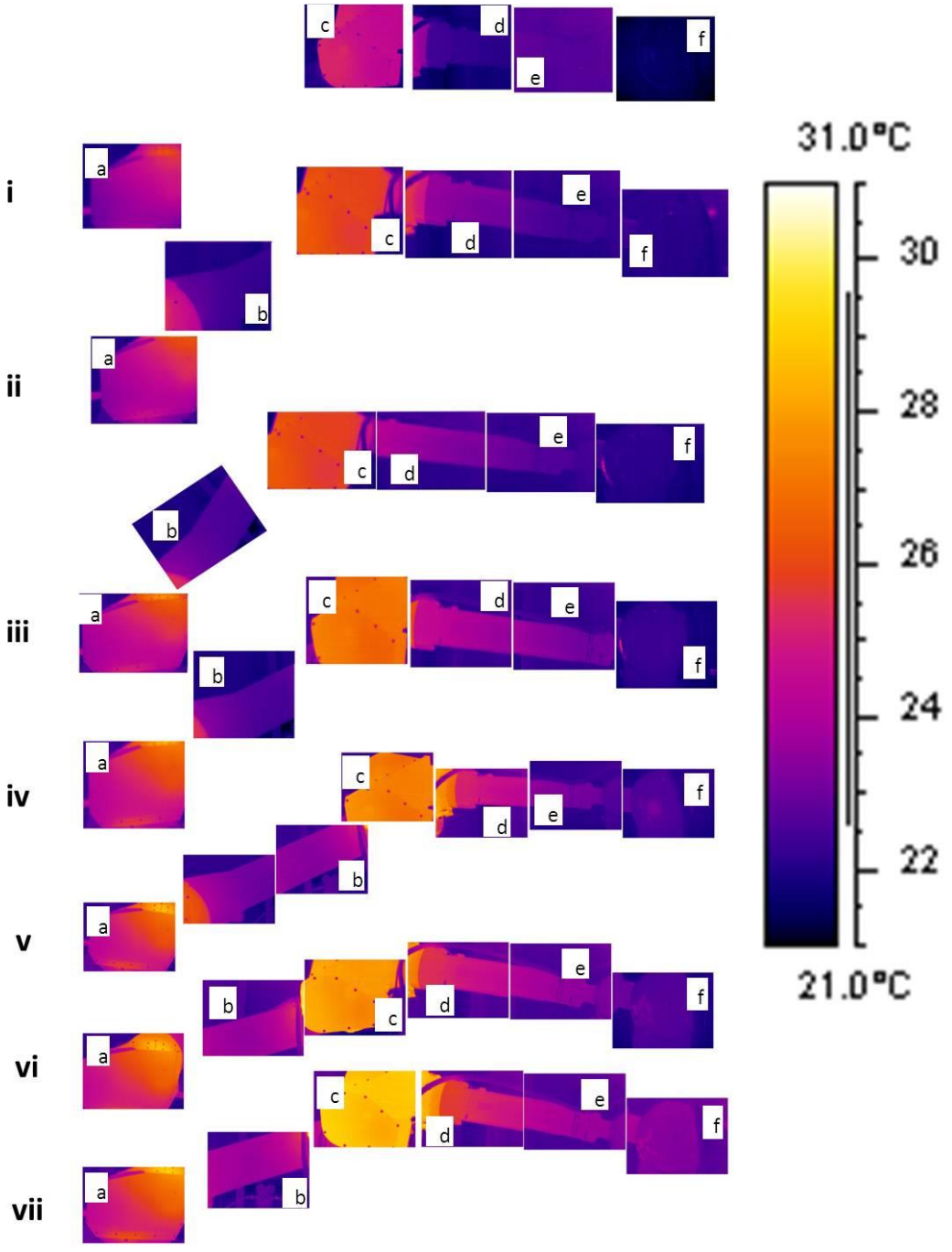


**Figure 90: Thermal image of robot after spiral sets i-vii**

### 5.2.1 Thermal profiling mapping: Thermal gradients for modelling

Temperature gradients across the surface of the base section, and the robot arm connected to it, are made in order to make a thermal model from the right hand corner of this image to the end of the arm connected to it. This will help to build a thermal model in order to predict the thermal effects on the robot's end effector.

In Figure 91, the temperature near the joint in image H shows an increase up to almost 26.5°C, with the rest of the structure increased above the 22.5°C background temperature. Subsequent images show that the heat gradually increases and that the movement of temperature across the base originates predominantly from the first link motor and the base.

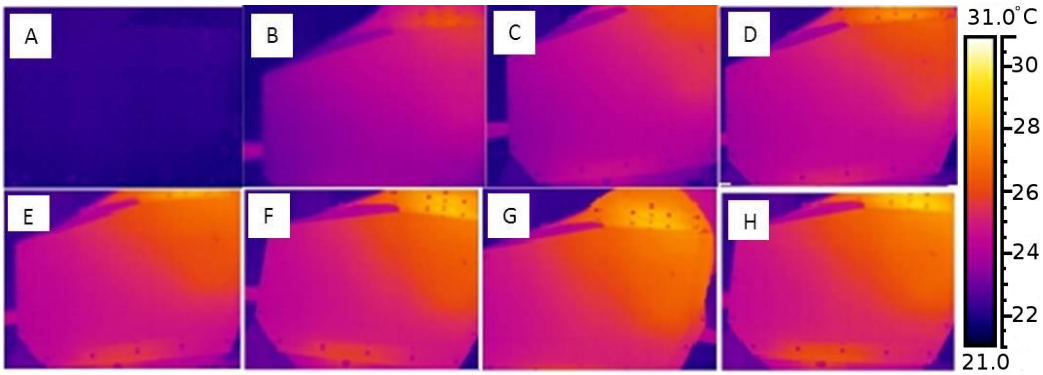


**Figure 91: Thermal image of robot base heating up with spiral motion**

The base section of the robot was thermally profiled (Figure 92). The thermal image shows that before the robot has been worked, this part is at ambient temperature with no thermal gradients across the surface. The robot did not undergo any movement and hence there was no reason for its temperature to be elevated. The profile has not been smoothed and therefore the profile has a level of noise.

The thermal image in Figure 93 image A shows the thermal gradient after the robot has been 'worked'. The lines show where the thermal profile has been analysed, plots are shown in the lower image B. Image A shows the thermal image of the base which contains joints one and two. The profiles are shown in

image B. The first half of the data and base image shows that the bottom of the robot and the top right half has a raised temperature, the rest is cooler. The bottom part contains the motor responsible for yaw of the robot arm. The dip and bumps are observed due to discontinuities in the view structure which result in their surfaces to appear to be different temperatures.

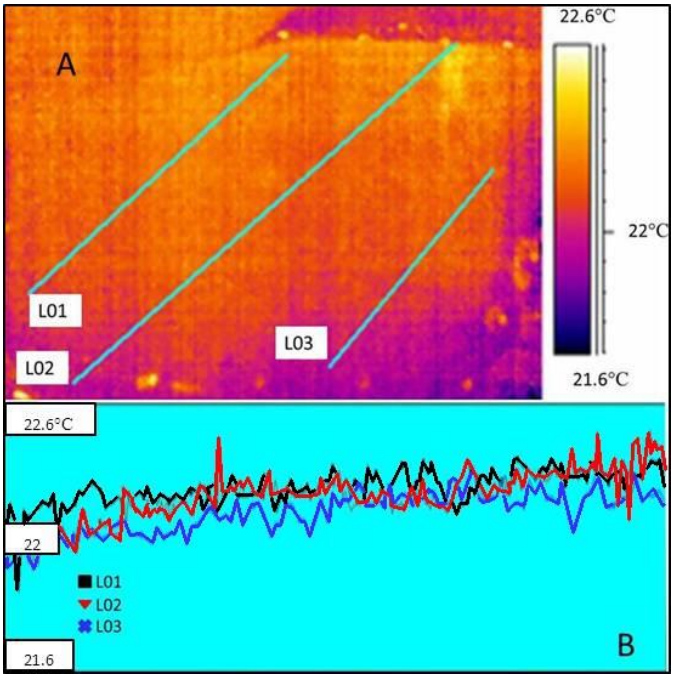


**Figure 92: Thermal gradient across base (no work)**

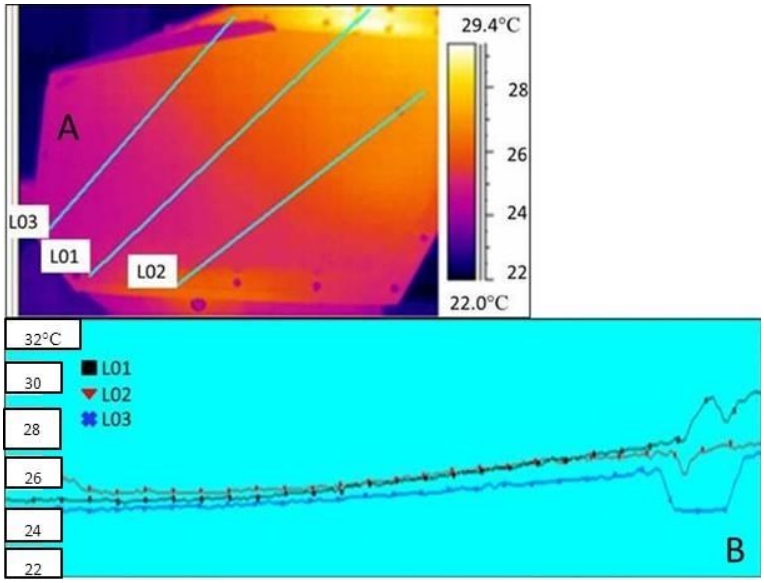


**Figure 93: Thermal gradient across base 'worked' state**

It can be seen that the top right part of the robot base is hottest at 29°C. This part contains the motor responsible for pitch of the robot arm. The top right corner of this image will be used for modelling the beginning of the first link.

The first link of the robot connects the base to the middle section of the robot. This provides vertical motion so that the robot can move the end effector. Along this link the temperature profile will be used to model to produce the thermal distribution.

The image shown in Figure 94 illustrates how the motor housed in the base of the robot, (that controls the part of the vertical motion and the joint in the middle of the link) causes a thermal gradient to pass through the link. The scale in the picture ranges from 21°C to 31°C. The hottest part in this section is where the base joins link one. Temperatures are seen to reach up to 24°C to 30°C.

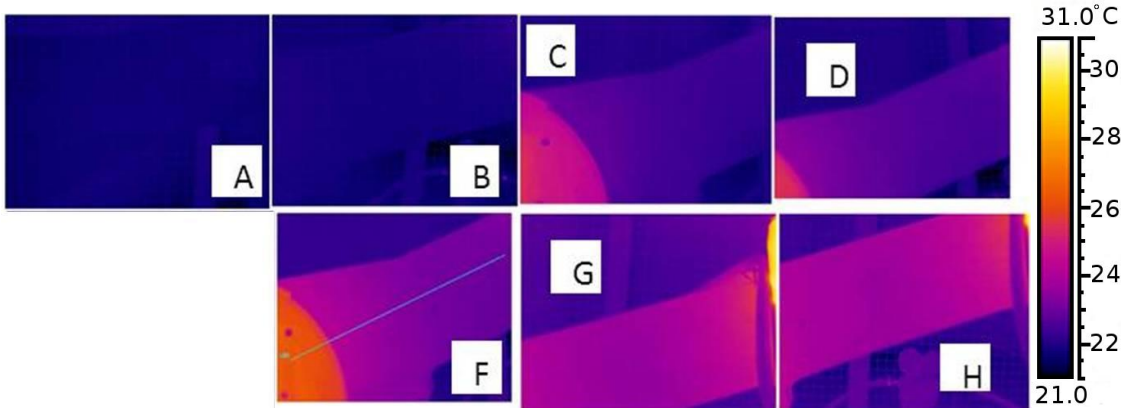


**Figure 94: Thermal effect on link1**

As the temperature of the first link rises it can be seen that this conducts into the first part of the arm, Figure 94 image C. The coolest point of the link is at the three quarters point along its length. In the hottest image, Figure 94 image H, the coolest part of the robot is above ambient temperature by about a 1.5°C. The middle joint of the robot arm (at the opposite end of link 1) is also seen to inject heat into the upper half of the first link`, see images G and H.

As shown in Figure 95 with the robot in the ‘cool’ state, the temperature is relatively at 21.5°C.

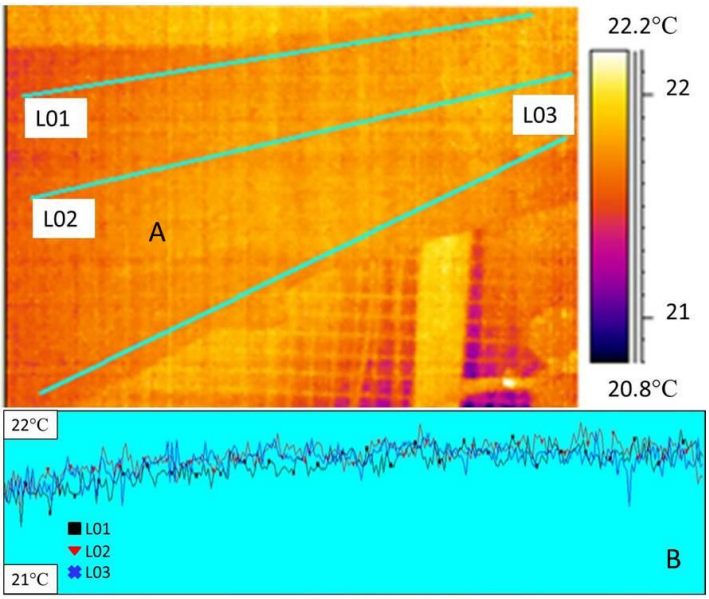


**Figure 95: Thermal gradient for link 1 in 'cool' state**

Figure 96 shows link 1 in the 'worked' state. The lower edge of the link is at 23°C while the hottest part of the link is at 26.6°C. The whole of the joint at the base of the arm is at 26°C. The gradient from the hot part of the link to the cooler section is 2°C. The reason for the rapid change in temperature is the joint structure.

The difference in the thermal profile was for the 'cool' state 20.8°C to 22.2 °C and for 'worked' state 22.2°C to 30°C.

These parts of the joints and link will be modelled as an exponential decay from the peak temperature of this joint, to the coolest part of the link as well as an exponential rise to the middle joint from the place where it begins to heat up. The thermal profile shows this in Figure 96 and Figure 97.

The middle joint of the robot was monitored; this contains four smaller motors responsible for all the motion of the second and third link. One motor at 2.5KW and another at 1KW power capability. The 2.5KW motor is responsible for the vertical motion of the joint which lifts or lowers the second link of the robot. The next motor is for the roll of the second link. The other 1KW motor is to lift or lower the wrist while the last 0.75KW motor is to roll the wrist. The motors responsible for keeping the orientation of the end effector constant, work less

and are smaller than the motors responsible for the end effector position, therefore generating less heat.

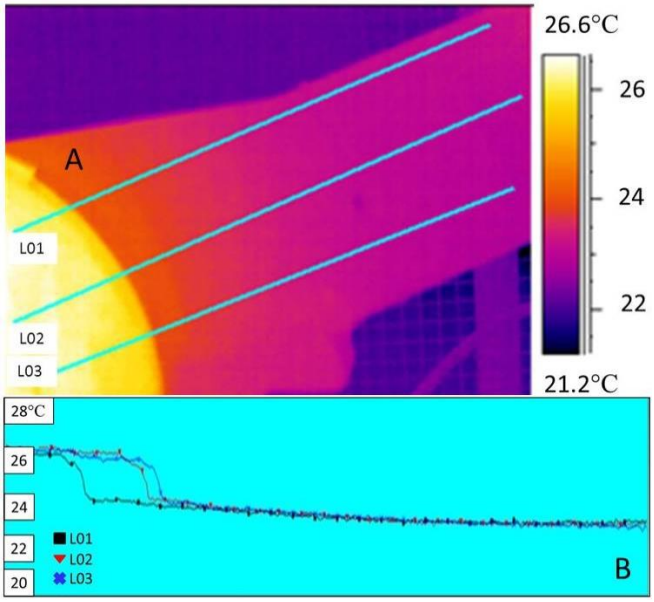


**Figure 96: Thermal gradient for first half of link 1 in 'worked' state**

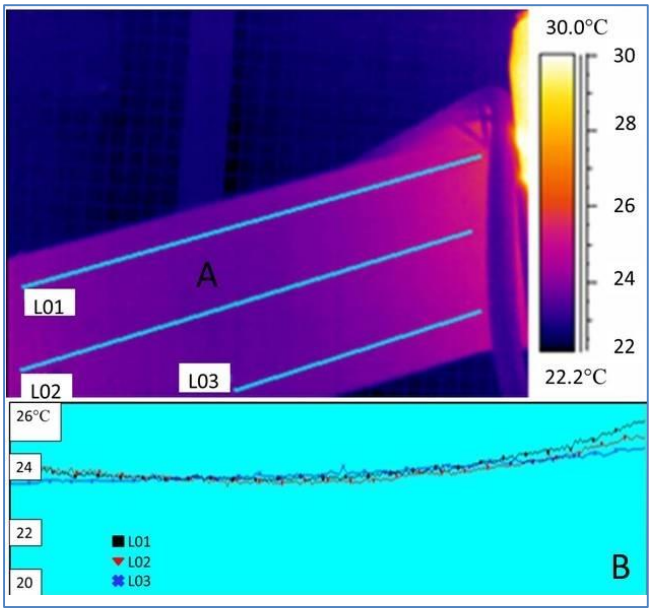


**Figure 97: Thermal gradient for second half of link 1 in 'worked' state**

Figure 98 shows the thermal progression during working. The robot starts at room temperature of 22.2°C, and the joint heats up to a minimum of 28°C whilst

the upper part at 29°C. The screws on the robot plate are shown to be cooler due to being a different colour.

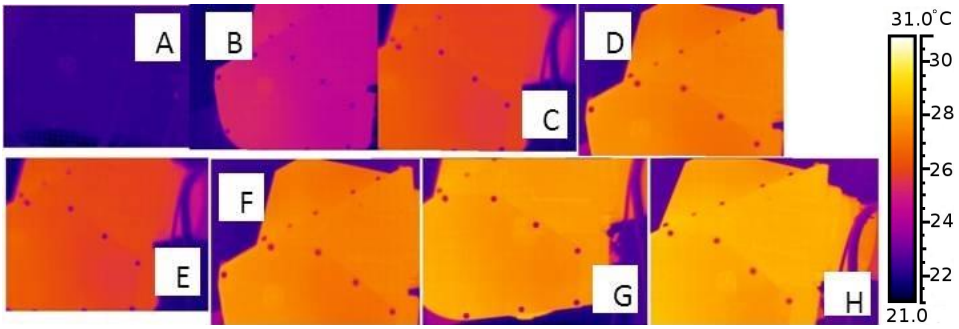


**Figure 98: Thermal images of middle joint heating up**

The thermal gradients in the 'cool' state across this part of the robot (shown in Figure 99) are uniform within 1°C. In the 'worked' state, the hotter areas (see Figure 100 image B) are at the edges and the upper half of the robot motor. This can be explained by the position of the different motors conduction. As the total temperature variation is still small, for modelling the temperature on the length of a link, a single point temperature is adequate.

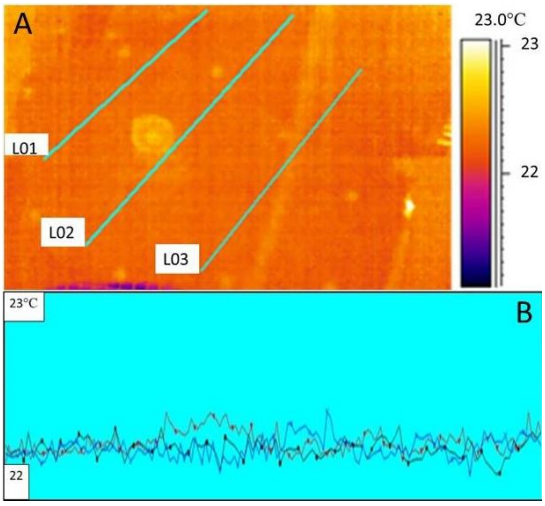


**Figure 99: Thermal gradient for middle joint 'cool' state**

This part of the robot arm contains the motors responsible for pitching and rolling the second link, and yawing and pitching the end effector. The heat responsible for the thermal image originate from the 2.5KW motor, involved in lifting and lowering the second link and the 1KW motor in keeping the end effector pitch orientation constant. The two remaining motors during the

required spiral motion responsible for rolling the second link (1KW) and yawing the end effector (0.75KW) produce minimal heat.

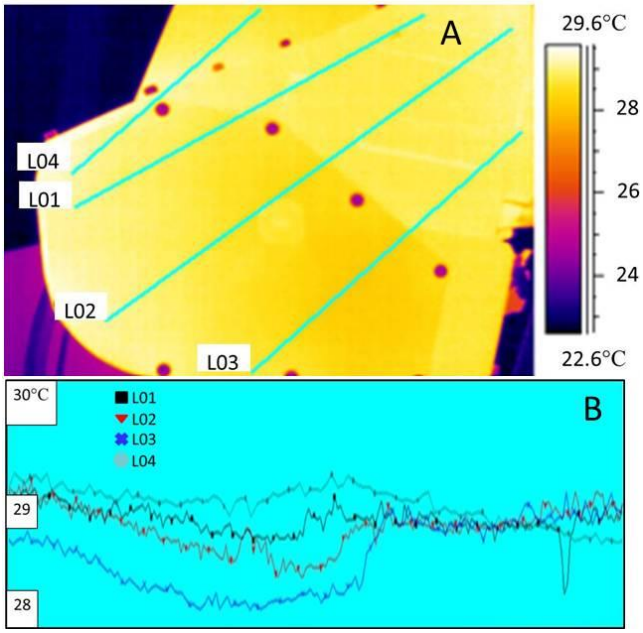


**Figure 100: Thermal gradient for middle joint in 'worked' state**

Figure 101 (image A to H) shows the first half of the second link of the arm. Initially at ambient temperature, the second link end of the heats up the quickest due to the heat from the middle joint of the arm. Conduction of this heat shown by image B to H from the left hand side to the right occurs at a slower pace.

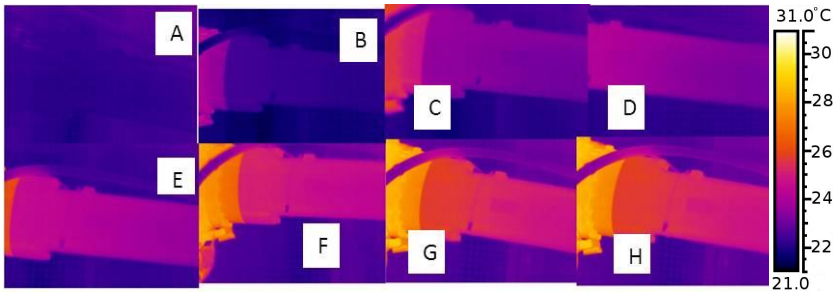


**Figure 101: Thermal images of first half of link 2**

Figure 102 shows the thermal gradient for the first half of the second link in the 'cool' state.

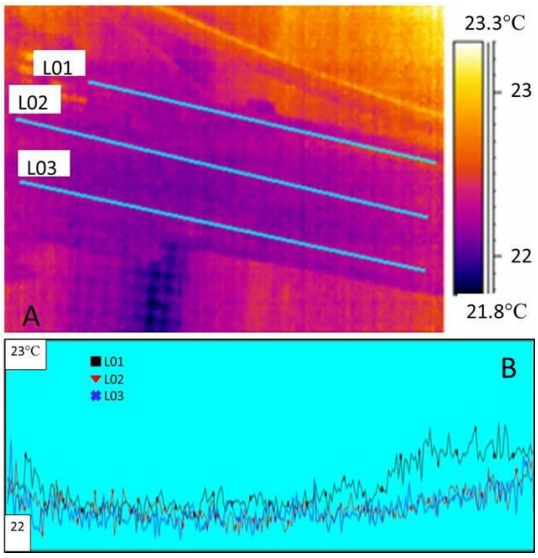


**Figure 102: Thermal gradient for first half of link two ‘cool’ state**

The image of the link when ‘worked’ is shown in Figure 103. It shows that the link has a gradual decline in temperature from the edge to the mid-section. The hottest section is at the connection to the middle joint. Following that, there is a sharp temperature drop from 29°C to 26°C. This is due to the joint structure, as well as different emmisivities that potentially contribute to this change. The gradient along the link after the sharp temperature drop is a decrease in one degree.

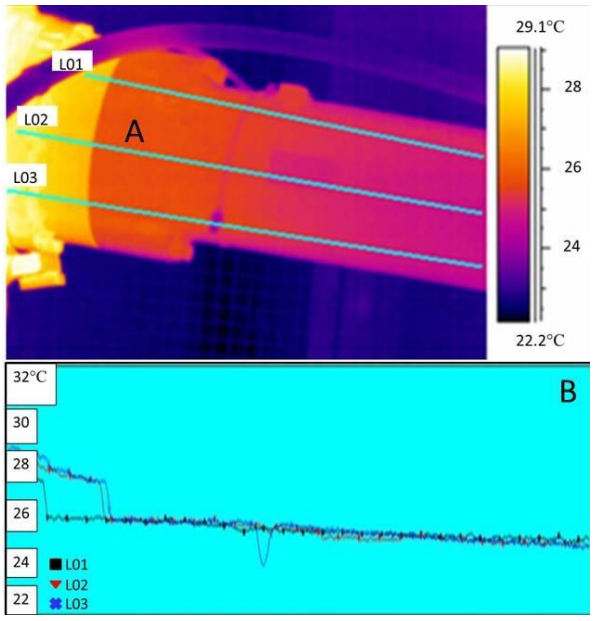


**Figure 103: Thermal gradient of first half of link two ‘worked’ state**

The second half of the second robot link was thermally imaged in order to complete the temperature profile of the second link for the robot model. This part is responsible for producing the roll of the second link of the robot driven by the 1KW motor in the middle section of the robot arm. The images A to H in Figure 104, show that the main source of heat comes from the motor responsible for the vertical motion in the middle joint.

The temperature differences shown are due to the surface colour and emissivity which is different to the painted surface of the robot. There is clearly a slight temperature difference of a degree across the link. The temperature gradient is very shallow at 1°C across this part of the arm. The hottest part of the arm is 24.5°C closest to the middle joint and the coolest point on this part of the analysed arm is 23.5°C. In image B heat is only just seeping on the edges of the arm. It is only after image C that the temperature of the arm is affected above ambient and grows more intense as time goes on.

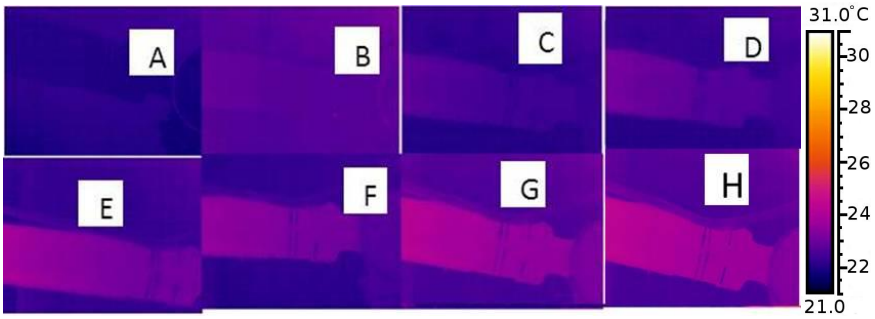


**Figure 104: Thermal images of second half of link two**

Figure 105 shows the second half of the second link of the arm when cold. The shiny surfaces of the cable ties are giving the peaks in the thermal profile at 22.5°C. The robot is at an ambient temperature is 22°C.

The thermal gradient along the second link can be modelled as an exponential decay based on the thermal profile in image B of Figure 103 and Figure 106. In this image there is a negative gradient of roughly a degree from the beginning of the image to the end effector joint.

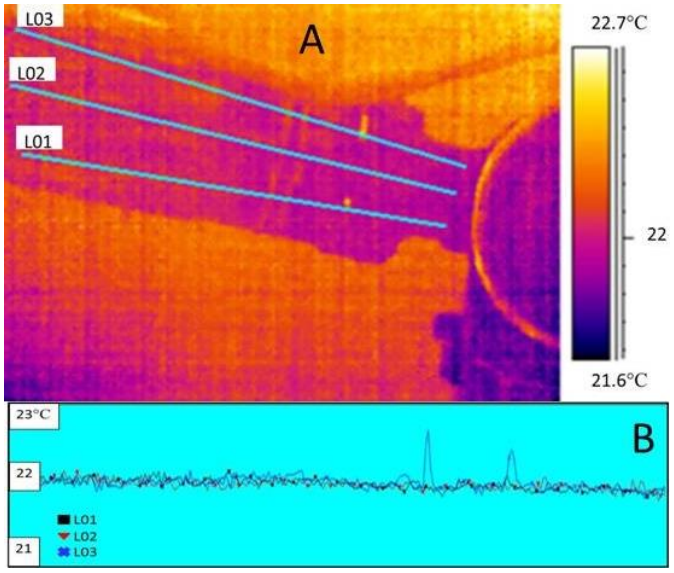


**Figure 105: Thermal gradient for second half of link two ‘cool’ state**

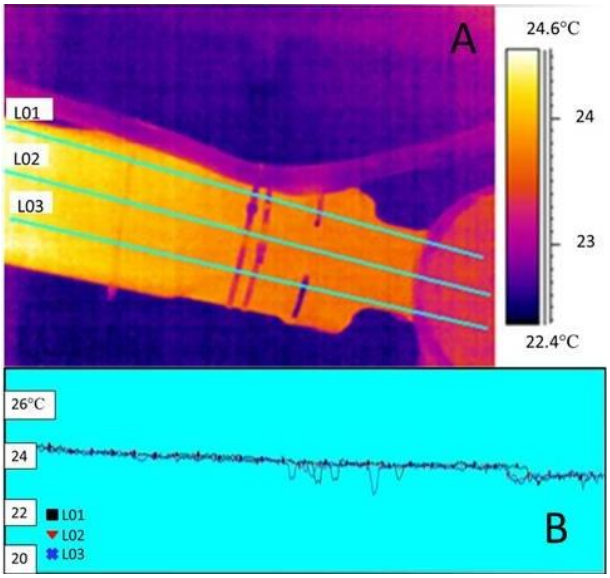


**Figure 106: Thermal gradient for second half of link two ’worked’ state**

This section of the thermal mapping assesses the last link for the robot model as well as measuring how the temperature changes from the edge of the robot’s second link to the last link’s joint.

The images in Figure 107 show how the temperature of joints five and six are the same as the ambient temperature, heating just slightly above ambient by images E to H.

The thermal gradient on the last robot joint when cold is shown in Figure 108 and is constant. Figure 109 shows that the joint temperature goes above the ambient temperature by approximately one degree. When the robot is hot, the link section just before the motor is 0.66°C above the joint face. The robot link is the hottest and the robot joint face is cooler. Only some parts show peaks which are illuminated by the infrared reflections of the thermal imager. These thermal profiles show little change across the face of the joint. There is a mild temperature gradient from the lowest part of the link to the top by about 0.2 degrees but this change is too small to show any significance.

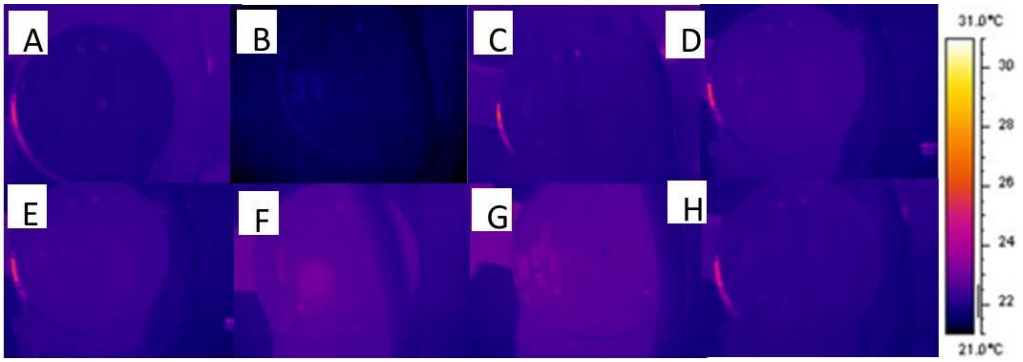


**Figure 107: Thermal images of robot's sixth joint heating up**

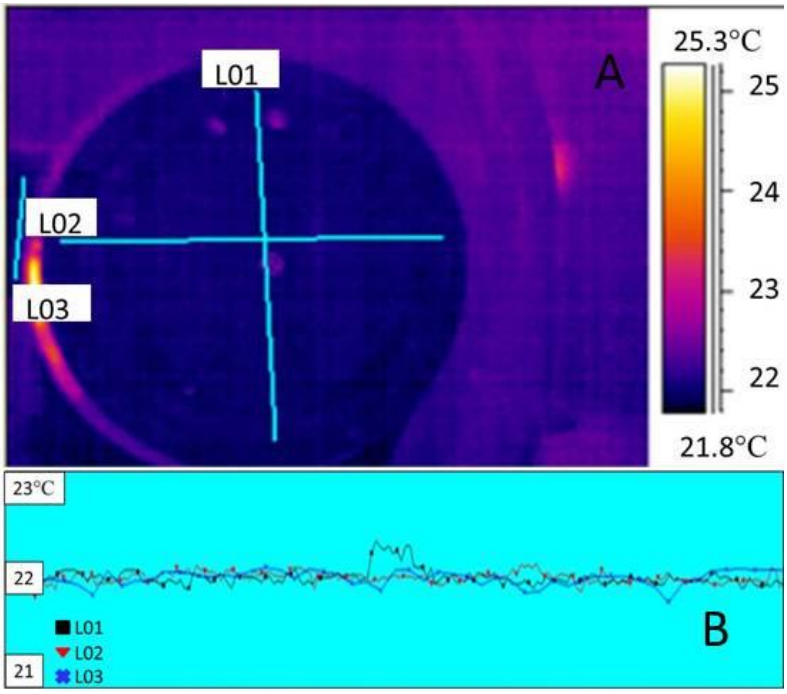


**Figure 108: Thermal gradient for third joint 'cool' state**

The thermal model will show that there is a linear temperature difference between the edge of the link and the robot link.

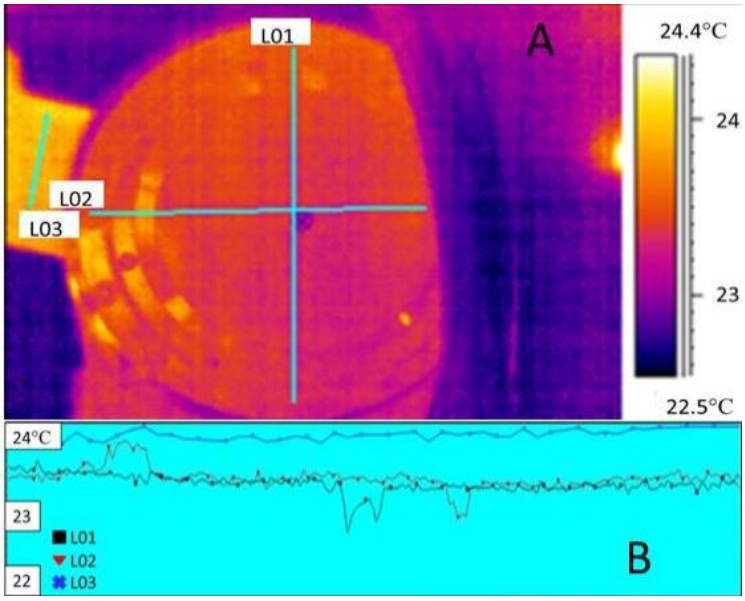


**Figure 109: Thermal gradient for third joint 'worked' state**

## 5.3 Thermal performance

Thermal performance of the robot in the X and Y axes were measured using thermocouples in conjunction with a laser interferometer. The thermal performance was measured for slow linear, fast circular and spiral motions. For the Z axis a laser tracker was used to provide the geometric data due to greater versatility with alignments. Results are presented.

### 5.3.1 Geometrical measurement

The robot's thermal influence on the linear positioning ability in the X Y and Z axes was assessed before and after thermal input was applied by exerting the robot in a fast circular motion repeatedly.

Tests were carried out over a period of 6.5 hours including the linear positioning measurements. The robot circular motion was set at 200mm/s. During the linear positioning measurement the robot velocity was restricted to 20mm/s to minimise induced heat. During the thermal input cycle Figure 110 shows the

temperature variation of the seven channels, see (Figure 48 for positions) over the test period. It can be seen that the lower speed activity, induced greatly reduced levels of heat when compared to the higher velocity. The results show the robot temperature increased by over 12°C at the hottest part. The lip on top of the peak in channel eight and the straight line are caused by the time lag in the robot. Each robot part cool slightly differently while other parts are heated slightly more. The robot peaks slightly after it has been turned off. This is due the internal temperature taking time to reach the surface of the part being monitored.

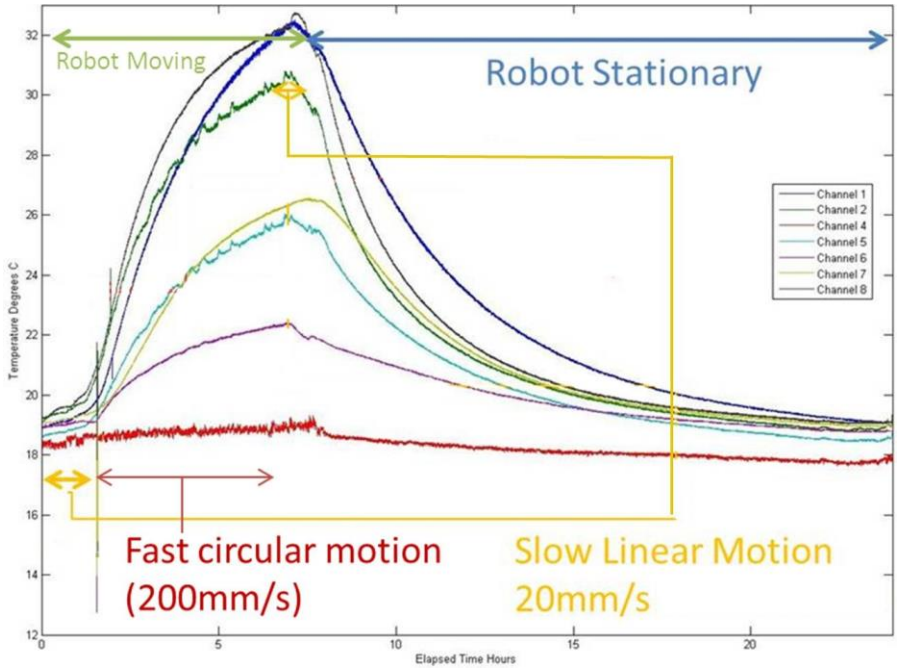


**Figure 110: Thermal response of robot for X linear positioning**

(Channel seven: Robot Part two mid-section of the base controlling lateral arm motion) shows a later temperature peak. This is due to the time it takes for the heat to conduct to the base and side motors. However, cooling is approximately the same due to the large surface area available. This channel did not show any differences during calibration, hence the effect was validated.

Channel one: (Robot Part three joint controlling vertical motion of first link) shows that it has a longer time constant than the others. This is due to the robot section being thicker at this point.

Figure 110 shows (Channels: Robot Part) (one: three; the surface of the joint controlling the first link of the robot arm), (two: one; top right corner of base section), (four: Ambient), (five: two; centre bottom of base section of robot with lateral control of robot arm), (six: eleven; the side of the joint controlling the third link to the end effector), (seven: eight; close to the beginning of link two near the mid-section of the arm), (eight: six; middle joint controlling the rest of the motions of the end effector from vertical motions, in link two and three and its orientation), that all of the thermocouples match the handheld thermocouple to less than a degree.

Using Equation 11, the thermal constant of the robot can be calculated. Considering it takes the whole robot roughly 16 hours to return to background temperature and when hot, the robot is 32°C at time zero and 18°C at time t = 16 hours. K is approximately -2.7°C / hour.

**Equation 11: Thermal constant using Newton's law of cooling**

$$\boldsymbol{k = \frac{ln\left(\frac{y_t}{y_0}\right)}{t}}$$

*Where:*

*k = thermal time constant °C / unit time*

*$y_t$= temperature after time t*

*$y_0$= Initial temperature*

*t = time period of cooling*

The temperature profile at the end of six and a half hours of motion is shown in Figure 111. It shows a thermal change of 14 degrees in the hottest section of the robot. The whole robot is at least four degrees hotter compared to when it began operating after 6.5 hours. The hottest part in this figure is 16°C above the temperature of the robot when cool. This type of temperature profile is typical of most other motions that the robot undergoes for long periods of time.

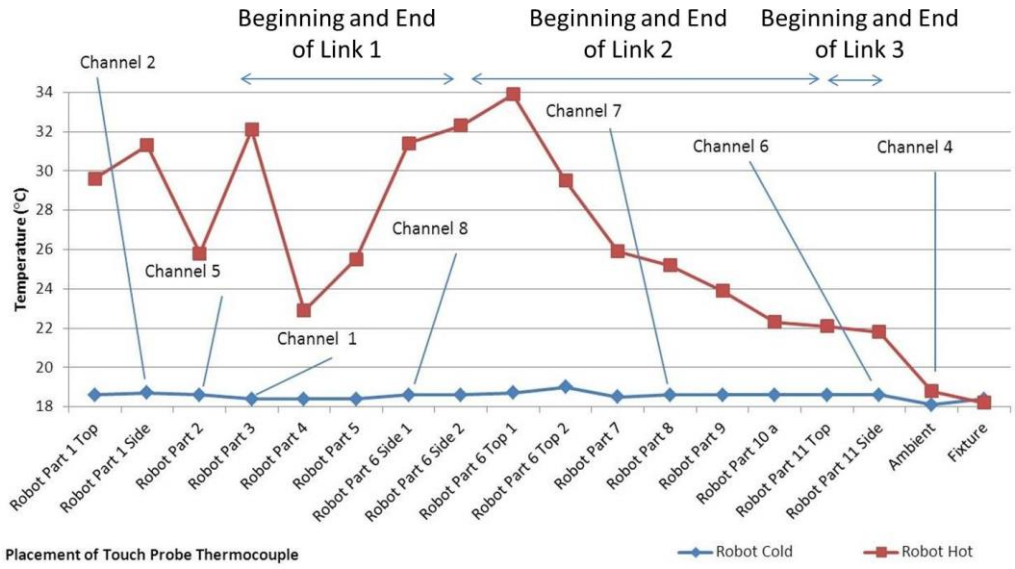


**Figure 111: Temperature profile (six hours 200mm/s circle motion)**

Robot accuracy for the linear positioning in the X Axis shown by Figure 112. In the 'cold' state the positioning accuracy is 500µm over the working stroke of 1.3m, with hysteresis of 110µm. Repeatability is 40µm (error bars). In this case the level of hysteresis would be the limiting factor for error path compensation. The magnitude of the thermal effect is 90µm.

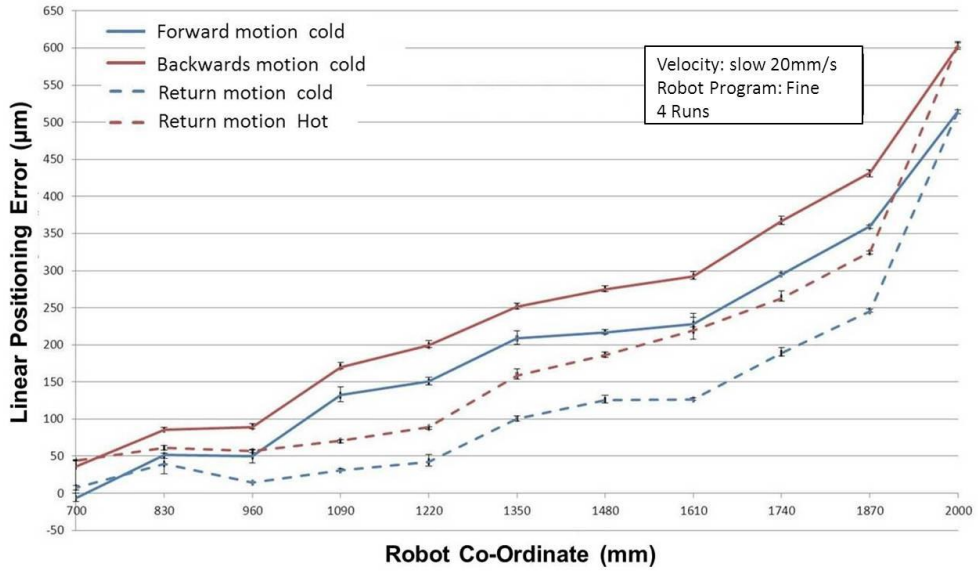


**Figure 112: Thermal effect X axis linear motion linear positioning**

For the X linear motion straightness (Z) measurements shown in Figure 113 is marginally affected by thermal effects. The cold state of the robot shows an

accuracy of 310µm. The accuracy is improved but the repeatability is low at 86µm (error bars) such that the variability in the measurements when hot and cold, overlap. At co-ordinate 1610mm to 2000mm this thermal effect is -15µm to -30µm.

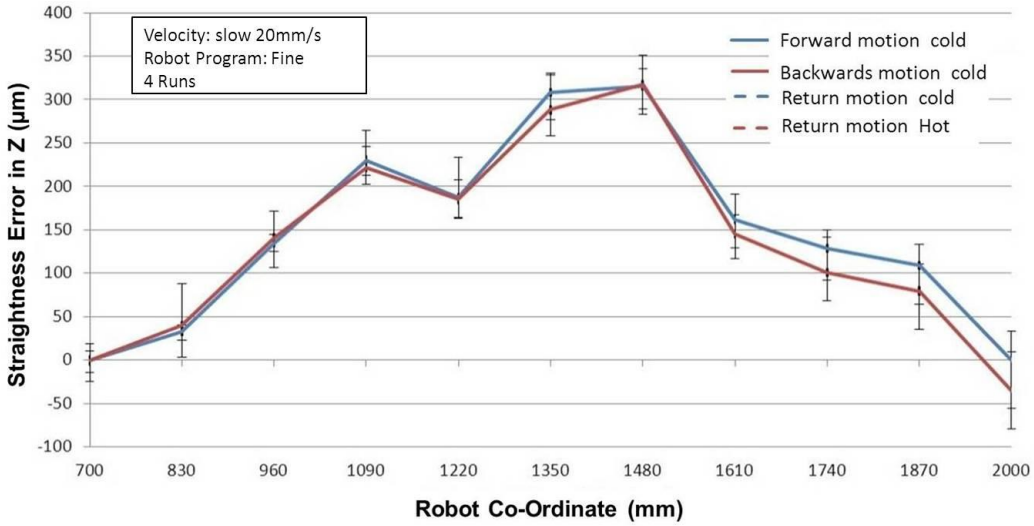


**Figure 113: Thermal effect X linear motion straightness (Z direction)**

For the X linear motion the straightness (Y) error is shown in Figure 114. This shows the largest range from the forward motion error being -100µm and a hysteresis of 300µm. Repeatability is at 30µm (error bars). The magnitude of thermal effects is 33µm.

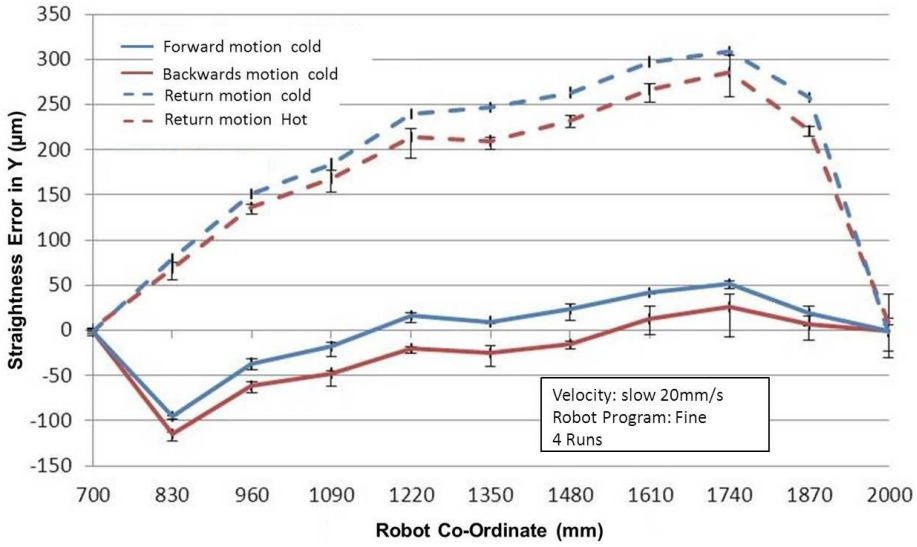


**Figure 114: Thermal effect X linear motion straightness (Y direction)**

For the Y linear motion positioning accuracy shown in Figure 115, the cold ‘state’ error is -746µm. Hysteresis shows -325µm error motion while the repeatability is 20µm (error bars). This level of hysteresis would limit the error path compensation. The thermal effect in the robot is at -90µm with a repeatability of 25µm.

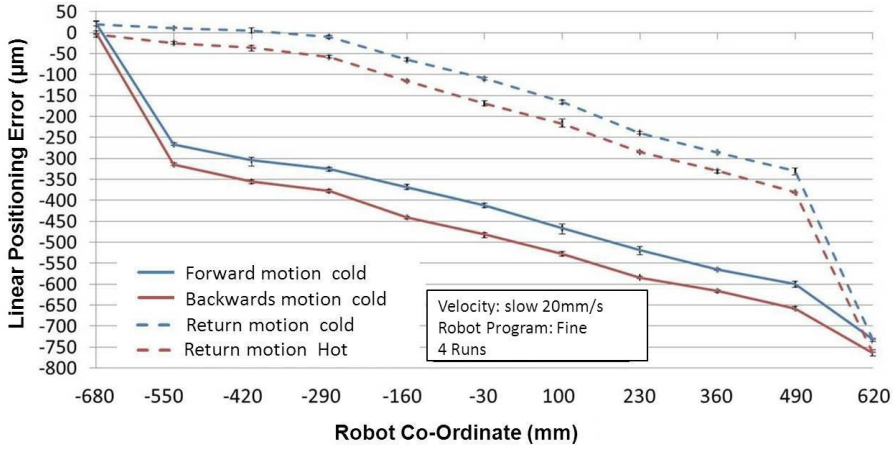


**Figure 115: Thermal effect Y linear motion linear positioning**

For the linear motion straightness (Z) in Figure 116, maximum error in the ‘cool’ state is at 341µm. Hysteresis shows error of 45µm. Repeatability is 17.4µm (error bars). Thermal effects have a 30µm improvement on the robot accuracy and a worse repeatability at 75µm.

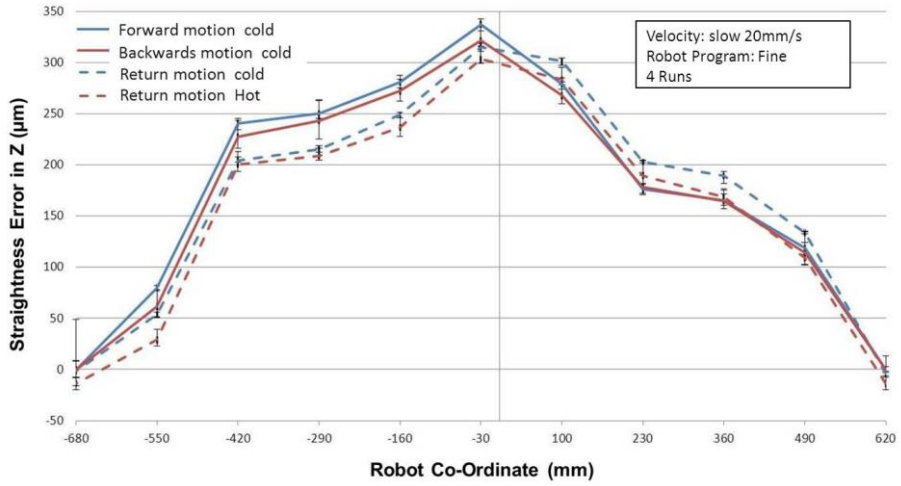


**Figure 116: Thermal effect Y linear motion straightness (Z direction)**

For the linear motion straightness (Y) in Figure 117, maximum error in the ‘cool’ state is at -150µm. Hysteresis shows error of 90µm. From co-ordinate 100mm to 620mm there is a cross over between forward motion and the hysteresis. Repeatability is 20µm (error bars). Thermal effects have a 20µm improvement on the robot accuracy and a worse repeatability approaching 90µm.

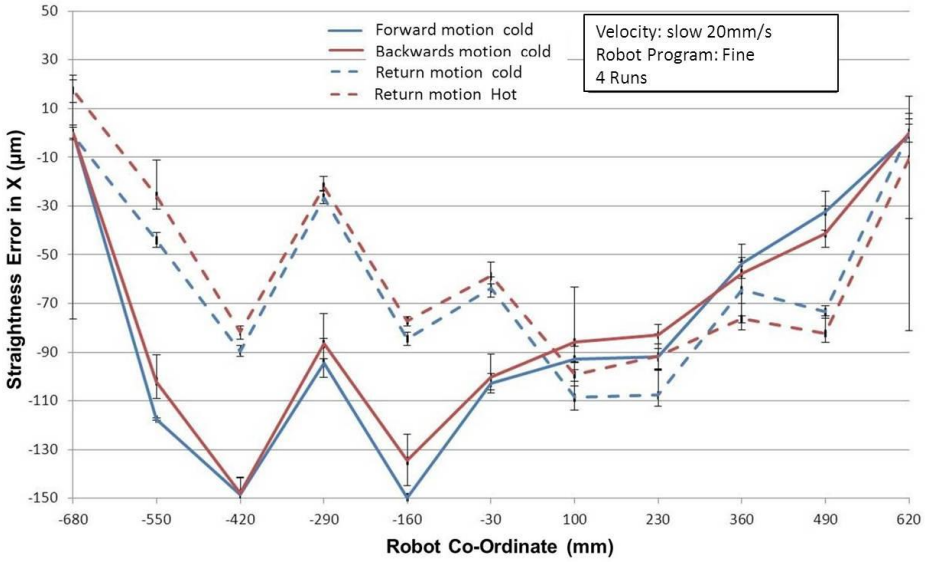


**Figure 117: Thermal effect Y linear motion straightness (X direction)**

The position measurements for the linear motion in the Z axis were done differently to the rest of the thermal performance geometric measurements in the X and Y axis. This is a set of mono-directional results and thermal effects after six hours of heating.

The results for the Z axes performance are now presented. A thermal profile (see Figure 118) of the robot during 94 minutes of slow linear motion positioning measurements at 20mm/s, for the Z axis is presented. This is related to the geometric accuracy performance see (Figure 78 to Figure 80 in sub-section 5.1.3) and in order to observe thermal effects, the repeatability of the robots geometric performance (see Figure 119 to Figure 121) is shown. The graphs show the by how much the reference co-ordinate is ahead or behind the subsequent one. So a positive value means the end effector has undershot the reference co-ordinate.

Figure 118 shows part six which contains four motors in the middle joint of the robot was mostly in operation during this motion; hence the heat produced in this part of the robot is the greatest. Part one is supporting the rest of the robot arm but moves a lot less by comparison to the joints lifting the spindle. Temperature rise of part six is 2.1°C above the ambient temperature. This implies that the robot has been doing less work than it did for the other axes. The spread in temperature across the robot for this slow speed of 20mm/s after 90 minutes is roughly the same as it was for the other axes at the beginning, and end temperatures approximately a degree Celsius or less.

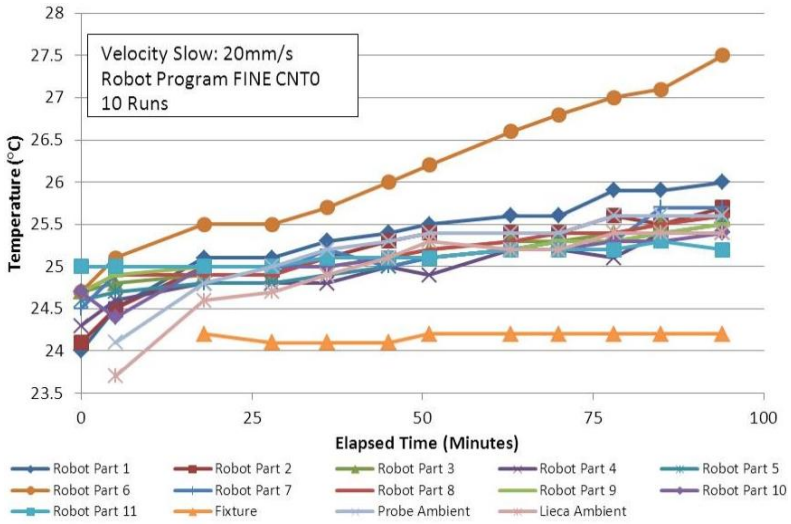


**Figure 118: Thermal variation of robot for linear motion in Z axis**

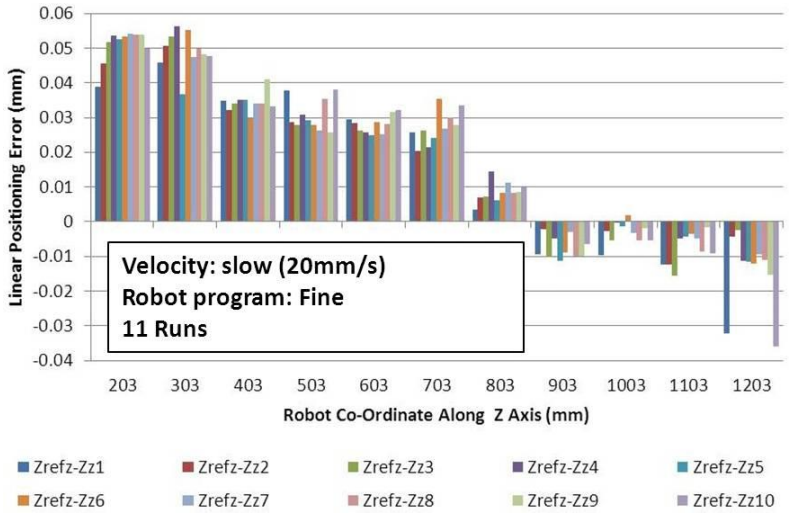


**Figure 119: Repeatability Z linear motion linear positioning (Z direction)**

The Z linear positioning ability of the robot in the Z axis is shown in Figure 120. It shows a repeatability of 56µm. A trend of -15µm is observed although this is below the repeatabilty of the measurement.

The straightness in X observed along the Z axis in Figure 120, shows 42µm repeatability. It is possible that there may be a -20µm drift.

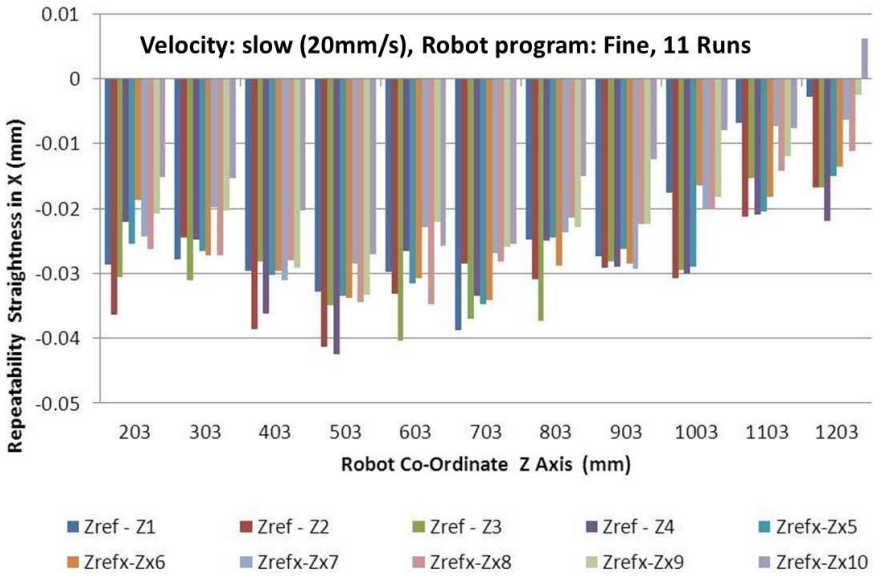


**Figure 120: Z Linear motion repeatability straightness (X direction)**

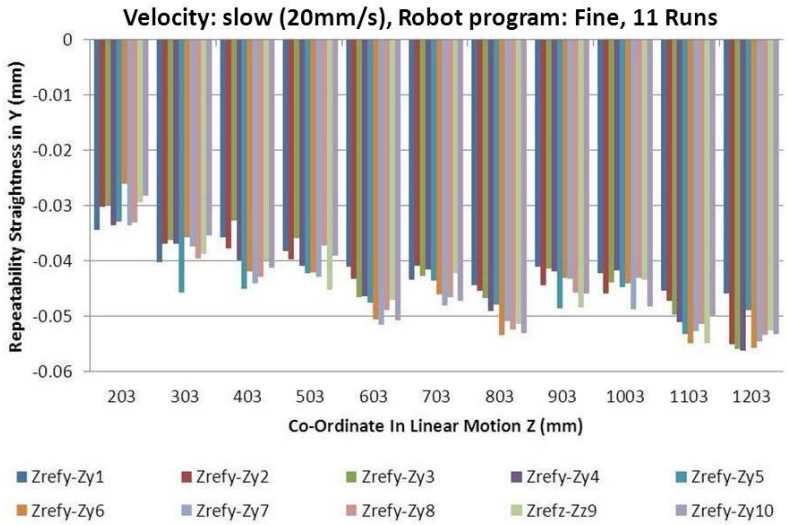


**Figure 121: Z Linear motion repeatability straightness (Y direction)**

The straightness in Y along the Z axis is shown in Figure 121. The robot is repeatable to 55µm. It may be that a trend of 10µm is present in this graph.

### 5.3.2 Thermal measurement

Thermal profiles were established for application within the thermal modelling. This was carried out for linear, circular and spiral motion. The thermal performance of the robot for linear slow positioning motion in the X and Y axis was assessed over a minimum of four runs.

Figure 122 shows a temperature plot of the robots response to ambient temperature using seven of the available eight channels for 39 hours and 50 minutes in the lab not doing any work. The ambient temperature varies at the most by 17.8°C to 18.3°C. The difference in the temperature along the robot is 18.7°C to 19.5°C. The coolest point is channel five which is the bottom of the centre of the base of the robot. The hottest part of the robot is channel two which corresponds to the top right corner of the base of the robot.

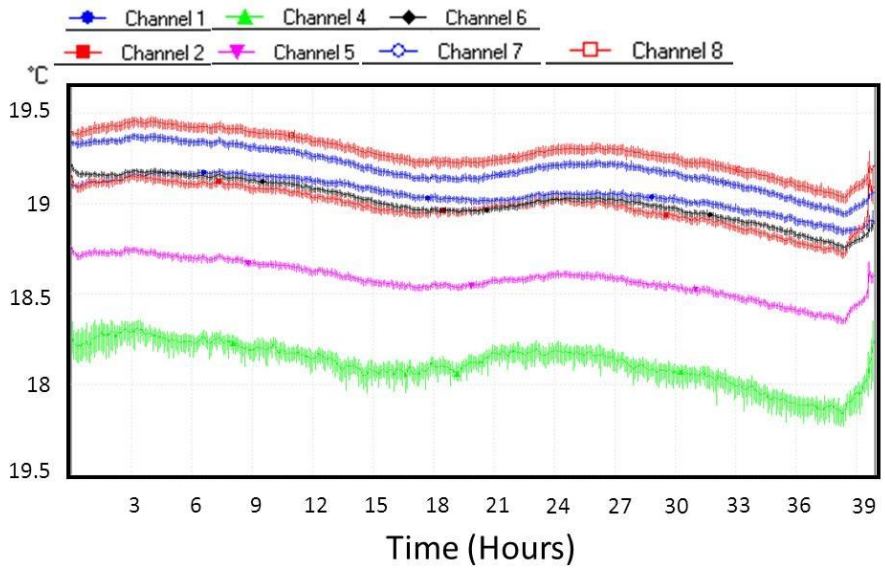


**Figure 122: Thermocouple response on different parts of the robot**

The small variation in ambient temperature is due to the thermally controlled laboratory, which is affected by the heat in the day time and outside sub-zero temperatures during the night. Measurements begin in the evening and temperature gradually decreases accordingly and as the morning approaches, the temperature rises. A variation of 0.5°C was observed throughout the 40 hour period. The response time of the robot to all the ambient temperature

variation does not change significantly and over 40 hours the lag time for the robot responding to the very small changes in temperature is minimal.

The result for the X linear motion is shown in Figure 123. The robot parts which showed a thermal response to the robot motion are one and six. Part one is within the error on the thermocouple of 1.5°C and part six is 2.2°C above the ambient temperature.

Part six is likely to be hottest because carries out the most work for the required motion. Part one will show heat because it has to do some work and has a larger motor that used to support the whole robot arm. It seems to be evident that the more the motor works the more it heats up and that induced heat is not directly related to the motor size. The spread in values from the beginning and end of motion remains within 0.5°C when excluding part one and six.

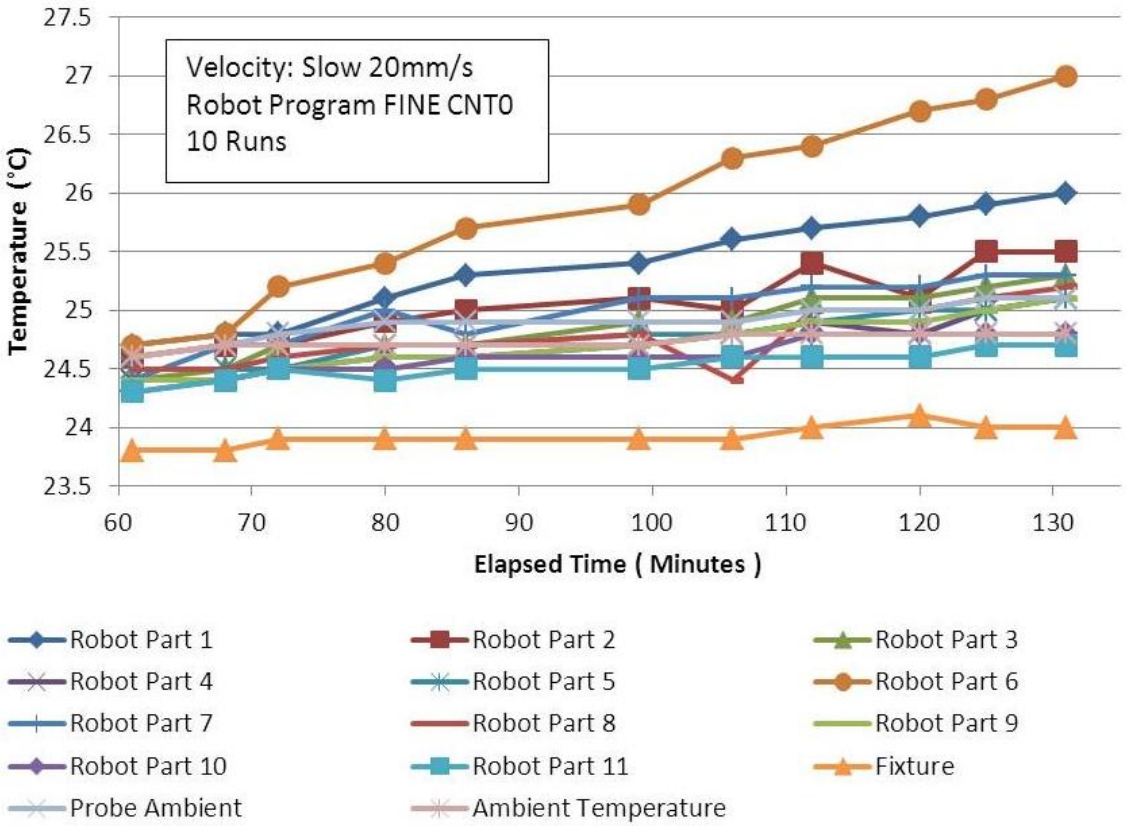


**Figure 123: Thermal variation of robot for linear motion X direction**

The data, Figure 124, shows that for the linear Y motion in part six heats up by 2.5°C. Also it can be seen that part one does not really increase significantly above ambient rising by 1.1°C, at best. This may be that it is following the ambient temperature.

Like the X axis, the Y axis has part six on the robot operating the most and a similar thermal profile is produced. Temperature rise of part six is 2.1°C above the ambient temperature. This implies that the robot has been doing less work than it did for the other axes. The spread in temperature on the robot of 1°C or less is the same as it was for the other axes at the beginning and end of the measurements.

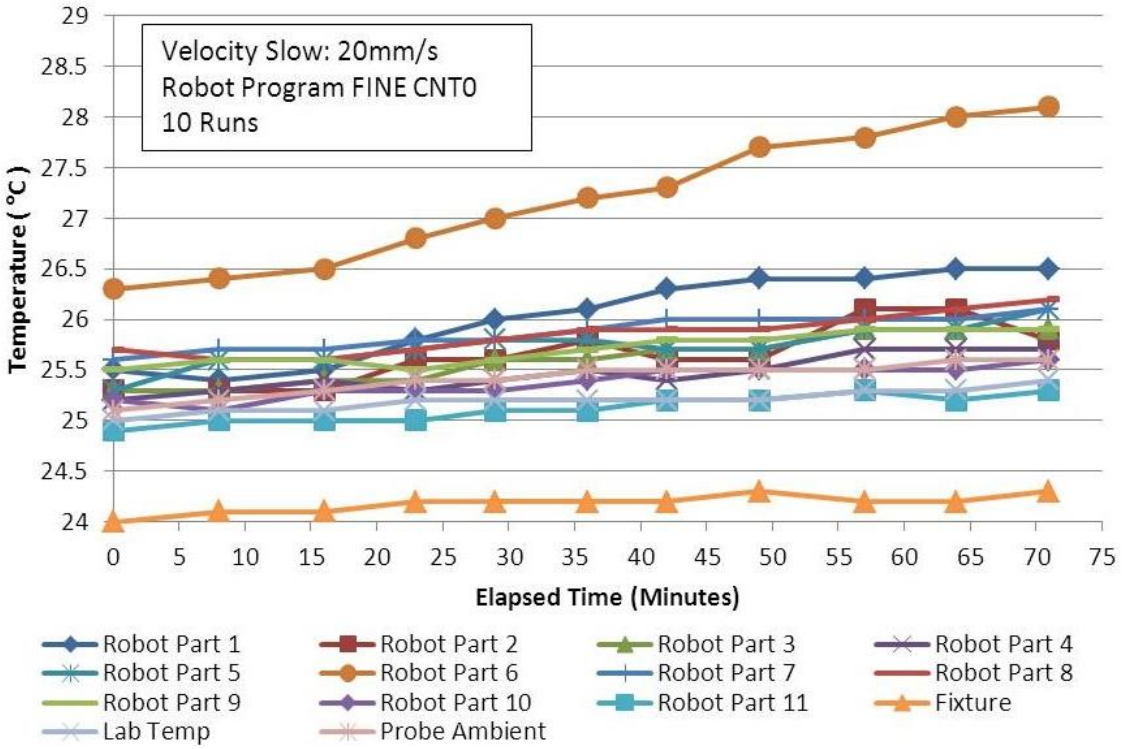


**Figure 124: Thermal variation of robot for linear motion in Y direction**

Combining Figure 123 and Figure 124 and removing offset parameters the temperature rise for slow linear positioning over two hours produces Figure 125. Robot parts three, four, six, and eleven are shown to have linear relationship with temperature. The values taken from this graph are contained in Table 3.

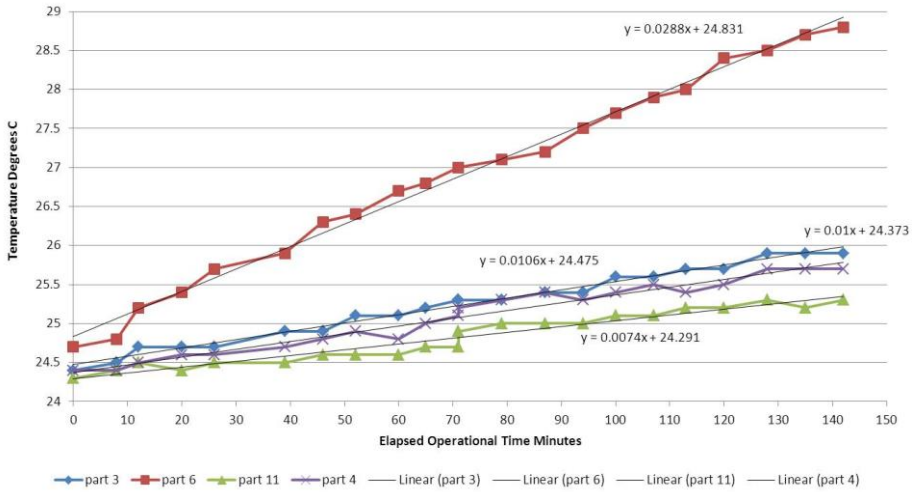


**Figure 125: Temperature rise of robot joints for XY linear motion**

**Table 3: Temperature increase for linear motion of robot part over time**

| Robot part | Temperature per unit time (°C/minute) |
|---|---|
| Three | 0.0106 |
| Four | 0.01 |
| Six | 0.0288 |
| Eleven | 0.0074 |

The temperature of the robot was then assessed after spiral motion at 100mm/s for 77 minutes. The data gathered from this can be seen in Figure 126. All the parts except 11 are above the ambient temperature by 0.5°C. Parts one, six and three are the hottest sections. As before, only the temperature for sections three, four, six and 11 were used for thermal modelling, see Figure 127 and Table 4.

**Table 4: Temperature increase for spiral motion of robot part over time**

| Robot part | Temperature per unit time (°C/minute) |
|---|---|
| Three | 0.214 |
| Four | 0.0085 |
| Six | 0.0423 |
| Eleven | 0.061 |

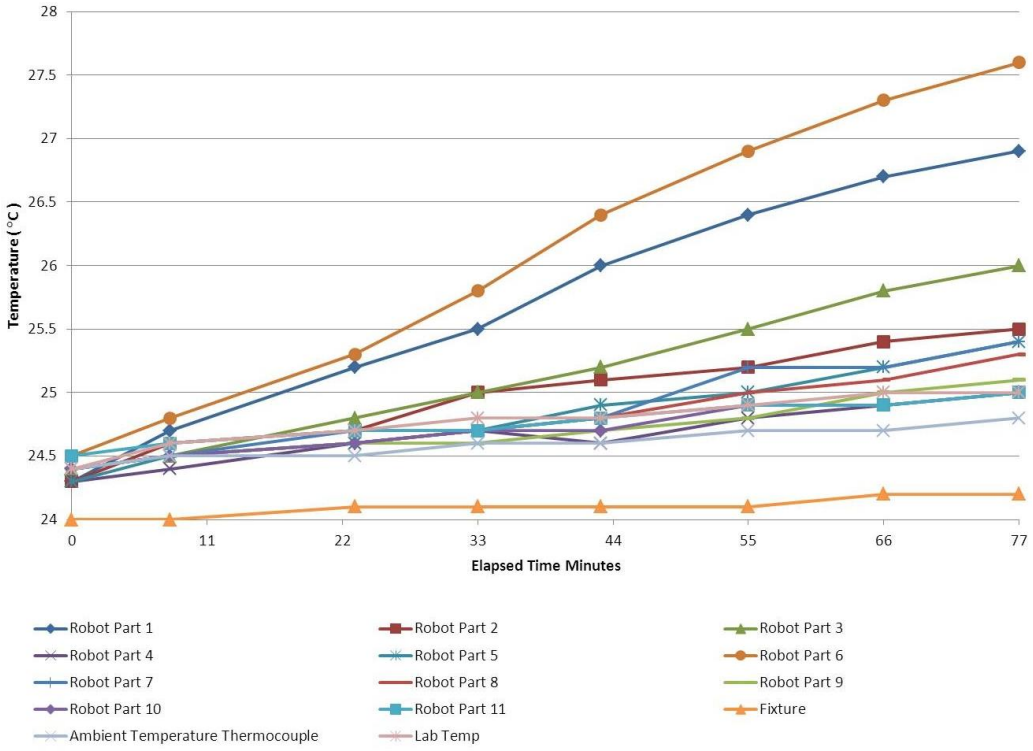


**Figure 126: Temperature rise of robot parts with 100mm/s spirals**

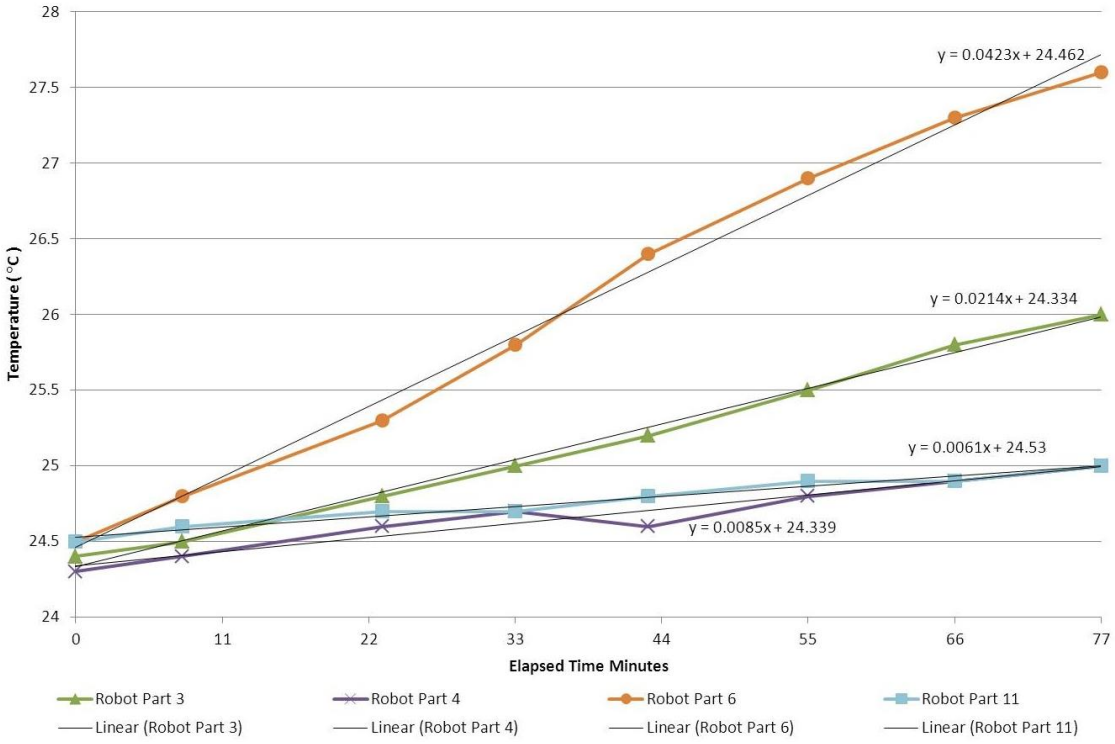


**Figure 127: Joint temperatures for 100mm/s spiral motion for model**

Motion of the end effector in a circular motion was carried out for approximately six hours, the thermal response is shown in Figure 128. In this case there is a clear difference in the response of part six of the robot. After approximately three hours, the linear temperature behaviour begins to fail in robot part six. Temperature rise in the same time period as the spiral for 77 minutes is about 0.5°C hotter. Every part of the robot in this test was hotter than ambient by almost 2°C. The rest of the robot parts can still be approximated to linear behaviour as before. Thermal modelling relationships are shown in Figure 129 and summarized in Table 5.

**Table 5: Temperature increase for circular motion of robot part over time**

| Robot part | Temperature per unit time (°C/minute) |
|---|---|
| Three | 0.214 |
| Four | 0.0101 |
| Six | Non-linear |
| Eleven | 0.008 |

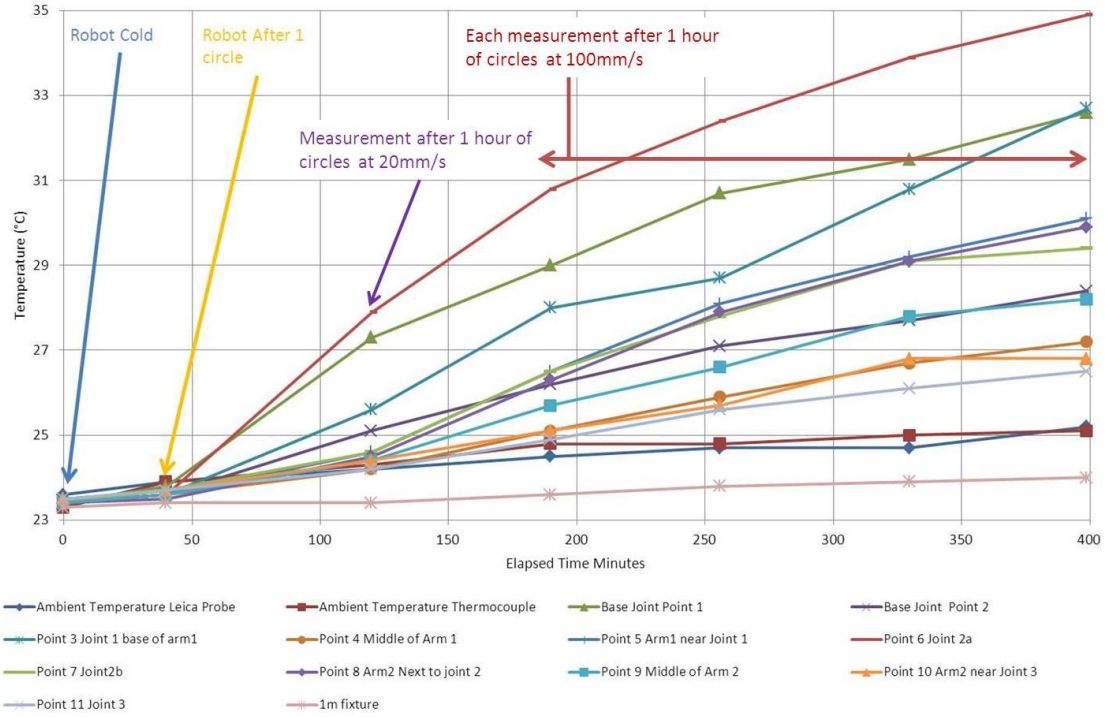


**Figure 128: Temperature rise for 100mm/s circular motion**

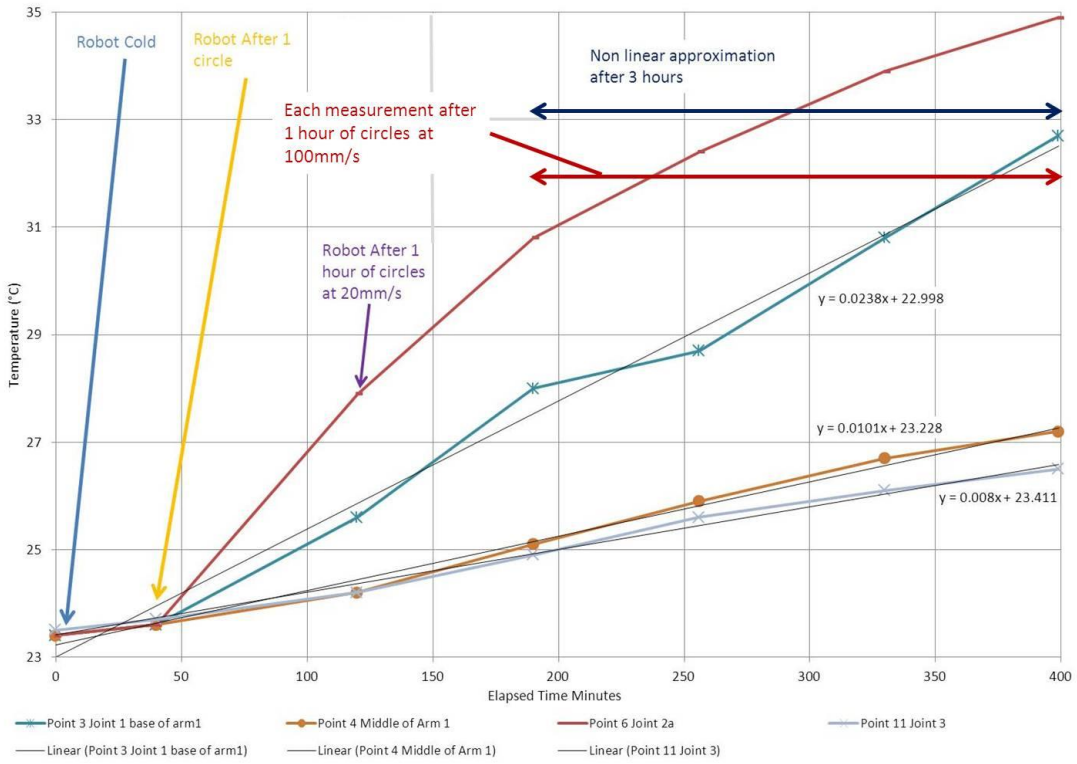


**Figure 129: Joint temperatures for 100mm/s circular motion for model**

# 6 Discussion

Here the results obtained from the geometric accuracy of the robotic arm, the thermal performance and the thermal effects will be discussed. The results are put into context with respect to recommendations for compensation for the smoothing process. Firstly, the thermal effects are presented and the impact they have on the smoothing process. Furthermore, how the thermal effects change the recommendation for compensation for the motions assessed on the robot is explored. Secondly, the thermal model is discussed as to its applicability for compensation in the smoothing plane. This is assessed by comparing it to the geometric and thermal effect results in the X and Y axis. Finally, the performance of the thermal measurement system is assessed, highlighting and reviewing different ways the robot heats up. The chapter concludes by discussing recommendations and future work.

## 6.1 Geometric, thermal effects, accuracy of model

The geometric performance of the robot has been assessed while it was in a cold state. This section will present and assess the accuracy and repeatability of the robot. This will focus on the linear positioning, the ISO standard paths and circular motion. The stated requirement in accuracy for the smoothing process is 100µm in the X and Y (Ahmed et al., 2010).

The robot's repeatability is quoted as 70µm by the manufacturer. The repeatability needs to be considered in conjunction with any accuracy data as the cumulative effect needs to be within the 100µm requirement. Thermal effects will in turn add to potential errors, the thermal input in most measurements was of the order of 12°C to 14°C.

The errors witnessed in the geometric measurements are of the same order of magnitude as that of (Young and Pickin, 2000). They concluded that inaccuracies arose due to the level of calibration of the robot encoders the carried out by the manufacturers.

### 6.1.1 X Axis

The errors in geometric linear positioning are shown in Figure 72, and the straightness in the perpendicular directions in Figure 73 and Figure 74. The discussion considers compensation of this axis. A comparison to the thermal model is also included.

In the forward linear X direction in Figure 72, geometric accuracy was 500µm. The repeatability in the measurements was 25µm (error bars) which was insignificant to the geometric error. Hysteresis was 110µm and implies that geometric compensation can achieve up to ±55µm accuracy. With approximately 13°C of thermal input, the magnitude of the thermal effects was up to 90µm (see Figure 112). Repeatability was 40µm with the robot in the 'worked' state and hysteresis was the same as it was when 'cool', hence compensation would be alike. The model predicted (see Figure 67) thermal effects to within 75%. At the beginning of the axis, the thermal effect was almost 71µm and at the end it reached about 122µm. The thermal effect increased further along the axis as it generally did in the linear positioning measurement.

The straightness in Y accuracy (see Figure 73) was accurate by 300µm to -100µm. Repeatability of the measurements was 75µm (error bars), this was under 22% of the magnitude at most. Hysteresis accounts for 250µm of error. Compensation for geometric errors therefore would give an optimal accuracy of ±125µm. Thermal effects are 33µm (see Figure 114) and were sometimes at the same order as the repeatability. Within the axis thermal effects were above the repeatability of some of the co-ordinates, as a result thermal compensation is suggested. The thermal model (see Figure 67) showed that the straightness in Y thermal effect agrees by 10% in the correct direction.

The straightness in Z accuracy shown by Figure 74 was accurate to 310µm. The worst repeatability measured was 89µm (error bars) at the furthest reach of the robot at 2000mm. Thermal effects (see Figure 113) were at most 40µm and the repeatability of a similar magnitude. Compensation would achieve accuracy to within ±89µm. In the model (see Figure 67), the magnitude of predicted

thermal effect was well below that shown in the experimental result. The error bars overlapped between hot and cold measurements, therefore the validity of the prediction between these points was reduced.

Reasoning for the thermal modelling for the straightness in X and Y being poor was due to the model only considering linear expansion and not containing bend and twist and other such thermal error effects.

The X axis requires geometric compensation while the robot is in a ‘cool state and has a potential accuracy of (±55µm, ±125µm, ±40µm) (X linear positioning, straightness in Y, straightness in Z). The potential accuracy is lower than the required 100µm as that stated by (Ahmed et al., 2010). Thermal effects that need to be compensated for when the robot is in a ‘worked’ state is recommended up to 89µm for the linear positioning motion, and up to 33µm, for the straightness in Y. The change in repeatability is marginally worse in two error motions in this axis (40µm, 86µm, 33µm) but because the values are lower, the potential accuracy is not likely to be affected. The other thermal error for straightness in Z is lower than the geometric accuracy and less than the worst repeatability value when the robot is not worked. Hence thermal compensation will not be deemed necessary.

### 6.1.2 Y Axis

The geometric linear positioning and straightness error in the perpendicular planes in the Y axis was also assessed in Figure 76, Figure 77, and Figure 78. The discussion highlights the recommendations compensating this motion path. Also how well these results match the thermal model is also discussed.

Y axis linear positioning accuracy (see Figure 75) was 725µm with a hysteresis of 325µm. The repeatability was at most 20µm and is insignificant to the error magnitude. Compensation as a result of the hysteresis will be at best ±162µm. The thermal effect (see Figure 115) in the motion of the robot was up to -85µm with a repeatability of at worst 15µm. Hence, thermal compensation is also recommended, the hysteresis when the robot was ‘worked’ was up to 350µm so

the compensation when hot will be at best ±175µm. The thermal model (see Figure 68) predicted the beginning and end of the axis of up to -40µm and 38µm respectively. The thermal model in Figure 68, predicted thermal effect magnitudes to at best 36% to 89% along most of the motion, except the centre. Modelling at -30mm predicted a -2µm error indicating most extensions cancelled. As the thermal error is not constantly -85µm, comparing different co-ordinates gives 32% to 64% accuracy at co-ordinates -550mm to -290mm.

The greatest straightness in X error (see Figure 76) is accurate to -150µm. The observed hysteresis is 90µm in the first half and in the second half of the axis the error motion crosses over such that it is greater than the forward motion. There was a repeatability of at worse 17.4µm (error bars). Thus geometric compensation will be at best ±45µm. Thermal effects shift the error motion 20µm (see Figure 117). Some of the thermal effects along this axis are outside of the repeatability and suggest possible compensation. Robot repeatability in most cases is made worse; 90µm at the robot co-ordinate 620mm. The thermal model (see Figure 68) suggests that the thermal error is positive by 78µm, which is the correct sign to the measured errors from co-ordinates -680mm to 230mm. After this the thermal error observed, is opposite to the prediction. The magnitude however is well above that, by almost 10 times. The thermal error prediction remains constant to within 1µm.

The whole motion for the straightness in Z error (see Figure 77) showed the accuracy to be 341µm. Repeatability was less than 18µm (error bars) and was insignificant to the error motion in either direction. Hysteresis was up to 45µm so overall compensation that can be achieved is of the same order of magnitude as the repeatability of around ±22.5µm. Thermal effects (see Figure 116) of 30µm were very close to the repeatability of the ‘cool’ robot and so will not be required. Hysteresis in the worked robot was almost the same as forward positioning in the second half of the robot motion and within the repeatability. The repeatability is worse by 75µm when the robot is ‘worked’ and will limit achievable accuracy to this value. The thermal model (see Figure 68) shows an abrupt change from point -680mm to -550mm of 79µm to -5µm respectively

which is not representative of the measurement. Thereafter the error is at most -6µm and the direction is correct from co-ordinate -550mm onwards. The overall accuracy for the thermal effects is 25% to 50% after position -680mm. In some cases this is within the repeatability of the robot as the measured forward thermal error from point 230mm to 620mm, is almost zero and has a repeatability outside the thermal error.

Thermal modelling considering the lack of twist and bend performs better than expected for the straightness in Z at 25% to 50% and most of the linear positioning in this axis performs adequately in terms of the magnitude of the error at 36% to 89% and at three co-ordinates is from 32% to 64%.

Geometric compensation could achieve an accuracy of (±45µm, ±162µm, ±22.5µm) (straightness in X, Y linear positioning, straightness in Z). This axis is below required accuracy of 100µm (Ahmed et al., 2010) and less accurate than the X axis. Repeatability was less than 20µm. Thermal effects will require compensation for the linear positioning in Y by up to 85µm and possibly in the straightness in X axis up to 20µm. Repeatability for these motions when the robot is worked is of the same order of magnitude as the thermal effects except in the case of the straightness in X measurements at 90µm.

### 6.1.3 Z axis

The Z axis was assessed in the forward direction for the errors in linear positioning and perpendicular straightness in X and Y. The information is useful if the robot is required to do other tasks. Only the positioning is critical for how the end effector moves to a required place for initial smoothing. Thermal effects for the whole linear positioning process were from a thermal input of approximately 2°C in the hottest part of the robot and 0.5°C in the next hottest section. This heat was generated in the motors while the measurement occurred during a period of approximately an hour and a half. Thermal modelling results do not represent the heat loads induced into the robot for this measurement, and so a comparison is not made.

The linear positioning inaccuracy in the Z axis (see Figure 119) was within ±100µm. The repeatability was at 56µm (error bars).This is half the geometric accuracy. The straightness in X geometric accuracy (see Figure 120) is -87µm. The repeatability is 52µm (error bars). The straightness in Y error (see Figure 121) shows that the robot is accurate by 50µm to -92µm. This motion is more accurate than the others along this axis. The repeatability in the measurements is worst at 43µm (error bars).

In the Z axis linear motions, general compensation may be needed up to 50µm at most to account for the inaccuracies and the repeatabilities would be within a sub 60µm tolerance. Thermal effects for the axis are not significant to the repeatability and accuracy.

This axis is the most accurate axis out of the X, Y and Z when undergoing motion when the robot is in a ‘cool’ state.

### 6.1.4 Discussion of circular motion repeatability

The motion of a circle by the robot was assessed to simulate the circular smoothing motion of a spiral at the diameter of 1.3m.

As the robot reaches the required velocity, the repeatability of the robot motion is reduced. In the X and Y axis, it is -900µm to 600µm with a magnitude of 1.5mm. The repeatability of the circular motion for the first repetition compared to the second is better in the first half of its motion by 100µm. From the half-way point, the repeatability was equal and then deteriorated at the end by 100µm. For smoothing, this repeatability is less than that quoted by the manufacturer. This is showing that between the circles two and three, they are repeatable to 100µm. From the initial circle they are vastly different. The Z motion repeatabilities had a magnitude of 350µm. The 1.3m diameter circle end effector motion is close to the maximum stroke of the robot and 1.5m diameter aspherical hexagonal segments to be processed. This would need to be taken into account when carrying out any smoothing procedure and would need to be considered for any compensation.

For the circular and spiral motion, the thermal effect has a trigonometric relationship. In the circle shown in Figure 70, the error motion in X behaves as a cosine function at 122µm to 45µm from the start of the circle to half way through while the error motion in Y has a sinusoidal behaviour starting at zero errors, peaking to 36µm and then to -39µm at the other end. The error motion in Z has neither behaviour; it changes minimally from just above zero at 5µm beginning to around -7µm at 130° of the circle to mid-point of 180° at -5.2µm. The error motion is reflected after this point due to the symmetrical nature of the robot positioning. The spiral motion produced a similar shape for error motion in X and error motion in Y, except the amplitude of the thermal errors was slowly increasing as the diameter of the spiral increased. The error motion in Z showed slight oscillation although again this was between -6µm and 5µm. Compared to the other errors this is minimal. At every positive maximum gradient of the thermal error in the Y motion, the error motion in Z is at a peak, a valley when it is at a negative maximum.

For the thermal errors predicted for the spiral and circular motion, 120µm to -50µm will be required for compensation depending on the error motion.

### 6.1.5 Discussion of ISO motion repeatability

The two repeatability tests were done using ISO standard paths:

1. Motion along a stated ISO path.
2. Linear continuous motion repeatability test in each of the axes for selected points along the perpendicular axes.

Over the majority of the motion of the cases of the along this ISO path, the repeatability of the robot was within the manufacturers specification of 70µm repeatability. The robot's corner motion repeatability was 70µm in the X, the robots small circle loop repeatability in Figure 85 was of the order 75µm. Some sections of this path showed worse repeatability, this was primarily due to limitation in synchronisation of the robot controller and measuring system.

Linear positioning overshoot tests showed that the robot performed to the level stated by the manufacturer. These tests were carried out at five times the speed

suggested for the smoothing operation. Hence repeatability may be better at the slower velocity.

## 6.2 Thermal performance

The thermal mapping provided information as to how to implement a thermal measurement system. The thermal performance of the robot was then assessed with a thermocouple based measurement system. The measurement system and thermal properties of the robot are discussed.

### 6.2.1 Thermal measurement system

Thermal mapping using the thermal imaging camera provided data as to where the greatest heat sources in the robots are. It also provided data for the thermal model in predicting the thermal profile along the robot arm. This was a quick way for establishing the thermal key points on the structure and temperature gradients along the links. Disadvantages are that thermal imaging cameras are costly to monitor multiple robot sections simultaneously and the images were not calibrated. Hence, producing active compensation from this method would not be efficient.

The thermal measurement system also gave information as to what temperatures the thermal model would need to be at specific points on the arm.

The thermocouples used had an accuracy of 1.5°C. Selection was based on an expected temperature rise of 20°C which assuming a thermal co-efficient of expansion of 11.25µm $m^{-1}$ $°C^{-1}$, extended robot reach of 2.05m, would result in a 338µm distortion. Temperatures measured were up to 13°C confirming the approach selected.

Thermocouples were placed in the hottest areas as well as along the first two links and in the last link. This gave information as to the temperatures along the links of the arm. Ambient temperature was also measured at the bottom of the moving base section of the robot. Offline measurements included more points

on the robot and helped to confirm online measurements and thermal modelling data.

The online measurement system was susceptible to noise but the measured temperature profiles on the robot showed repeatability for the measurements that were carried out in the linear positioning and fast circular motion. This would be adequate enough for developing offline compensation while online compensation would need further investigation to reduce noise levels.

### 6.2.2 Thermal output of robot

The robot motors all generated heat while the gear boxes located in each of the joints failed to show any significant thermal output. This explains the lack of any heat source in the second link from joint five and six. The two largest motors contained in the base section of the robot were both 4.3KW each. The rest of the motors 2.5KW, 1KW, 1KW and 750W were located in the middle joint (i.e. robot part six) which controlled the spherical wrist. The thermal map confirmed that part six of the robot heats up the most.

The thermal profile for the X, Y and Z show linear motion at (20mm/s) has a maximum of 3°C at the hottest (part six) and a 1.5°C rise at the next hottest part labelled as (part one). For spiral motion at 100mm/s the change above ambient 2.5°C over 77 minutes. The temperature for the 200mm/s circular motion over six hours was 12°C above ambient room temperature, in the hottest sections (Part three and six). The remaining structure, increased by at least 4°C above ambient

The most significant thermal errors from the ‘worked’ robot are in the smoothing plane, linear positioning motion. In the X and Y axis the thermal error is up to 90µm, and suggested for the straightness in Y error motion. The rest of the thermal effects for the other errors are the same level as the measured repeatability.

The room where the robot was situated was temperature controlled. The variation in the ambient temperature were measured at up to 1.5°C. This level

of variation was not great enough to influence the robots geometrical performance.

The time constant for the robot to cool down from hot was approximately 16 hours for the hottest sections. The base joint connected to the arm took the longest to reach the cool temperature. However the region in which most measurements were made, was around 12°C to 13°C above ambient and took approximately six hours to reach. Temperature variation for the hottest robot part after this time was not more than 3°C. These results were used for the thermal model.

## 6.3 Recommendation for further work

This initial research considered a limited set of motion paths for the assessment of the robot and the related thermal errors. This sub-section will lay out the additional work considered useful for assessing the geometric and thermal performance of the robot, for the purpose of smoothing an optic.

1. Use a higher accuracy volumetric measurement system to assess errors over the complete working volume. A suitable instrument would be an Etalon laser tracer.

2. Adapt thermal model to account for non-linear thermal effects and introduce non thermal errors discussed in the literature review to improve compensation.

3. Measure robot performance whilst working (smoothing optic) to ascertain whether loading affects performance.

# 7 Conclusions

The geometric accuracy for the end effector was assessed for the repeatability in a volumetric envelope with a laser tracker and interferometer. This showed that the robot linear motions exceeded the required accuracy for the smoothing process (Ahmed et al., 2010). The errors are repeatable such that compensation could be employed to achieve the requirements.

The repeatability of the Z axis is such that accuracy can be compensated to within ±50µm, the X axis to within (±55µm X error, ±125µm Y error, 40µm Z error) and (±45µm X error, ±162µm Y error, ±22.5µm Z error) in the Y axis. ISO standard stated paths and overshoot tests showed that the repeatability of the robot is adequate.

Thermal imaging was effective for developing the implemented temperature measurement system. The system used a combination of online and offline thermocouples measurements. Thermal output after six hours of work at 200mm/s (10 times that expected during the smoothing process) produced the greatest heat in the base joints and middle joint of the robot arm. The temperatures observed where up to 13°C above ambient.

The results show that thermal effects in the robot, was minimal at the slow velocity. At fast speeds the thermal effects can induce errors of up to 90µm. Results show at most a 50µm to 100µm change in accuracy, as a result of thermal effects in the X axis linear positioning.

Thermal modelling in sub-section 4.4.1 produced results that show thermal effects far exceed those found in the results. In such cases, only compensation for the measured thermal effect inaccuracies in the smoothing path is recommended. At best, the model forecasts linear positioning along the X axis measurement by at best 75%while initially it is greater by 50%. Three of the linear positioning thermal errors in the Y axis had 64% to 32% accuracy agreement at co-ordinates -550mm to -290mm and similar but opposite thermal error magnitudes are found from 230mm to 620mm. A more reliable correlation

was the linear positioning thermal modelling being 75% that of the thermal effect in the X axis.

Thermal effects in the smoothing plane were minimal. If any operation involved the central joint of the robot arm heating to that above 10°C, error compensation would be considered.

This thesis has investigated the geometric and thermal errors for a multi-axis smoothing facility within the Cranfield Precision Engineering Centre. Thermal assessment of the robot has provided information for modelling. The recommendations for compensation provided an initial step towards attaining the accuracies for this process. This work will serve as in part as a guide in the processing components on the smoothing cell.

# 8 References


Ahmed, A., Butterworth, I., Hunter, K., Dany, M. and Tadjerout, N. (2010), *Removal of the mid-spatial frequency abberations from large optics,* Group Project, MSc Precision Engineering, Cranfield University, Cranfield.

Alici, G. and Shirinzadeh, B. (2005), "A systematic technique to estimate positioning errors for robot accuracy improvement using laser interferometry based sensing", *Mechanism and Machine Theory,* vol. 40, no. 8, pp. 879-906.

Attia, M. H., Fraser, S. and Osman, M. O. M. (1999), "On-line estimation of time-variant thermal load applied to machine tool structures using a s-domain inverse solution", *International Journal of Machine Tools and Manufacture,* vol. 39, no. 6, pp. 985-1000.

Awang, M. S. and Abdullah, M. Z. (2010), "Robotic neurosurgery: a preliminary study using an active vision-guided robotic arm for bone drilling and endoscopic manovoeuvres", *Malaysian journal of medical science,* vol. 18, no. 2, pp. 53-57.

Briot, S. and Bonev, I. (2007), "Are parallel robots more accurate than serial robots?", *CSME Transactions,* vol. 31, no. 4, pp. 445-456.

Brogårdh, T. (2007), "Present and future robot control development—An industrial perspective", *Annual Reviews in Control,* vol. 31, no. 1, pp. 69-79.

Bryan, J. (1990), "International status of thermal error research (1990)", *CIRP Annals - Manufacturing Technology,* vol. 39, no. 2, pp. 645-656.

Camarillo, D. B., Krummel, T. M. and Salisbury, J. K. (2004), "Robotic technology in surgery: past, present, and future", *The American Journal of Surgery,* vol. 188, no. Supplement 1, pp. 2-15.

Cameron, S. (1999), *A comparison of methods for attaching thermocouples to printed circuit boards for thermal profiling,* presented at Nepcon West 1999, Session TS-19, Feb 23, available at: http://kicthermal.com/library/NW1999%20-%20A%20Comparison%20of%20Methods%20for%20Attaching%20TCs%20(Cam).pdf (accessed 28 April 2011).

Chen, B., Zhang, E., Yan, L., Li, C., Tang, W. and Feng, Q. (2009), "A laser interferometer for measuring straightness and its position based on heterodyne interferometry", *Review of Scientific Instruments,* vol. 80, no. 11, pp. 115113-1-115113-5.

Chritchlow, A. J. (1985), *Introduction to robotics,* Macmillan, New York.

Comley, P., Morantz, P., Shore, P. and Tonnellier, X. (2011), "Grinding metre scale mirror segments for the E-ELT ground based telescope", *CIRP Annals - Manufacturing Technology,* vol. 60, no. 1, pp. 379-382.

Corke, P. I. (1996), "A robotics toolbox for MATLAB", *IEEE Robotics and Automation Magazine,* vol. 3, no. 1, pp. 24-32.

Creighton, E., Honegger, A., Tulsian, A. and Mukhopadhyay, D. (2010), "Analysis of thermal errors in a high-speed micro-milling spindle", *International Journal of Machine Tools and Manufacture,* vol. 50, no. 4, pp. 386-393.

Davies, M. A., Cooke, A. L. and Larsen, E. R. (2005), "High bandwidth thermal microscopy of machining AISI 1045 steel", *CIRP Annals - Manufacturing Technology,* vol. 54, no. 1, pp. 63-66.

DeBra, D. B., Victor, R. A. and Bryan, J. B. (1986), "Shower and high pressure oil temperature control", *CIRP Annals - Manufacturing Technology,* vol. 35, no. 1, pp. 359-363.

Dukovski, V. (1990), "Robot accuracy and stiffness-an experimental study", *Robotics and Computer-Integrated Manufacturing,* vol. 7, no. 3/4, pp. 321-326.

Eastwood, S. and Webb, P. (2009), "Error significance analysis and compensation for HPKMs", *Industrial Robot: An International Journal,* vol. 36, no. 1, pp. 27-35.

Eastwood, S. J. and Webb, P. (2010), "A gravitational deflection compensation strategy for HPKMs", *Robotics and Computer-Integrated Manufacturing,* vol. 26, no. 6, pp. 694-702.

Ellery, A. D. (2000), "Inverse position kinematics solution", in Mason, J. B. P. (ed.) *An introduction to space robotics,* Praxis publishing limited, Bodmin, Cornwall, UK, pp. 159-164.

Gim, T. (1997), *Modelling and evaluation of time-varying thermal errors in machine tool elements* (PhD thesis), Cranfield University, Cranfield.

Gong, C., Yuan, J. and Ni, J. (2000), "Nongeometric error identification and compensation for robotic system by inverse calibration", *International Journal of Machine Tools and Manufacture,* vol. 40, no. 14, pp. 2119-2137.

Greenway, B. (2000), "Robot accuracy", *Industrial Robot,* vol. 27, no. 4, pp. 257-265.

Heisel, U., Richter, F. and Wurst, K. H. (1997), "Thermal behaviour of industrial robots and possibilities for error compensation", *CIRP Annals - Manufacturing Technology,* vol. 46, no. 1, pp. 283-286.

ISO 9283 (1998), "Manipulating industrial robots - performance criteria and related test methods (ISO 9283:1998)", *BSI,* vol. BS EN ISO 9283:1998, pp. i-ii-v, 1 - 62.

Jiang, B. C., Black, J. T. and Duraisamy, R. (1988), "A review of recent developments in robot metrology", *Journal of Manufacturing Systems,* vol. 7, no. 4, pp. 339-357.

Karan, B. and Vukobratovic, M. (1994), "Calibration and accuracy of manipultion robot models-an overview", *Mechanism and Machine Theory,* vol. 29, no. 3, pp. 479-500.

Kim, H. J., Kim, H. Y., Jeong, H. D., Lee, E. S. and Shin, Y. J. (2002), "Friction and thermal phenomena in chemical mechanical polishing", *Journal of Materials Processing Technology,* vol. 130-131, pp. 334-338.

Kim, K., Kim, M. and Chung, S. (2004), "Real-time compensatory control of thermal errors for high-speed machine tools", *Proceedings of the Institution of Mechanical Engineers, Part B: Journal of Engineering Manufacture,* vol. 218, no. 8, pp. 913-924.

Koivo, A. J. (1989), "Kinematics for manipulator joints, links and gripper", in *Fundamentals for control of robotic manipulators,* Whiley, Toronto Canada, pp. 35-69.

Koren, Y. (1985), "Chapter 4.6.1 Quaternion Defenition", in sun, B. and Fogarty, D. (eds.) *Robotics for engineers,* McGraw-Hill, US, pp. 118-122.

Kral, J. and Matthews, E. K. (1996), *Pyrolaser & pyrofiber infrared temperature measurement with automatic emissivity correction,* presented at Metal '96 International Fair of Metallurgy, Ostrava, Republic of Czechoslovakia, Pyrometer Instrument Company, Inc, available at: http://www.pyrometer.com/paper0596.htm (accessed 28 April 2011).

Lubrano, E. and Clavel, R. (2010), "Thermal calibration of a 3 DOF ultra high-precision robot operating in industrial environment", *Proceeding of the 2010 (IEEE) International Conference on Robotics and Automation,* Anchorage, Alaska, USA, IEEE, pp. 3692-3697.

Mackay, S. A. (1982), *Evaluation of robot performance testing* (MSc thesis), Cranfield University, Cranfield.

Mendes, N., Gustavo, H. C., X, d. A. O. and X, d. A. H. (2001), "Building thermal performance analysis by using MATLAB/SIMULINK", *Seventh International*

*IBPSA Conference,* 13-15 August 2001, Rio de Janeiro, Brazil, Building Simulation, Rio de Janeiro, Brazil, pp. 473-480.

Mian, N., Fletcher, S., Longstaff, A. P., Myers, A. and Pislaru, C. (2009), "Efficient offline thermal error modelling strategy for accurate thermal behaviour assessment of the machine tool.", in Gary, L. and Zhijie, X. (eds.) *Proceedings of Computing and Engineering Annual Researchers' Conference 2009: (CEARC09),* University of Huddersfield, Huddersfield, pp. 26-32.

Nawara, H. L. and Kowalski, M. (1987), "Analysis of the random component of multicoordinate measuring machines and metrological robots' position error", *CIRP Annals - Manufacturing Technology,* vol. 36, no. 1, pp. 373-376.

Nawrocki, W. (2005), *Measurement systems and sensors,* Artech House Publishers, Norwood, MA.

Nook, S. (1985), "Conference reports, 3rd international precision engineering seminar", *3rd International Precision Engineering Seminar,* Vol. 8, 13-16 May 1985, Interlaken, Switzerland, Precision Engineering, InterLaken: Precision Engineering, pp. 41-48.

Oitzman, M. and Campbell, J. (2000), "High accuracy positioning system implements robotic applications with guaranteed placement accuracy", *Industrial Robot: An International Journal,* vol. 27, no. 4, pp. 274-278.

Peters, J., Bryan, J. B., Estler, W. T., Evans, C., Kunzmann, H., Lucca, D. A., Sartori, S., Sato, H., Thwaite, E. G., Vanherck, P., Hocken, R. J., Peklenik, J., Pfeifer, T., Trumpold, H. and Vorburger, T. V. (2001), "Contribution of CIRP to the development of metrology and surface quality evaluation during the last fifty years", *CIRP Annals - Manufacturing Technology,* vol. 50, no. 2, pp. 471-488.

Poonyapak, P. and Hayes, M. J. D. (2006), "Towards a predictive model for temperature-induced deformation of an industrial robot", Schröcker, H. and Husty, M. (eds.), in: *Proceedings of EuCoMeS, the First European Conference on Mechanism Science,* February 21-26-2006, Obergurgl, Austria, pp. 1-12.

Reinhart, G., Gräser, R. and Klingel, R. (1998), "Qualification of standard industrial robots to cope with sophisticated assembly tasks", *CIRP Annals - Manufacturing Technology,* vol. 47, no. 1, pp. 1-4.

Ricciardi, G., Borsati, L. and Micheletti, G. F. (1985), "Theoretic and experimental methodologies for increasing Dynamic performances of general purpose robots and measuring machines", *CIRP Annals - Manufacturing Technology,* vol. 34, no. 1, pp. 375-379.

Sahul, S., Biswall, B. B. and Sabudhi, B. (2008), "A novel method for representing robot kinematics using quaternion theory", *IEEE sponsored conference on computational intelligence, control and computer vision in robotics & automation,* 10-11 March 2008, NIT Rourkela, NIT Rourkela, pp. 75-82.

Sartori, S. and Zhang, G. X. (1995), "Geometric error measurement and compensation of machines", *CIRP Annals - Manufacturing Technology,* vol. 44, no. 2, pp. 599-609.

Schellekens, P., Rosielle, N., Vermeulen, H., Vermeulen, M., Wetzels, S. and Pril, W. (1998), "Design for precision: current status and trends", *CIRP Annals - Manufacturing Technology,* vol. 47, no. 2, pp. 557-586.

Schneider, Carl-Thomas. AICON 3D Systems GmbH (2004), "Laser tracer - a new type of self tracking laser interferometer", *8th International Workshop on Accelerator Alignment (IWAA 2004), CERN,* 4-7 October, Geneva, pp. 1-6.

Schwenke, H., Knapp, W., Haitjema, H., Weckenmann, A., Schmitt, R. and Delbressine, F. (2008), "Geometric error measurement and compensation of machines—an update", *CIRP Annals - Manufacturing Technology,* vol. 57, no. 2, pp. 660-675.

Slocum, A. H. (1992), *Precision machine design,* Prentice-Hall, Englewood Cliffs, New Jersey.

Sulzer, J. and Kovač, I. (2010), "Enhancement of positioning accuracy of industrial robots with a reconfigurable fine-positioning module", *Precision Engineering,* vol. 34, no. 2, pp. 201-217.

Van Brussel, H. (1990), "Evaluation and testing of robots", *CIRP Annals - Manufacturing Technology,* vol. 39, no. 2, pp. 657-664.

Vira, V. and Estler, T. (1990), "Use of a contact-type measurement device to detect robots' hand positions", *ISA Transactions,* vol. 29, no. 4, pp. 21-35.

Weck, M., McKeown, P., Bonse, R. and Herbst, U. (1995), "Reduction and compensation of thermal errors in machine tools", *CIRP Annals - Manufacturing Technology,* vol. 44, no. 2, pp. 589-598.

Yang, S., Yuan, J. and Ni, J. (1996), "The improvement of thermal error modeling and compensation on machine tools by CMAC neural network", *International Journal of Machine Tools and Manufacture,* vol. 36, no. 4, pp. 527-537.

Yoshioka, H., Hashizume, H. and Shinn, H. (2004), "In-process microsensor for ultraprecision machining", *Science, Measurement and Technology, IEE Proceedings,* vol. 151, no. 2, pp. 121-125.

Young, K. and Pickin, C. G. (2000), "Accuracy assessment of the modern industrial robot", *Industrial Robot,* vol. 27, pp. 427-436.

Zverev, I., Eun, I., Chung, W. and Lee, C. (2003), "Thermal model of high-speed spindle units", *Journal of Mechanical Science and Technology,* vol. 17, no. 5, pp. 668-678.